Maximum Torque per Ampere and Maximum Torque per Voltage Operation of Brushless DC Motor Drive Systems with Extended Switching Schemes

by

Jinhe Zhou

B.Eng., The Hong Kong Polytechnic University, 2020

A THESIS SUBMITTED IN PARTIAL FULFILLMENT OF

THE REQUIREMENTS FOR THE DEGREE OF

MASTER OF APPLIED SCIENCE

in

THE FACULTY OF GRADUATE AND POSTDOCTORAL STUDIES

(Electrical and Computer Engineering)

THE UNIVERSITY OF BRITISH COLUMBIA

(Vancouver)

August 2022

The following individuals certify that they have read, and recommend to the Faculty of Graduate and Postdoctoral Studies for acceptance, the thesis entitled:

Maximum Torque per Ampere and Maximum Torque per Voltage Operation of Brushless DC Motor Drive Systems with Extended Switching Schemes

submitted by   Jinhe Zhou   in partial fulfilment of the requirements for

the degree of   Master of Applied Science

in   The Faculty of Graduate and Postdoctoral Studies

Examining Committee:

Dr. Juri Jatskevich, Professor, Electrical and Computer Engineering, UBC
Supervisor

Dr. Hermann Dommel, Professors Emeriti, Electrical and Computer Engineering, UBC
Supervisory Committee Member

Dr. Christine Chen, Associate Professor, Electrical and Computer Engineering, UBC
Supervisory Committee Member

Abstract

Hall-sensor-controlled brushless dc (BLDC) motors are widely used in many electromechanical applications due to their simplicity, low cost, and good torque-speed characteristics. The conventional commutation methods include the 120-degree and 180-degree switching logics. For these commutation methods, the maximum torque per Ampere (MTPA) and maximum torque per Voltage (MTPV) control schemes are often considered to achieve the optimal properties. Previously, many analytical and numerical implementations of MTPA and MTPV have been developed and widely applied. However, the common limitations such as deviation from the optimal operation due to machine parameters and high computational cost of controllers necessitate further research and improvements. In this thesis, three simple and novel control schemes have been proposed. Firstly, a hybrid MTPA/MTPV method is proposed based on the equations of 180-degree operation to combine the advantages of both methods. This hybrid method is shown to achieve high efficiency in steady state and fast response during electromechanical transients. Secondly, a numerical implementation of the MTPA and MTPV strategies has been developed for BLDC motors with 120-degree commutation to achieve better torque-speed characteristics compared with the conventional implementations. Thirdly, the switching logic has been extended to cover any conduction angle between 120 and 180 degrees while maintaining the MTPA optimal property. This proposed method is demonstrated to achieve up to 10% higher maximum achievable phase voltage than the conventional 120-degree operation from the same dc source voltage. Since the new methods are simple and computationally efficient, it is envisioned that they may be easily adopted in many applications utilizing Hall-sensor controlled BLDC motors where higher efficiency and faster transient response are desirable.

Lay Summary

Hall-sensor controlled brushless dc (BLDC) motor drives have been widely used in many electromechanical applications due to their simplicity, low cost, good torque performance, etc. For those motors, the control schemes often focus on developing the maximum torque for a given current or for a given available dc voltage. These control goals are referred to the maximum torque per Ampere (MTPA) and maximum torque per Voltage (MTPV), respectively. However, the conventional control methods often deviate from their ideal operation, resulting in lower efficiency and slower transient response. This thesis proposes several methods that improve the operation of BLDC motors in steady state and during electromechanical transients, as well as better utilization of the available dc source voltage. The proposed methods have been verified against the conventional methods and demonstrated to result in more efficient and faster performance. It is envisioned that the new methods will become adopted in many applications utilizing Hall-sensor controlled BLDC motors where higher efficiency and faster transient response are desirable.

Preface

Most of the research results presented in this thesis have been published in conference proceedings or submitted to scientific journal. In all of the papers, I was responsible for the majority of works including deriving the mathematical equations, implementing the control schemes, establishing the simulation models, programming the microcontroller, executing all simulations and hardware experiments, analyzing results, as well as initiating and editing the drafts. My supervisor, Dr. Juri Jatskevich has provided valuable guidance and constructive comments throughout the entire research process and paper editions. The coauthor, Dr. Seyyedmilad Ebrahimi also provided helpful instructions and feedbacks during the discussions and paper revisions. I also received some help from Mr. Jia Lu who has been a member of our research group, and helped me to debug the programs and carried out the hardware experiments. It should be stated that

Chapter 2 is based on the following conference paper that has been published:

J. Zhou, S. Ebrahimi, and J. Jatskevich, "Dynamic performance improvement of brushless dc motors using a hybrid MTPV/MTPA control," in *Proc. IEEE Int. Conf. Elect. Power Energy (EPEC)*, Toronto, Canada, 2021, pp. 469–474.

Chapter 3 is based on the following conference paper that has been published:

J. Zhou, J. Lu, S. Ebrahimi, and J. Jatskevich, "A compensation of commutation angle in Hall-sensor-controlled brushless dc motors for maximum torque per ampere operation", in *Proc. 21st Int. Symp. INFOTEH-JAHORINA (INFOTEH)*, East Sarajevo, Bosnia and Herzegovina, 2022, pp. 1–6.

Chapter 4 is based on the following journal paper that has been submitted:

J. Zhou, S. Ebrahimi, and J. Jatskevich, "Extended operation of brushless dc motors beyond 120° under maximum torque per Ampere control", (under review) submitted on Jun. 28, 2022.

Table of Contents

List of Tables

List of Figures

List of Symbols

In this thesis, scalars are written using italic fonts [e.g., i_{as}], and vectors are denoted by lowercase bold letters [e.g., $\mathbf{i}_{abcs}$], and matrices are denoted by uppercase bold letters [e.g., $\mathbf{L}_{abcs}$]. Furthermore, lowercase letters are used to denote instantaneous signals [e.g., i_{as}], and uppercase letters are to denote steady state values [e.g., I_{as}].

Only basic variables are aggregated in this section; all other variables are defined explicitly throughout the thesis.

α_d	Delay angle
D_{con}	Conduction angle
$\Delta\phi_v$	Firing angle compensation
$\Delta\bar{v}_{dc}$	DC voltage compensation
d_{pwm}	Duty cycle of pulse width modulation
d'_{pwm}, d'_{max}	Modified duty cycle of pulse width modulation and its maximum
e	Normalized speed difference
e_{as}, e_{bs}, e_{cs}	Back electromotive force
e_{qs}, e_{ds}	Back electromotive force in qd-rotor reference frame
H_1, H_2, H_3	Hall sensor
h_1, h_2, h_3	Hall sensor signal
h_s	Hall state integer

i_{as}, i_{bs}, i_{cs}	Stator phase current
i_{qs}, i_{ds}	Stator current in qd-rotor reference frame
I_{rms}, V_{rms}	Root-mean-square value of the steady-state stator current and voltage
J	Moment of inertia
K_{m1}, K_{m2}, K_{m3}, K_{m4}	Torque constant
K_p, K_i	Proportional-integral controller parameters
$\mathbf{K}_s^r$	Park's transformation matrix
λ_{as}, λ_{bs}, λ_{cs}	Stator flux linkage
λ_m'	Rotor permanent magnet flux linkage
L_{ls}	Stator leakage inductance
L_m	Stator magnetizing inductance
L_{ss}	Stator self-inductance
n	Machine speed
ω_r, $\hat{\omega}_r$, ω_r^*	Actual, estimated and desired rotor electrical speed
P	Number of poles
ϕ_{MTPA}, ϕ_{MTPV}	Firing angle corresponding to MTPA and MTPV operation
ϕ_v	Advance in firing angle
ϕ_v'	Compensated firing angle
r_s	Stator resistance
s	Laplace variable

ss	Switching state
$S_1, S_2, S_3, S_4, S_5, S_6$	Switching signal of the inverter transistor
t	Time
τ_L, τ_{L-1}, τ_{L-2}	Low-pass filter time constant
t_{com}, t_{cond}	Commutation and conduction interval duration
T_e, $T_{e-ripple}$	Electromagnetic torque and its ripple
θ	Angular position adding rotor angle with advanced firing angle
$\hat{\theta}$	Estimated angular position
θ_H	Hall-signal-quantized angular position
θ'	Compensated angular position
θ_r	Rotor electrical position
T_I	Hardware interruption interval
T_m	Mechanical load torque
T_{sw}	Switching interval
v_{as}, v_{bs}, v_{cs}	Stator phase voltage
v_{qs}, v_{ds}	Stator voltage in *qd*-rotor reference frame
V_{dc}	Fixed dc voltage
$\bar{v}_{dc}$	Effective average dc voltage
$\bar{v}'_{dc}$	Compensated dc voltage

List of Abbreviations

AC	Alternative Current
ADC	Analog-to-digital Converter
BLDC	Brushless Direct Current
COM	Common Operating Mode
d-axis	Direct Axis
DC	Direct Current
DSP	Digital Signal Processor
EMF	Electromotive Force
LPF	Low-pass Filter
LUT	Lookup Table
MTPA	Maximum Torque per Ampere
MTPV	Maximum Torque per Voltage
PI	Proportional-integral
PM	Permanent Magnet
PMSM	Permanent Magnet Synchronous Machine
PWM	Pulse-width Modulation
q-axis	Quadrature Axis
RMS	Root Mean Square
THD	Total Harmonic Distortion
VSI	Voltage Source Inverter

Acknowledgements

Firstly, I would like to express my deepest appreciation to my supervisor Dr. Juri Jatskevich, who has provided me with strong academic guidance, constructive and valuable comments, and detailed and clear instructions to carry me throughout the entire process of research and make this work and contributions possible. With his rich knowledge, great passion and personal charisma, I was led to a brand-new area and learned the effective ways of learning, researching, working, and living. I feel very lucky and grateful to be one of the students of this excellent, enthusiastic, and supportive supervisor.

I am also very thankful to my examining committee members Dr. Hermann Dommel and Dr. Christine Chen, for dedicating their valuable time and providing useful comments and feedback to improve my thesis. I also offer my gratitude to the faculty, staff and my fellow students at UBC, who have supported my study and helped my work in this field.

Specifically, my sincere thanks go to my friends and colleagues in Electric Power and Energy Systems research group at UBC. I am particularly grateful to Dr. Seyyedmilad Ebrahimi for his patient guidance and insightful comments in terms of researching, editing papers, as well as helping me to become a good Teaching Assistant. I would also like to thank Jia Lu, Erfan Mostajeran, Siqi Wu, Arash Safavizadeh, Levi Bieber, Gloria Wang, Parastoo Sadat Hosseinian, Sheraz Baig, Taleb Vahabzadeh, Zhenyao Sun, and many others, for the helpful discussions, inspiring working environment and the enjoyable time in our lab.

Last but not the least, the special gratitude is owned to my lovely parents Lijian Zhou and Yuguo Zhou for their solid supports during my master study, both morally and financially. I am also very thankful to all other family members who encouraged me and gave care to me during these years.

To my lovely Mom and Dad

Chapter 1: Introduction

1.1 Background

Due to the low-cost, high-power density, high efficiency, and good torque-speed characteristics, brushless dc (BLDC) motor drive systems are playing an important role in many electromechanical applications including electric vehicles, drones, automation robots, hoists, elevators, conveyor belts, computer disk drives, office printers, copy machines, washing machines, water pumping systems, fans, air conditioners, etc. [1]. Specifically, the Hall-sensor-controlled scheme is well-accepted in many low-cost applications such as underwater robotics [2] and small electric vehicles [3] due to its simplicity and reliable operation [4], where the sensorless control schemes may not be suitable or justified.

A typical BLDC motor drive consists of a permanent magnet synchronous machine (PMSM) driven by a voltage-source inverter (VSI). Two conventional control schemes of VSI, i.e., the 120-degree and 180-degree conduction switching schemes are commonly adopted. In the 180-degree commutation, each inverter switch (transistor) conducts 180 degrees in one electrical cycle, which results in continuous phase currents [5] and high-power delivery [6]. Particularly, this type of commutation logic has been utilized in applications such as electric bicycles [7] and turbochargers [8].

As for the 120-degree switching scheme, the conduction duration is reduced to 120 degrees for the inverter transistors and the phase current becomes zero twice (for 60 degrees each time) during one electrical cycle [9]–[10]. Despite the decreased voltage utilization and discontinuous current, the 120-degree commutation naturally achieves the approximation of the maximum torque per Ampere (MTPA) operation. This optimal and desirable property makes the 120-degree strategy

very common in a wide range of applications including water pumping systems [11], elevator systems [12], reciprocating compressors [13], flying drones [14], robotics [15], electric propulsion [16], etc.

In addition, to achieve different torque-speed characteristics for each of the above conduction logic, the relative position between the rotating magnetic field of the stator and the rotor field due to the permanent magnet is also controlled by the VSI [5]. For this purpose, the phase voltage is advanced relative to the rotor poles with a so-called advance in firing angle by simply shifting the conduction logics with respect to the rotor position. Three typical schemes of controlling the firing angle are considered in this thesis: common operating mode (COM); maximum torque per Ampere (MTPA) mode; and maximum torque per Voltage (MTPV) mode. The COM is the simplest control method with a fixed firing angle, which achieves the approximation of alignment between the phase voltages and the respective back electromotive forces (back EMFs). Specifically, the firing angle is fixed at zero in 180-degree operation [5], while it is fixed at 30 degrees with 120-degree conduction logic [9]–[11].

Unlike the simple COM without any optimal goals, the MTPA operation maximizes the ratio of the motor torque over the stator current amplitude. In other words, this control achieves the smallest stator current for a given torque, which in turn reduces the copper losses and increases the efficiency. Due to this optimal property, the MTPA is often used with BLDC motor drives in electrical vehicles [17]–[18], blender machines [19], pump applications [20], etc. that operate in steady state for a prolong period of time and energy savings are important.

The MTPV is another well-known control mode. The MTPV also aims at maximizing torque during the motor operation. However, it maximizes the torque for a given available dc source voltage. Instead of the current, the MTPV fully utilizes the voltage provided by the inverter [5],

[21]–[22], which results in operation over a wider speed range. Compared with the MTPA, the MTPV is more advantageous for high-speed applications [23]–[24]. Another advantage of the MTPV is the fast speed response due to the highest torque for a given dc voltage [25]. In contrast, the MTPA is known to be slower in response to the load changes [26]. Both MTPA and MTPV strategies are commonly incorporated with the pulse-width modulation (PWM) technique to effectively adjust the phase voltage of BLDC motors, when the input dc voltage of the VSI is constant [5].

1.2   Motivation

Considering the optimal properties, the MTPA and MTPV operations are to be properly incorporated with different conduction switching schemes. Previously, analytical and numerical methods have been developed for the 180-degree and 120-degree operations, respectively. However, several problems commonly exist in the most practical implementations of the MTPA and MTPV methods, which makes their operation not optimal. Some major challenges are identified and listed in this thesis.

Firstly, aiming at different optimization goals, the MTPA and MTPV achieves different machine performances. The MTPA is typically adopted because of its high efficiency, while it is not suitable for applications with high-speed operation or requirement of fast dynamic response due to its relatively low voltage utilization. Meanwhile, the MTPV operation has demonstrated advantages in terms of high-speed operation and fast speed response, but it has degraded the steady-state efficiency. To utilize the advantages of both methods and achieve a wide operating range of speed, the controllers have been developed to allow the MTPA operation in the low-speed range while switch to MTPV method at high speed [27]–[31]. This type of combined strategy has

become a typical method for applications with wide-speed ranges. However, there is seldom consideration for another type of combination which achieves the high efficiency as the MTPA and the fast dynamic response as the MTPV. With full utilization of these two properties, the machine performance is expected to be further improved.

Secondly, the 120-degree commutation applies non-complementary switching, which indicates that both transistors in the same phase leg are turned off twice for 60-degree intervals per revolution. Meanwhile, with the present of the stator inductance, the phase current cannot turn zero instantaneously. Instead, the phase current gradually goes to zero with a period referred to the commutation interval [9]–[10]. The length of commutation interval depends on machine parameters (i.e. time constant) and operating conditions [10], which varies the voltage waveforms and makes the derivation of the explicit analytical equations difficult (if not impossible). Meanwhile, the conventional control which achieves the approximation of the MTPA in COM can result in an operating point far away from the optimal due to the commutation process. To restore the MTPA optimal operation, some numerical methods have been developed. One of the most commonly adopted strategies is to control the stator currents based on the corresponding equations with respect to the desired torque [32]–[37]. Specifically, for Hall-sensor-controlled BLDC motors with round (non-salient) rotors, a proportional-integral (PI) controller is adopted in [37] to fix the current component along the *d*-axis of rotor reference frame at zero. However, the controller developed in [37] introduces high-order filter to reduce the current harmonics, which increases the complexity. Another type of MTPA methods is to directly eliminate the angle difference between the stator current and the back EMF by either measuring [38] or estimating this angle difference based on analytical equations [39]–[40]. Nevertheless, the existing implementations of the MTPA operation increases the complexity and the cost by including either long equations or additional

measurements. Therefore, a computationally-efficient, and simple and straightforward to implement method is very desirable.

As for the MTPV operation, this method is seldom applied for BLDC motors with 120-degree switching logic. Since for the 120-degree switching logic the commutation angle is operating-point-dependent and there is no explicit analytical expression for it, it becomes challenging to develop an analytical expression for the MTPV operation as well. In the literature, only a few numerical strategies have been developed for PMSMs. The strategies could be classified into the methods based on analytical approximations [27]–[31], [41]–[44] and the methods based on lookup tables (LUTs) [45]–[47]. The former ones derive the analytical current equations by applying voltage and current limits [41]–[42]. Subsequently, the current expressions could be utilized in current regulators [43]–[44] or vector current controllers (which are more common) [27]–[31]. As for the methods based on LUTs, the current values could be obtained from a table of pre-collected data (from detailed simulations or hardware experiments), which removes the calculation errors and reduces the computational burden for the microprocessor [45]. Considering the optimal properties, MTPV is highly desirable to be extended to the BLDC drives with 120-degree commutation to achieve the highest torque utilization, especially for high-speed operation.

Thirdly, a recent attention has been given to switching methods with the conduction angles other than conventional 120 and 180 degrees. For example, 150-, 160-, and 165-degree commutation schemes have been proposed and shown to reduce the torque ripple and current harmonics when compared with the 120-degree operation [48]–[51]. Studies have also been carried out in [52] to investigate the performance and voltage waveforms with conduction angles up to 168.75 degrees. These switching logics could be extended to achieve any conduction angles between 120 and 180 degrees. Specifically, with the increase of the conduction angle, the

increasing trend of ac phase voltage is observed in [51]. Therefore, operating with the extended conduction angle provides a feasible scheme for voltage adjustment on top of the conventional PWM. However, many of the previous studies have been carried out without the MTPA control, and the corresponding results may not be optimal ones. Instead, it is always very desirable to maintain the optimal operation during the voltage adjustment, and this point has not been addressed in the prior literature. Therefore, it is crucial to consider the MTPA method for the extended switching logics. Similar to the 120-degree operation, any extended switching logic will also apply non-complementary switching of transistors and be subjected to the operating-point-dependent commutation intervals.

1.3   Research Objectives

This thesis is focused on the challenges in achieving the MTPA and MTPV controls of BLDC motors with different conduction switching logics: (1) to achieve both advantages of high efficiency as the MTPA and fast dynamic response as the MTPV, a hybrid MTPA/MTPV control is to be proposed for the 180-degree operation; (2) to reduce the computational cost and remove additional measurements, simple and straightforward numerical implementations of the MTPA and the MTPV are proposed for the 120-degree operation; (3) the extended switching logic with conduction angles between 120 and 180 degrees is developed for voltage extension while ensuring the MTPA optimal property. The details of the objectives are summarized as below:

1.3.1 Objective I: A Hybrid MTPA/MTPV control of BLDCs operating with 180-degree switching logic

So far, simple and explicit equations for calculating the firing angles to achieve the MTPA and MTPV operating strategies have been well-known for BLDC motors operating using 180-degree switching logic [5]. Based on these equations, this thesis aims to develop a hybrid MTPA/MTPV control scheme to fully exploit the advantages of both MTPA and MTPV methods. The goal of this scheme is to smoothly switch between these two methods based on the operating conditions. Specifically, during steady-state operation, the MTPA should be adopted due to its high efficiency and reduced losses optimal property, which can save the energy in the long term. However, to fully exploit the torque capability and achieve faster dynamic response, the controller should convert to the MTPV operation in transients. This objective will achieve the energy savings in the long-term during steady state as well as achieve fast dynamic response due to higher available torque during transients.

1.3.2 Objective II: MTPA and MTPV control of BLDC motors with 120-degree switching logic

For BLDC motors operating with 120-degree switching logic, it is difficult to derive analytical equations for the firing angle corresponding to the MTPA and MTPV schemes due to the operating-point-dependent commutation interval [10]. This Objective aims to develop effective numerical approximations and implementations of the MTPA and MTPV schemes that improve upon the conventional control methods which neglect the commutation phenomena and impact of motor parameters.

Specifically, the MTPA strategies presented in the prior literature have increased the computational complexity of control algorithms by requiring solutions of large equations and/or increased the cost by requiring additional measurements. This research Objective aims to develop a simple and computationally efficient method to restore the MTPA operation with 120-degree switching logic. Additionally, to reduce the computational cost and simplify the controller, the methods based on lookup tables may be considered to fix the gap and develop an effective MTPV strategy for BLDC operating in 120-degree commutation.

1.3.3   Objective III: Generalizing the conduction switching scheme for extended voltage under the MTPA operation

In this Objective, an innovative extended conduction switching scheme with a conduction angle between 120 and 180 degrees is developed. By increasing the conduction interval beyond 120-degree, the motor phase voltage tends to increase [51]. Therefore, operating with an extended conduction angle provides a voltage extension above the conventional 120-degree operation with PWM. Operation in extended voltage range is expected to reduce the torque ripple, current ripple, and iron losses caused by the PWM [53]. Meanwhile, the MTPA implementation in Objective II should be extended to incorporate the generalized switching logic over the entire range of voltage. This control scheme should be discretized and implemented in a digital signal processor (DSP).

1.4   Platforms for Verification

For the purpose of conducting steady-state and transient studies to verify the proposed control schemes, simulations and hardware experiments are conducted as needed in each case. In this thesis, the simulations are built in MATLAB/Simulink [54]. Therein, the circuit toolbox SimScape Electrical [55] is used for implementing the detailed switching model of the VSI with parameters listed in Appendix 1.4. This toolbox is widely used by engineers and researchers in the industry and academia for accurate detailed simulations of power-electronic-based systems. Specifically, its VSI model could properly simulate the detailed operation of each transistor and automatically include the effect of conduction and commutation [56]. For the purpose of generality and flexibility of defining the parameters, the PMSM is modelled separately using conventional Simulink blocks. For many of the studies presented in this thesis, a typical industrial BLDC motor with parameters listed in Appendix A.1 has been considered. Other motors with diverse parameters have been considered as well to verify performance of the proposed control algorithms under various operating scenarios. Generally, the results of detailed simulations of BLDC motor-drive systems may be considered acceptable for verification of control schemes, since such models have relatively good accuracy and agreement with experimental prototypes as has been demonstrated in [10].
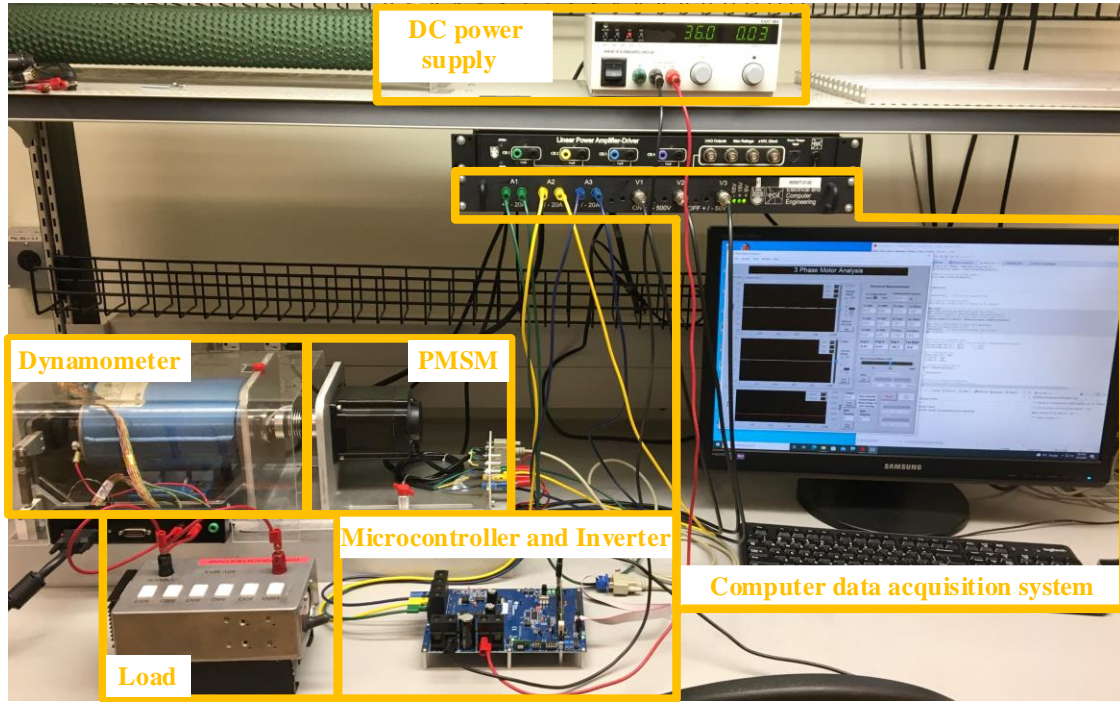
Figure 1.1 Experimental setup of the BLDC motor drive system in UBC lab Kaiser 3085-B.

For the hardware experiments, a setup shown in Figure 1.1 has been considered. The setup includes a voltage-source inverter board (DRV8301-HC-EVM) controlled by a microcontroller (TMS320F28035); a BLDC motor; a dc dynamometer which provides a mechanical load; a dc power supply; and a computer data acquisition system for recording measurements and subsequent analysis. The details including the layout, functional block diagram and schematic of the VSI boards are listed in Appendix D. Additionally, the BLDC motors model 86EMB3S98F, model EC 167131, and model JK80BLS02 are considered. The details are shown in Figures 1.2–1.4 and their parameters are listed in Appendix A.1–3, respectively. These three BLDC motors are typical industrial motors and have many applications such as water pumping systems [11], reciprocating compressors [13], industrial automation and robotic applications [57], etc.

Figure 1.2 Arrow precision brushless dc motor (Model 86EMB3S98F) considered in studies.

Figure 1.3 Maxon precision brushless dc motor (Model EC 167131) considered in studies.
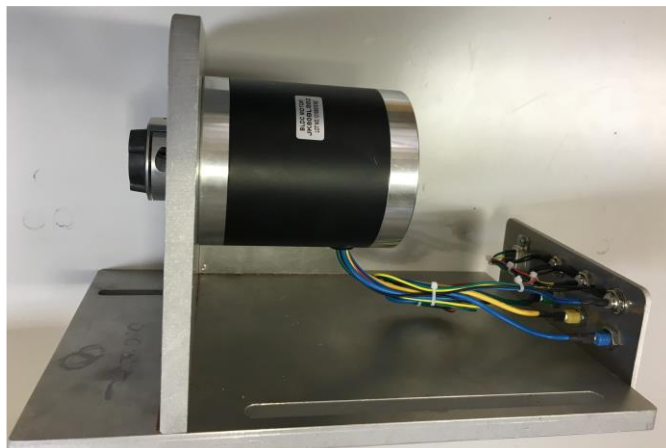
Figure 1.4 JKONG brushless dc motor (Model JK80BLS02) considered in studies.

Chapter 2: A Hybrid MTPA/MTPV Strategy for BLDC Motors with 180-Degree Operation

The BLDC motors with inverter operating under the 180-degree conduction mode apply complementary switching logic to the transistors in the same phase leg, which results in the typical six-step voltage waveforms and continuous currents [5]. Moreover, with the known pattern of phase voltages, simple and straightforward equations for the MTPA and the MTPV strategies have been investigated and developed in the literature [5]. Aiming at different optimization goals, the MTPA and MTPV strategies result in different torque-speed characteristics. The MTPA achieves high efficiency in steady state, but does not fully utilize the torque capability during transients. Meanwhile, the MTPV allows faster dynamic response, but degrades the efficiency in steady state conditions. To fully exploit the advantages of both methods, this chapter proposes a novel hybrid control scheme which utilizes the MTPA or the MTPV method based on the operating conditions. Specifically, during a steady-state operation, the MTPA is adopted due to its higher efficiency, while the controller converts to the MTPV during transients to fully exploit the torque capability and achieve faster dynamic response. The proposed hybrid control method is demonstrated through simulations and is verified to achieve high efficiency in steady state (similar to MTPA) and fast dynamic response (similar to MTPV).

2.1 Operation of BLDC Motors with 180-Degree Switching Logic

A typical Hall-sensor-controlled BLDC motor drive system considered in this thesis is depicted in Figure 2.1. Therein, a permanent magnet synchronous machine (PMSM) is driven by a voltage-source inverter (VSI) whose six switches (transistors S_1 through S_6) are commutated based on the rotor position θ_r. The rotor position angle is estimated using the three Hall-effect sensors depicted in Figure 2.1 as H_1, H_2 and H_3, respectively. The Hall sensors produce logical 0 or 1 depending on whether a sensor is under North or South rotor pole, respectively. The Hall sensor signals are denoted by variables h_1, h_2 and h_3, which are used to estimate the angular position $\hat{\theta}$. This position estimates the summation of the rotor angular position θ_r together with the physical shift of the Hall sensors ϕ_v which is also referred as the advance in firing angle. To further flexibly adjust the firing angle, a compensation of firing angle defined as $\Delta\phi_v$ is added with the estimated position $\hat{\theta}$. Then, the compensated angle θ' is used to determine the switching of the six switches based on the pre-defined commutation logic table. Specifically, different commutation logics could be developed by specifying the transistor conduction angle D_{con} (e.g., the conventional 180-degree operation is with $D_{con} = 180°$). It is also possible to control the effective dc voltage from a fixed dc voltage supply V_{dc} by incorporating the PWM in the commutation and adjust the corresponding duty cycle d_{pwm}. For the purpose of analysis and design of control schemes, a detailed model of the BLDC motor drive system [10] has been developed.
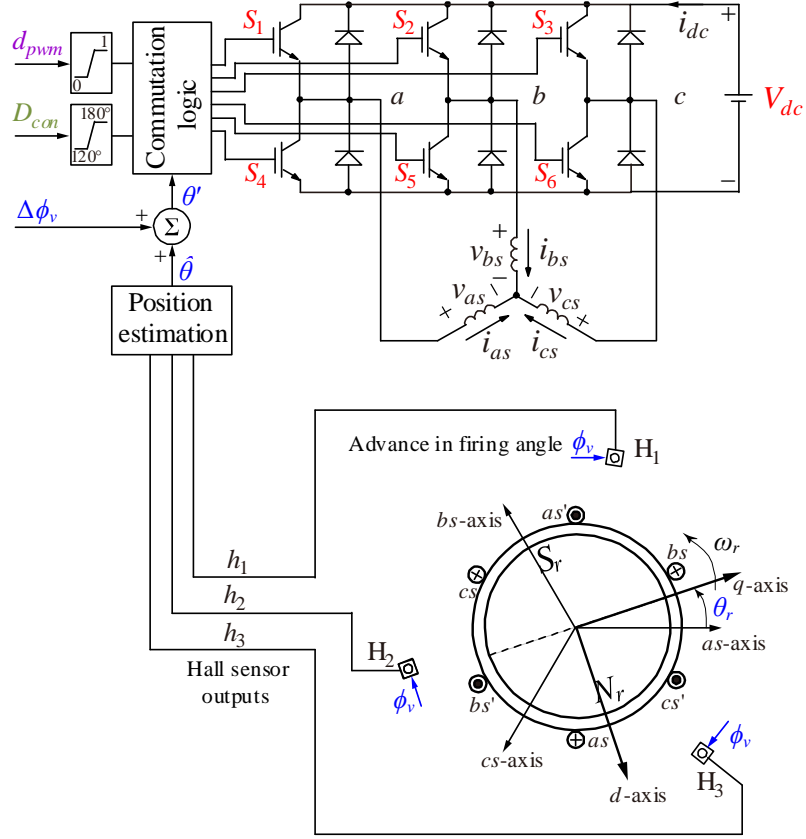
Figure 2.1 A voltage-source-inverter-driven BLDC motor controlled by Hall-effect sensors.

2.1.1 Modelling of the PMSM

For consistency with [10], the model of the PMSM is developed with the following assumptions: (a) the effect of saturation is negligible; (b) the eddy currents and hysteresis losses are negligible; (c) the rotor is round (non-salient); and (d) the back EMFs are sinusoidal. Hence, the stator voltage equation in phase coordinates can be expressed as

$$\mathbf{v}_{abcs} = \mathbf{r}_s \mathbf{i}_{abcs} + \frac{d\boldsymbol{\lambda}_{abcs}}{dt}, \qquad (2.1)$$

where $\mathbf{f}_{abcs} = [f_{as} \quad f_{bs} \quad f_{cs}]^T$ and f may represent voltage, current or flux linkage. The stator resistance matrix is

$$\mathbf{r}_s = diag[r_s \quad r_s \quad r_s]. \tag{2.2}$$

The flux linkage equation is

$$\boldsymbol{\lambda}_{abcs} = \mathbf{L}_s \mathbf{i}_{abcs} + \boldsymbol{\lambda}'_m. \tag{2.3}$$

where the inductance matrix and rotor flux are

$$\mathbf{L}_s = \begin{bmatrix} L_{ls} + L_m & -0.5L_m & -0.5L_m \\ -0.5L_m & L_{ls} + L_m & -0.5L_m \\ -0.5L_m & -0.5L_m & L_{ls} + L_m \end{bmatrix}, \tag{2.4}$$

$$\boldsymbol{\lambda}'_m = \lambda'_m \begin{bmatrix} \sin\theta_r \\ \sin(\theta_r - 2\pi/3) \\ \sin(\theta_r + 2\pi/3) \end{bmatrix}. \tag{2.5}$$

Here, L_{ls} and L_m are stator leakage and stator magnetizing inductance, respectively; λ'_m is the

rotor permanent magnet (PM) flux linkage; and θ_r is rotor (electrical) angle. Based on (2.1)–(2.5),

the phase back EMF voltages are expressed as

$$\mathbf{e}_{abcs} = \omega_r \lambda'_m \begin{bmatrix} \cos\theta_r \\ \cos(\theta_r - 2\pi/3) \\ \cos(\theta_r + 2\pi/3) \end{bmatrix}, \tag{2.6}$$

where ω_r is rotor (electrical) speed. Then, a model is established in the qd-rotor reference frame,

where Park's transformation [5]

$$\mathbf{K}_s^r = \begin{bmatrix} \cos\theta_r & \cos(\theta_r - 2\pi/3) & \cos(\theta_r + 2\pi/3) \\ \sin\theta_r & \sin(\theta_r - 2\pi/3) & \sin(\theta_r + 2\pi/3) \\ 1/2 & 1/2 & 1/2 \end{bmatrix}, \tag{2.7}$$

is used to transform the stator variables in phase coordinates $\mathbf{f}_{abcs}$ to qd-rotor reference frame $\mathbf{f}_{qds}$

as

$$\mathbf{f}_{qds} = \mathbf{K}_s^r(\theta_r)\mathbf{f}_{abcs}. \tag{2.8}$$

15

According to the selection of the rotor reference frame, the d-axis is aligned with the rotor North pole. Hence, the transformed back EMFs $\mathbf{e}_{qds}$ can be expressed as

$$e_{qs} = \omega_r \lambda'_m, \qquad e_{ds} = 0. \tag{2.9}$$

Subsequently, the stator voltage equations are written as [5]

$$v_{qs} = r_s i_{qs} + L_{ss}\frac{di_{qs}}{dt} + \omega_r L_{ss} i_{ds} + e_{qs}, \tag{2.10}$$

$$v_{ds} = r_s i_{ds} + L_{ss}\frac{di_{ds}}{dt} - \omega_r L_{ss} i_{qs}, \tag{2.11}$$

where $L_{ss} = L_{ls} + 1.5L_m$ is the stator self-inductance in qd-coordinates. For a round-rotor machine with P poles, the electromagnetic torque is calculated as

$$T_e = \frac{3P}{4}\lambda'_m i_{qs}. \tag{2.12}$$

In this thesis, it is also assumed that the mechanical subsystem is composed of a single rigid body with the moment of inertia J (combined rotor and load inertia). The dynamics of the mechanical subsystem can be expressed as

$$\frac{d\omega_r}{dt} = \frac{P}{2J}\left(T_e - T_m\right), \tag{2.13}$$

$$\frac{d\theta_r}{dt} = \omega_r, \tag{2.14}$$

where T_m is the load mechanical torque including friction.

2.1.2 Modelling of VSI with 180-Degree Conduction Logic

For BLDC motor drives, the switching of the six inverter transistors in Figure 2.1 could be determined based on the 180-degree conduction logic depicted in Figure 2.2. Here, the discrete switching logic of each transistor is determined according to the compensated angular position θ',

16

which is defined with the position estimated from the Hall signals $\hat{\theta}$ and the firing angle compensation $\Delta\phi_v$ as

$$\theta' = \hat{\theta} + \Delta\phi_v, \tag{2.15}$$

From Figure 2.2, each of the transistor is observed to conduct 180 degrees per electrical cycle, and thus, the conduction duration denoted by D_{con} equals to180 degrees. Since the VSI is supplied from a fixed dc source with voltage V_{dc}, the phase voltage is additionally modulated using PWM, as is also depicted in Figure 2.2. Changing the duty cycle of the PWM denoted by d_{pwm}, the root-mean-square (RMS) value of the phase voltages is also changed enabling effective voltage control of BLDC motors.
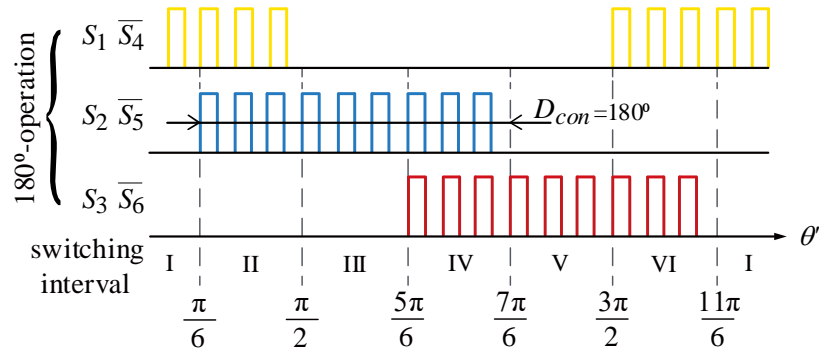
Figure 2.2 Typical commutation logic of the six-step 180-degree VSI operation with PWM.

2.1.2.1   Position Estimation

The estimated position $\hat{\theta}$ in (2.15) to construct the commutation logic is the estimation of the angular position denoted by

$$\theta = \theta_r + \phi_v, \tag{2.16}$$

17

It could be estimated based on the signals coming from the Hall-effect sensors, which output 1s and 0s based on the position of the rotor magnetic poles [5], as depicted by Figure 2.3(a).

To estimate the position efficiently, the Hall state integer variable h_s is defined by combining the Hall sensor outputs as [58]

$$h_s = 4h_1 + 2h_2 + h_3.$$ (2.17)
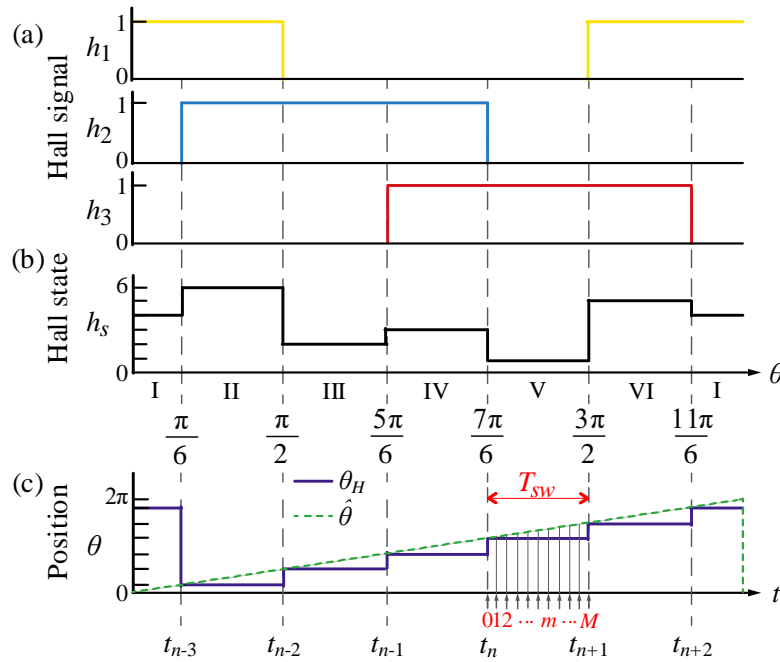
Figure 2.3 Signals assuming standard Hall sensors: (a) Hall-sensor outputs, (b) Hall state integer, and (c) quantized position and estimated position.

Assuming the standard Hall sensor outputs, this state integer changes with the switching interval I-II-III-IV-V-VI-I as the sequence 4-6-2-3-1-5-4 shown in Figure 2.3(b). At each step transition of the state integer h_s, the angular position could be updated. The obtained position is quantized as depicted in Figure 2.3(c). In practice, the values of the previous state and the current state are compared with the expected sequence to avoid any invalid updates caused by Hall signal errors.

18

Assuming that at the nth step transition of the Hall state, the time instance is t_n and the quantized

position is $\theta_H(t_n)$, the rotor speed can be estimated as

$$\hat{\omega}_r(t_n) = \frac{\theta_H(t_n) - \theta_H(t_{n-1})}{t_n - t_{n-1}}. \tag{2.18}$$

Then, the position angle θ between t_n and t_{n+1} [exemplified in switching interval V of Figure

2.3 (c)] at the point m can be approximately predicted based on the estimated speed as

$$\hat{\theta}(t_m) = \theta_H(t_n) + \int_{t_n}^{t_m} \hat{\omega}_r(t_n)dt, \qquad t_n \leq t_m \leq t_{n+1}. \tag{2.19}$$

where t_m is the time instant of point m. Practically, the estimated speed (2.18) and its integral

(2.19) are reset at every update of the quantized position (at every switching interval). The

estimated angular position $\hat{\theta}$ is depicted in Figure 2.3(c) (superimposed with the quantized

position). Therefore, the rotor angle may also be calculated from the estimated position with the

physically shifted angle of Hall sensors by

$$\theta_r(t_m) = \hat{\theta}(t_m) - \phi_v. \tag{2.20}$$

2.1.2.2   Average-Value Modelling of 180-Degree Conduction Logic

With the estimated position (2.19) and (2.20), the discrete operations of individual inverter

transistors in Figure 2.1 could be determined based on the logic depicted in Figure 2.2. For the

analysis of controller performance considered in this section, it is sufficient to focus on the slower

dynamics. In the so-called average-value models, the effect of fast switching is averaged-out

(neglected) using the fast averaging defined as

$$\bar{f}(t) = \frac{1}{T_{sw}} \int_{t-T_{sw}}^{t} f(\xi)d\xi, \qquad T_{sw} = \frac{\pi}{3\omega_r}, \tag{2.21}$$

where $\overline{f}$ represents the average value of the variable f, and T_{sw} is equal to one switching interval of the inverter (numbered as I–VI in Figure 2.3).

With the six-step 180-degree operation (shown in Figure 2.2), the average values of the stator qd voltages can be obtained as [10]

$$\overline{v}_{qs}^{r} = \frac{2}{\pi} d_{pwm} V_{dc} \cos \phi'_{v} = \frac{2}{\pi} \overline{v}_{dc} \cos \phi'_{v}, \tag{2.22}$$

$$\overline{v}_{ds}^{r} = -\frac{2}{\pi} d_{pwm} V_{dc} \sin \phi'_{v} = -\frac{2}{\pi} \overline{v}_{dc} \sin \phi'_{v}, \tag{2.23}$$

where V_{dc} is the fixed input dc voltage of the inverter, $\overline{v}_{dc}$ is the effective average value of the dc voltage, and ϕ'_{v} is the total firing angle (i.e. the compensated firing angle) defined as physical firing angle with its compensation as

$$\phi'_{v} = \phi_{v} + \Delta\phi_{v}. \tag{2.24}$$

The overall average-value model of the BLDC system can be obtained using (2.9)–(2.14) where the stator voltages v_{qs} and v_{ds} in (2.10)–(2.11) are replaced with their average values from (2.22)–(2.23).

For a typical BLDC with 180-degree operation in COM (i.e., the advanced firing angle is fixed at zero), the voltage and current waveforms obtained from the detailed model as well as the average-value model are shown in Figure 2.4. From the detailed model, the six-step voltage waveform and continuous current can be observed, which are consistent with the typical waveforms shown in the literature [10]. Meanwhile, the results from the average-value model are aligned with those obtained from the detailed model, while the fast-switching details are neglected. The average-value model predicts the performance of BLDC motor in this mode of operation very effectively and numerically efficiently.
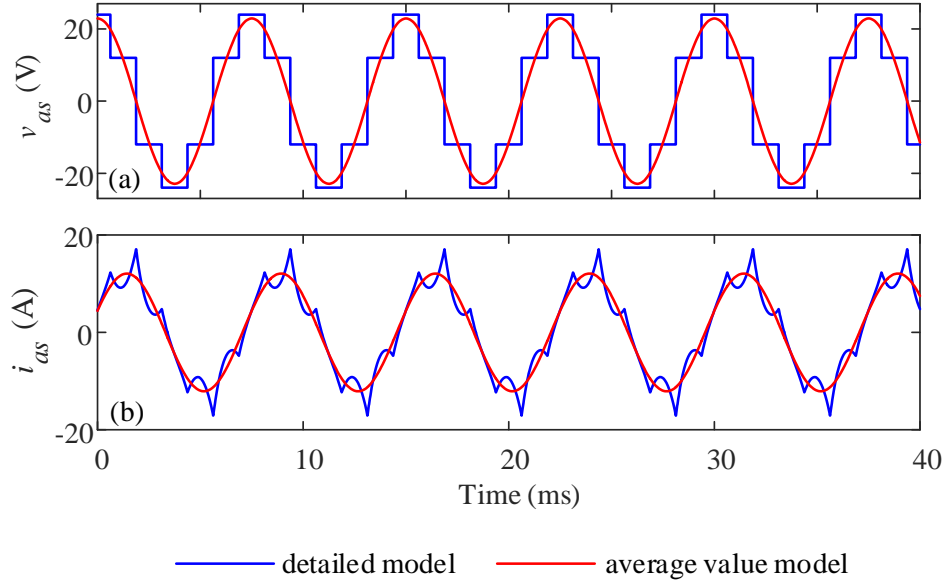
Figure 2.4 Typical waveforms of BLDC motors with 180-degree commutation in COM: (a) phase voltage, and (b) phase current.

2.2 Classical MTPA and MTPV Strategies

In COM, the advanced firing angle is fixed and could be properly incorporated into the switching logic by simply adjusting the physical position of the Hall sensors while fixing the firing angle compensation at zero. For 180-degree operation, this physical shift is generally fixed at 0 degree. However, for MTPA and MTPV operations which may be more desirable, the firing angle needs to be adjusted with respect to different operating strategies [5] and the compensation is no longer zero. To effectively incorporate the changing firing angle with the fixed shift of the Hall sensors, a non-zero compensation angle $\Delta\phi_v$ is added to the estimated angular position $\hat{\theta}$ (shown in Figure 2.1).

2.2.1　MTPV Operation

Maximum torque per voltage (MTPV) control aims at maximizing the electromagnetic torque for a given dc voltage. To obtain the firing angle that results in this maximization of torque, the partial derivative of torque with respect to ϕ'_v is first obtained and then set to zero. For the purpose of deriving the expression of torque with respect to the advanced firing angle, the steady state voltage equations are first obtained from (2.10) and (2.11) by setting the current derivatives to zero as

$$V_{qs} = r_s I_{qs} + \omega_r L_{ss} I_{ds} + E_{qs}, \tag{2.25}$$

$$V_{ds} = r_s I_{ds} - \omega_r L_{ss} I_{qs}. \tag{2.26}$$

From (2.9) and (2.25)–(2.26), the steady state q-axis current could be expressed as

$$I_{qs} = \frac{r_s V_{qs} - L_{ss} \omega_r V_{ds} - \omega_r r_s \lambda'_m}{r_s^2 + \omega_r^2 L_{ss}^2}. \tag{2.27}$$

According to (2.12), the steady state torque is proportional to the q-axis current as

$$T_e = \frac{3P}{4} \lambda'_m \frac{r_s V_{qs} - L_{ss} \omega_r V_{ds} - \omega_r r_s \lambda'_m}{r_s^2 + \omega_r^2 L_{ss}^2}. \tag{2.28}$$

Here, the voltages could be replaced with their average values in (2.22) and (2.23). Subsequently, the averaged steady state torque is as

$$\bar{T}_e = \frac{3P}{4} \lambda'_m \frac{r_s \dfrac{2}{\pi} \bar{v}_{dc} \cos \phi'_v + \omega_r L_{ss} \dfrac{2}{\pi} \bar{v}_{dc} \sin \phi'_v - r_s \omega_r \lambda'_m}{r_s^2 + \omega_r^2 L_{ss}^2}. \tag{2.29}$$

The partial derivative of (2.29) with respect to ϕ'_v is

$$\frac{\partial \bar{T}_e}{\partial \phi'_v} = \frac{3P}{4} \lambda'_m \frac{-r_s \dfrac{2}{\pi} \bar{v}_{dc} \sin \phi'_v + \omega_r L_{ss} \dfrac{2}{\pi} \bar{v}_{dc} \cos \phi'_v}{r_s^2 + \omega_r^2 L_{ss}^2}. \tag{2.30}$$

Setting (2.30) to zero, one can obtain the optimal angle $\phi'_v = \phi_{\text{MTPV}}$ as [5]

$$\phi'_v = \phi_{\text{MTPV}} = \tan^{-1}\left(\frac{\omega_r L_{ss}}{r_s}\right). \tag{2.31}$$

Additionally, to maintain the desired speed ω_r^*, the average dc voltage $\overline{v}_{dc}$ could be adjusted

by controlling the PWM duty cycle d_{pwm} (e.g., through a PI controller). The schematic diagram of

the MTPV control method is shown in Figure 2.5. Therein, the total firing angle for MTPV

$\phi'_v = \phi_{\text{MTPV}}$ is calculated using (2.31) based on the estimated speed from (2.18). Then the angle of

compensation $\Delta\phi_v$ could be obtained by deducting the shift of Hall sensors ϕ_v from the total firing

angle. Meanwhile, the estimated speed $\hat{\omega}_r$ is regulated to the speed setpoint ω_r^* by a PI controller

through adjusting the effective dc voltage, which is done by properly adjusting the duty cycle of

the PWM.
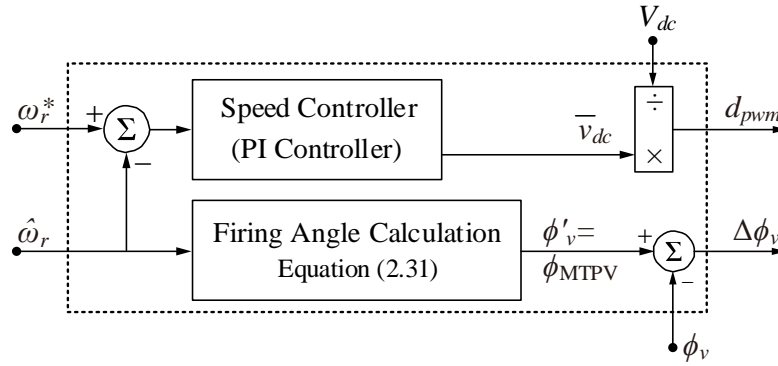
Figure 2.5 Diagram of the MTPV control method.

2.2.2   MTPA Operation

In the maximum torque per Ampere (MTPA) control, the ratio of the motor torque over the

stator current amplitude is maximized. Equivalently, the stator current is minimized for a given

torque, which reduces the copper losses and increases the efficiency. For the round machines, this is done by controlling the angle ϕ'_v such that the d-axis current of stator i_{ds} is maintained at zero, since i_{ds} does not contribute to the motor torque according to (2.12). For this goal, the steady state d-axis equation is derived from (2.9) and (2.25)–(2.26) as

$$I_{ds} = \frac{L_{ss}\omega_r V_{qs} + r_s V_{ds} - \omega_r^2 L_{ss}\lambda'_m}{r_s^2 + \omega_r^2 L_{ss}^2}. \tag{2.32}$$

Here, the voltages could be replaced with their average values in (2.22) and (2.23). Subsequently, the averaged d-axis current is as

$$\bar{I}_{ds} = \frac{L_{ss}\omega_r \frac{2}{\pi}\bar{v}_{dc}\cos\phi'_v - r_s \frac{2}{\pi}\bar{v}_{dc}\sin\phi'_v - \omega_r^2 L_{ss}\lambda'_m}{r_s^2 + \omega_r^2 L_{ss}^2}. \tag{2.33}$$

Setting (2.33) to zero, one can obtain

$$L_{ss}\omega_r \frac{2}{\pi}\bar{v}_{dc}\cos\phi'_v - r_s \frac{2}{\pi}\bar{v}_{dc}\sin\phi'_v - \omega_r^2 L_{ss}\lambda'_m = 0. \tag{2.34}$$

Replacing $\cos\phi'_v$ with $\sqrt{1-\sin^2\phi'_v}$ according to the Pythagorean identity and reordering the equation, a quadratic function with respect to $\sin\phi'_v$ is obtained as

$$\frac{r_s^2 + \omega_r^2 L_{ss}^2}{\omega_r^2 L_{ss}^2}\sin^2\phi'_v + \frac{\pi r_s \lambda'_m}{\bar{v}_{dc} L_{ss}}\sin\phi'_v + \frac{\pi^2 \omega_r^2 \lambda'^2_m}{4\bar{v}_{dc}^2} - 1 = 0. \tag{2.35}$$

The solution of (2.35) could be determined based on quadratic formula and the optimal angle $\phi'_v = \phi_{\mathrm{MTPA}}$ for the MTPA operation is obtained as

$$\phi_{\mathrm{MTPA}} = \sin^{-1}\left[\omega_r\tau_s\left(\frac{-\omega_r\tau_v + \sqrt{1 + \omega_r^2\tau_s^2\left(1 - \omega_s^2\tau_v^2\right)}}{1 + \omega_r^2\tau_s^2}\right)\right], \tag{2.36}$$

where, for simplicity, two intermediate variables have been introduced as

24

$$\tau_s = \frac{L_{ss}}{r_s} \,, \tag{2.37}$$

$$\tau_v = \frac{\pi \lambda'_m}{2\overline{v}_{dc}} \,. \tag{2.38}$$

The schematic diagram of the MTPA control method is shown in Figure 2.6, where a PI controller is used to regulate the estimated speed from (2.18) to the desired speed ω_r^* by adjusting the effective average dc voltage $\overline{v}_{dc}$. For the purpose of adjusting $\overline{v}_{dc}$, the PWM technique is used and the duty cycle of PWM is calculated by dividing the effective dc voltage by the fixed dc supply V_{dc}. Meanwhile, the total firing angle for MTPA $\phi'_v = \phi_{\mathrm{MTPA}}$ is calculated based on (2.36)–(2.38) with the estimated speed from (2.18) and the effective dc voltage from the output of the PI controller. Then, the angle of compensation $\Delta\phi_v$ is obtained by deducting the shift of Hall sensors ϕ_v from the total firing angle.
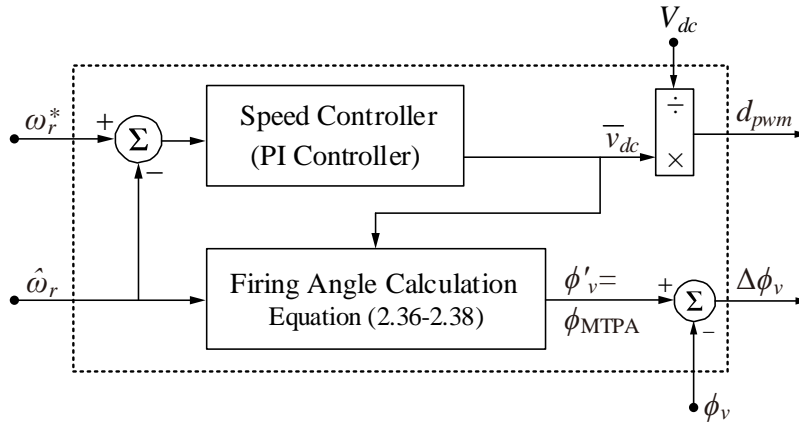
Figure 2.6 Diagram of the MTPA control method.

25

2.3 A Hybrid MTPV-MTPA Strategy

In the proposed hybrid method, the control dynamically adopts either the MTPV or the MTPA depending on the operating condition. In a steady state, the BLDC is operated with the MTPA using ϕ_{MTPA} defined in (2.36)–(2.38) to increase the efficiency. However, during transients, the BLDC is operated with MTPV using the firing angle ϕ_{MTPV} defined in (2.31) to fully exploit the torque capability of the machine for faster transients. The schematic diagram of the proposed combined MTPV/MTPA control method is shown in Figure 2.7.

As shown in Figure 2.7, in order to determine whether the system is in steady state or transient, a speed error index is defined as

$$e = \frac{\omega_r^* - \hat{\omega}_r}{\omega_r^*}, \tag{2.39}$$

which is the normalized difference between the actual speed $\hat{\omega}_r$ and the speed reference command ω_r^*.
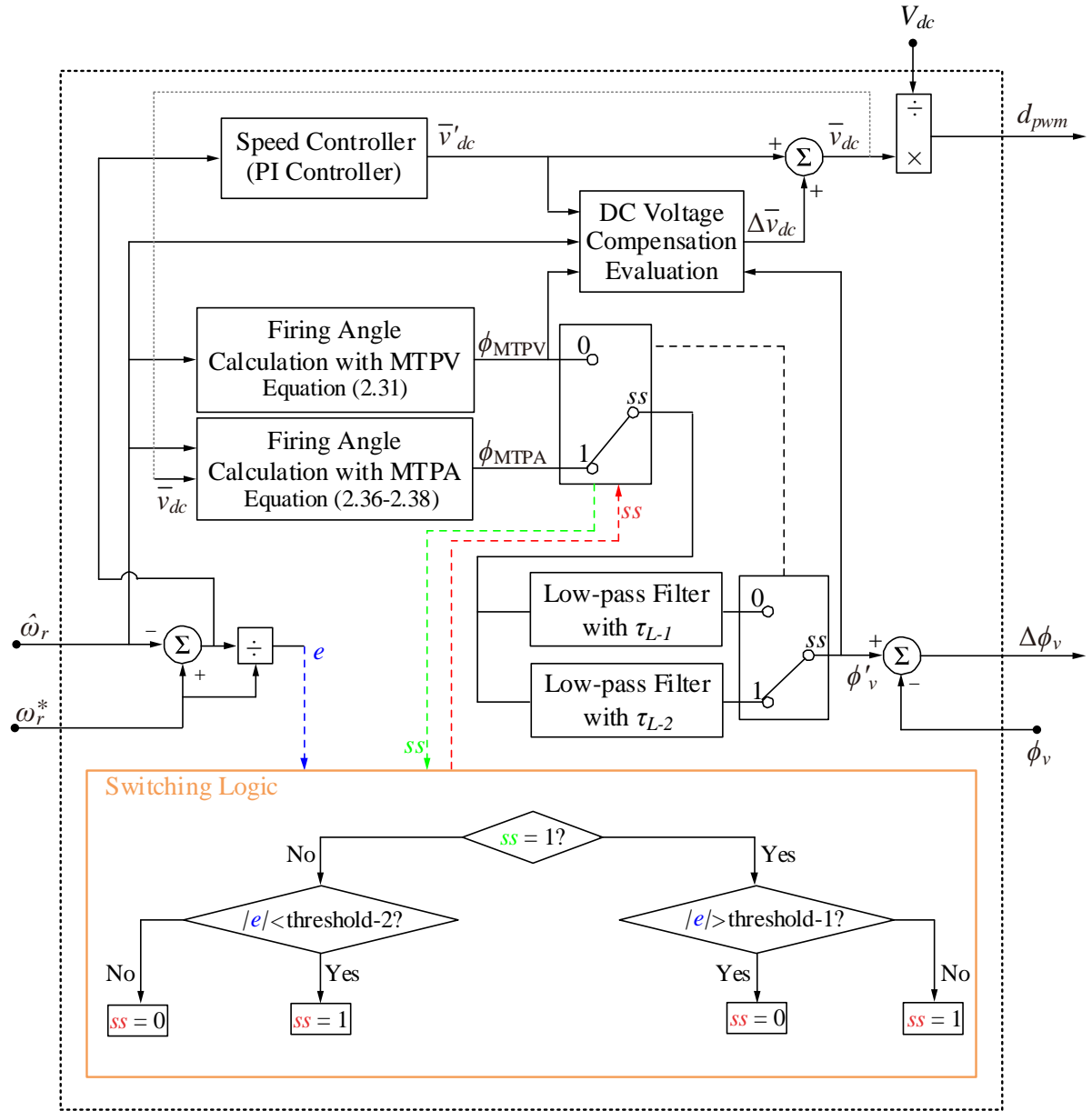
Figure 2.7 Diagram of the proposed hybrid control method for BLDC motors.

To distinguish between the transient and steady-state operations, as well as enable the transition between them, the absolute value of e is compared with some assumed thresholds (i.e., threshold-1 and threshold-2, as shown in Figure 2.7, which may be defined for a considered electromechanical application and the given BLDC motor). Knowing such thresholds, if the

system originally operates in a steady state (switching state denoted as *ss* is at 1), once the absolute value of *e* exceeds the threshold-1, a transient can be identified and the state *ss* is switched to 0. Also, if the system operates in a transient (i.e., *ss* = 0), once the absolute value of *e* becomes less than the threshold-2, then the system is assumed to reach a steady state and the state *ss* is switched to 1. The proper values for threshold-1 and threshold-2 may be set based on the system parameters and dynamic performance requirements. Accordingly, the control logic used to switch between the MTPV and the MTPA is based on the system operating conditions as is illustrated in Figure 2.7.

In each case, the effective dc voltage $\bar{v}_{dc}$ is regulated with a PI controller to achieve the desired speed, as shown in Figure 2.7. However, it should be noted that the levels of average dc voltage required to operate the MTPV and the MTPA are different. In order to achieve the transition between MTPV and MTPA, the output of the PI regulator is also compensated as shown in Figure 2.7. This compensation is needed since for a given operating point defined by the torque and speed while driving a particular mechanical load, the average dc voltage $\bar{v}_{dc}$ and the corresponding angle ϕ'_v would be different for the MTPV and the MTPA operations, respectively. Therefore, a voltage compensation $\Delta\bar{v}_{dc}$ is introduced to deal with the change in $\bar{v}_{dc}$. This value is defined as:

$$\Delta\bar{v}_{dc} = \bar{v}_{dc}(\phi'_v) - \bar{v}'_{dc}, \tag{2.40}$$

where $\bar{v}_{dc}(\phi'_v)$ is the average dc voltage corresponding to the current firing angle; $\bar{v}'_{dc}$ denotes the un-compensated average dc voltage that comes out of the speed regulator, as depicted in Figure 2.7. This value is assumed to be followed with the firing angle of MTPV, which means the $\bar{v}'_{dc}$ is corresponding to the average dc voltage operating with MTPV.

With this definition, the compensation is approximately equal to 0 during the MTPV operation and becomes activated during the switch to the MTPA operation. When the steady state is reached

and the MTPA method is again enabled, the compensation becomes approximately equal to $\bar{v}_{dc}(\phi_{MTPA}) - \bar{v}'_{dc}$. (The approximation is caused by the low-pass filters and the influenced period is relatively short.)

Since the compensation is only needed during the steady-state operation in MTPA, the steady-state equations can be considered for evaluating $\bar{v}_{dc}(\phi'_v)$. Reordering (2.28), the steady state dc voltage is expressed as

$$\bar{v}_{dc}\left(\phi'_v\right) = \frac{4\bar{T}_e}{3P} \frac{r_s^2 + \omega_r^2 L_{ss}^2}{r_s \lambda'_m + \omega_r \lambda'_m (r_s^2 + \omega_r^2 L_{ss}^2)} \frac{\pi}{2\cos\phi'_v + 2\tau_s \sin\phi'_v}. \tag{2.41}$$

However, the electromagnetic torque is hard to measure from the actual machine. To calculate the torque, the $\bar{v}'_{dc}$ which is assumed to be with the firing angle of MTPV is considered again. Replacing firing angle ϕ'_v in (2.28) with the firing angle of MTPV operation ϕ_{MTPV}, the steady state torque in MTPV operation can be expressed as

$$\bar{T}_e = \frac{3P}{4} \lambda'_m \frac{r_s \dfrac{2}{\pi} \bar{v}'_{dc} \cos\phi_{MTPV} + \omega_r L_{ss} \dfrac{2}{\pi} \bar{v}'_{dc} \sin\phi_{MTPV} - r_s \omega_r \lambda'_m}{r_s^2 + \omega_r^2 L_{ss}^2}. \tag{2.42}$$
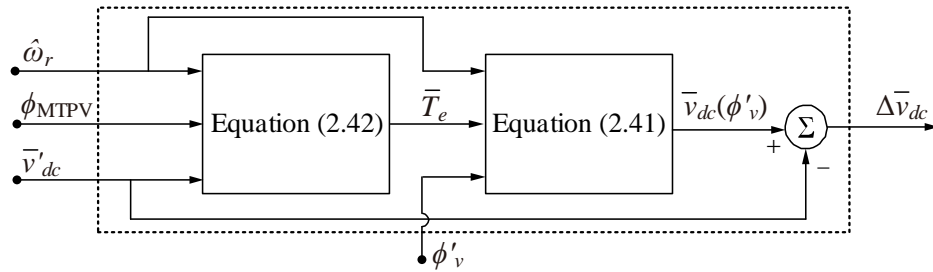
Figure 2.8 Diagram depicting the voltage compensation calculation used in Figure 2.7.

A diagram depicting the calculation of the average dc voltage compensation is shown in Figure 2.8. The averaged torque is first calculated using (2.42) with the MTPV firing angle ϕ_{MTPV} and its

29

corresponding dc voltage $\bar{v}'_{dc}$ (i.e., the output of the PI controller). This equation is also based on the rotor speed which could be estimated from (2.18). Then, the obtained averaged torque together with the current total firing angle ϕ'_v and the estimated speed are as the inputs of (2.41). The compensated dc voltage is obtained and the compensation could be further calculated by deducing the dc voltage directly from the PI controller. The effective dc voltage is then adjusted accordingly by changing the duty cycle of the PWM.

In order to avoid sudden changes in the firing angle values and the average dc voltage commands, which may cause spikes in the torque, the lower-pass filters (LPFs) are utilized to smoothen the transition. The LPFs used in this paper are assumed to be of the following form

$$\text{LPF}(s) = \frac{1}{\tau_L s + 1}, \tag{2.43}$$

where τ_L is the time constant. For better performance, similar to different threshold-1 and threshold-2, different time-constants τ_{L-1} and τ_{L-2} are used depending on whether the transition is from the MTPA to the MTPV, or from the MTPV to the MTPA, respectively, as shown in Figure 2.7.

2.4 Computer Studies

Here, performance of the proposed hybrid control method is verified against the conventional MTPV and MTPA techniques, as well as the COM where the advanced firing angle is set to 0 (i.e., $\phi'_v = \phi_v = 0°$). For this purpose, the system depicted in Figure 2.1 has been implemented in MATLAB/Simulink in full detail with the subject BLDC motor (with parameters listed in Appendix A.1). The controller parameters have been tuned properly and their values are summarized in Appendix B.1. Specifically, the speed PI controller is tuned to make the closed-loop step response critically damped/overdamped. Also, in the following computer studies, the

30

load mechanical torque is assumed to be quadratic with respect to the rotor speed, as $T_m = K_{m1}\omega_r^2$ (as listed in Appendix C.1).

First, it is assumed that the system is initially operating in a steady state at operating point A with $\omega_r^* = 600$rad/s (machine speed $n = 1432.39$ rpm). Then, at $t = 3.3$s, the rotor speed command is stepped up to 800rad/s ($n = 1909.86$ rpm). After a short period of transient, the machine reaches a new steady-state operating point B. These two operating points are shown in Figure 2.9, based on the respective steady-state torque-speed characteristics of the BLDC motor with different control techniques. It is important to notice that for a given operating point, the MTPV and the MTPA require different average dc voltages, as indicated in Figure 2.9. The transient responses observed in several system's variables are shown in Figures 2.10–2.12.
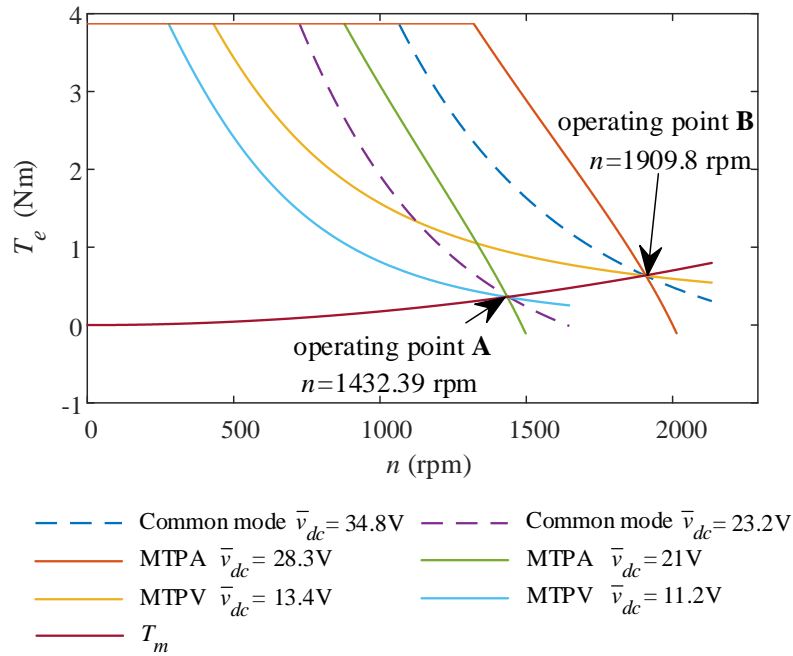
Figure 2.9 Steady-state torque-speed characteristics of the BLDC motor assuming MTPV, MTPA, and COM. The mechanical load torque characteristic intercepts indicating the considered operating points.

As it can be observed in Figures 2.10–2.12, similar to the MTPV, the proposed method has a much faster transient response compared to the conventional MTPA and common mode operation (i.e., almost 0.27s vs. 1.04s vs. 1.54s of settling time, respectively). The efficiency of the BLDC motor at the two considered operating points using different control methods are summarized in Table 2.1. It is also seen in Table 2.1 that, similar to the MTPA, the proposed hybrid method achieves significantly higher efficiency compared to the conventional MTPV and common mode operation (i.e., 96.86% vs. 15.18% vs. 87.9% at 600 rad/s, and 95.85% vs. 25.27% vs. 77.36% at 800 rad/s, respectively). It is noted that the significantly lower efficiency of MTPV compared to other methods is also expected from Figure 2.10(c)-(d), where the stator current for the MTPV is considerably higher than the one with other methods, resulting in increased losses and lower efficiency.
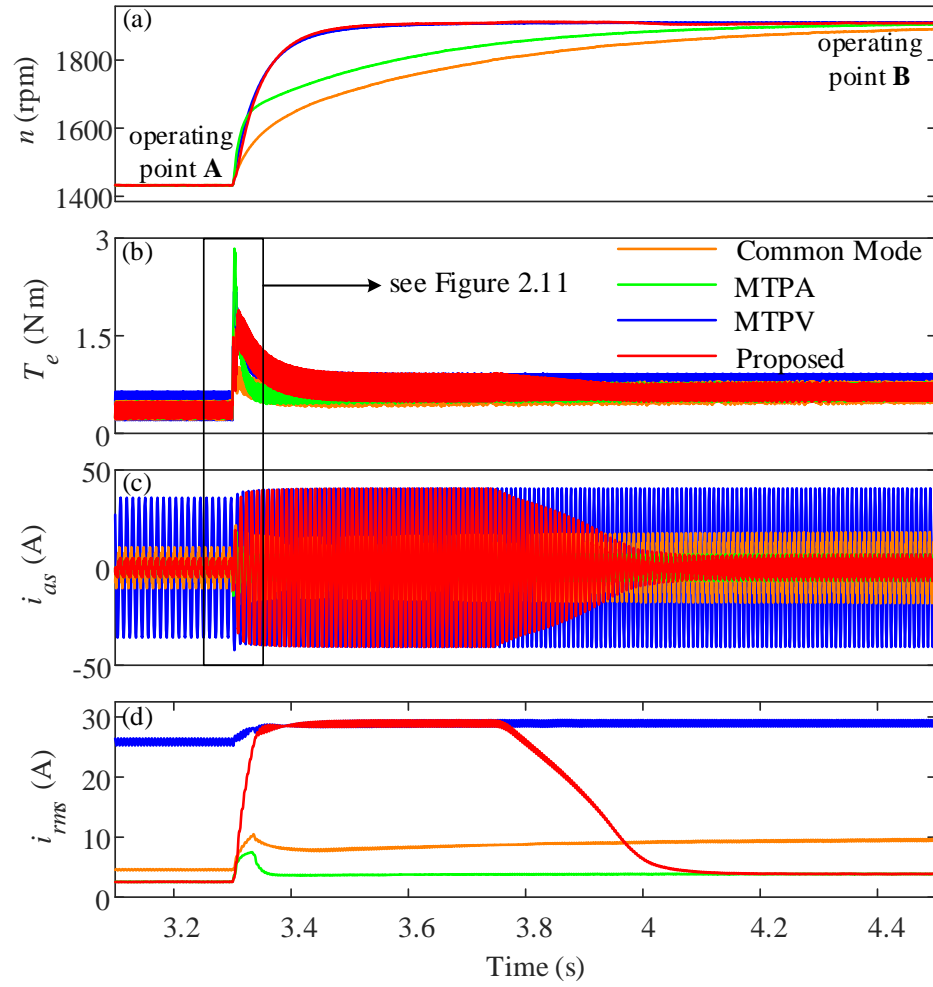
Figure 2.10 Transient response of the subject control methods when the command speed is increased at $t = 3.3$s **for several system variables: (a) mechanical speed, (b) electromagnetic torque, (c) phase current, and (d) root mean square of the phase current.**

Table 2.1 Efficiency of the BLDC motor with different control methods for operating points A and B

Operating Point	COM	MTPV	MTPA & Proposed
A (n =1432.39 rpm)	87.90%	15.18%	96.86%
B (n = 1909.86 rpm)	77.36%	25.27%	95.85%
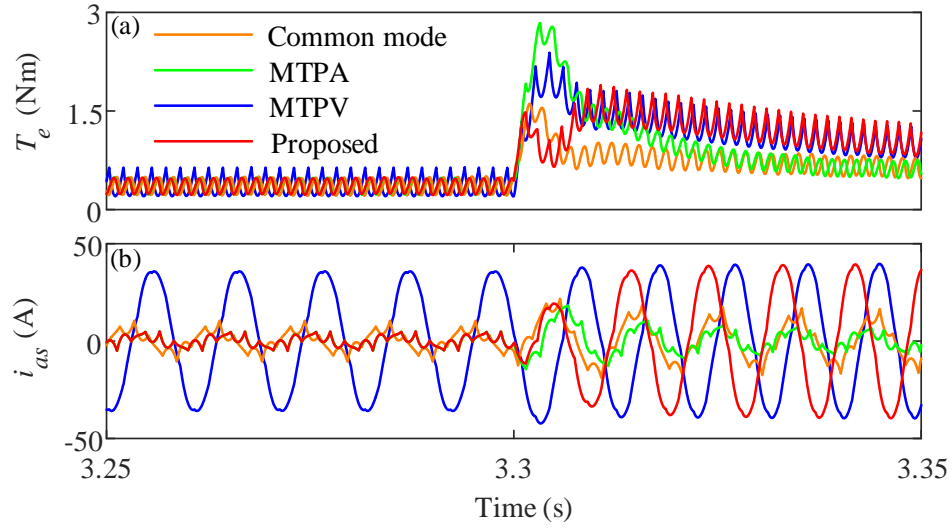
Figure 2.11 Magnified view of the rectangular in Figure 2.10 for the variables: (a) electromagnetic torque, and (b) phase current.
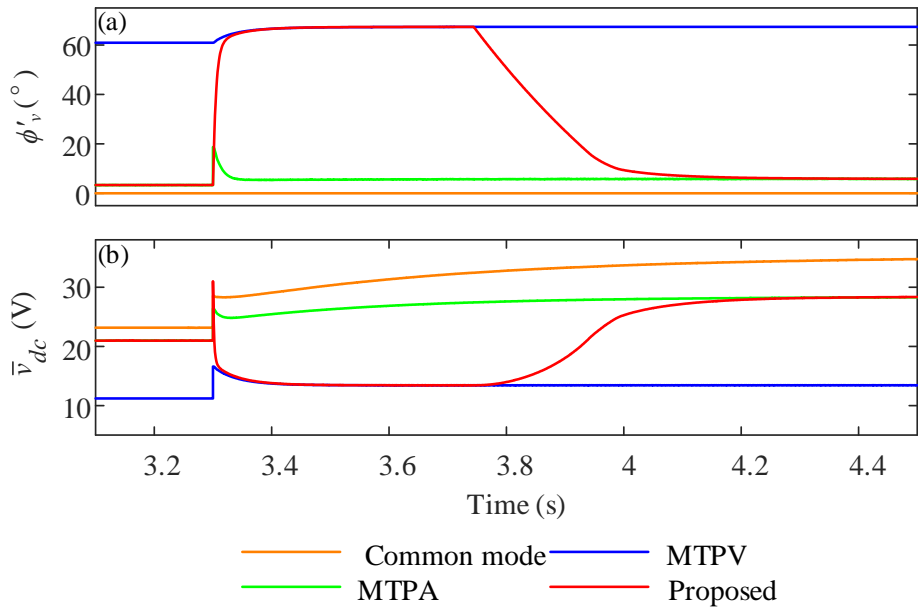
Figure 2.12 Transient response of the subject control methods for several system variables when the command speed changes at $t = 3.3$ s: (a) firing angle, and (b) average dc voltage.

Overall, it is verified that the proposed hybrid control method of BLDC motors inherits the advantages of both the MTPV (in transient) and the MTPA (in steady state) methods and provides a practical solution for electromechanical applications that need both fast transient response and high steady-state energy efficiency.

Chapter 3: MTPA and MTPV Strategies of BLDCs with 120-Degree Operation

Many BLDC motor drive systems are commonly controlled using the 120-degree commutation method since this method naturally achieves an approximation of the MTPA operation with the common mode of operation. However, due to the winding inductance and commutation process, the fundamental component of the phase current will experience some delays, resulting in a sub-optimal operation that may be especially noticeable for motors with large inductance (and small resistance). A simple and direct method to compensate for the operating-point-dependent commutation angle has been proposed in this chapter. It is shown that a simple PI-control can be used to regulate the averaged *d*-axis current to zero, which restores the MTPA operation and improves the torque-speed characteristic.

Additionally, to fully utilize the torque capability for a given dc voltage, a straightforward MTPV strategy for the 120-degree operation has been developed based on a two-dimensional lookup table. The detailed models are simulated in a loop to store the firing angle that results in the maximum torque corresponding to different dc voltages and machine speeds. With the pre-stored table, the firing angle could be adjusted properly for different operating points and better torque utilization is shown to be achievable. The proposed MTPA and MTPV schemes are demonstrated with detailed simulations of a typical industrial BLDC motor and are shown to be effective over a wide range of operating conditions.

3.1 BLDC Motors with 120-Degree Conduction Logic

In this chapter, the BLDC motor drive systems shown in Figure 2.1 is controlled through operating the individual inverter transistor based on the 120-degree conduction logic depicted in Figure 3.1. Here, the logic is developed with respect to the position θ' which is the summation of the estimated angle $\hat{\theta}$ from (2.19) and the firing angle compensation $\Delta\phi_v$ as shown in Figure 2.1. In this switching logic, the conduction duration of each transistor is reduced to 120 degrees (i.e., $D_{con} = 120°$) and both transistors in the same phase leg turn off twice (for 60 degrees each time) over one electrical revolution.

Additionally, to control the effective dc voltage from a fixed dc supply V_{dc}, the 120-degree conduction logic is also used together with PWM (e.g., non-complementary and complementary PWM mode [59], PWM-ON mode [60]–[61], ON-PWM mode [60], [62], PWM-ON-PWM mode [63], PWM-OFF-PWM mode [64]). Here, the PWM-ON mode is shown in Figure 3.1, wherein only one conducting transistor is PWM-controlled for 60 degrees. This strategy is commonly used due to its simplicity, low torque ripple, and high dc bus utilization [60]–[61]. By changing the duty cycle of the PWM d_{pwm}, the effective dc voltage is changed to $\bar{v}_{dc}$ and the RMS value of the phase voltages is changed as well.
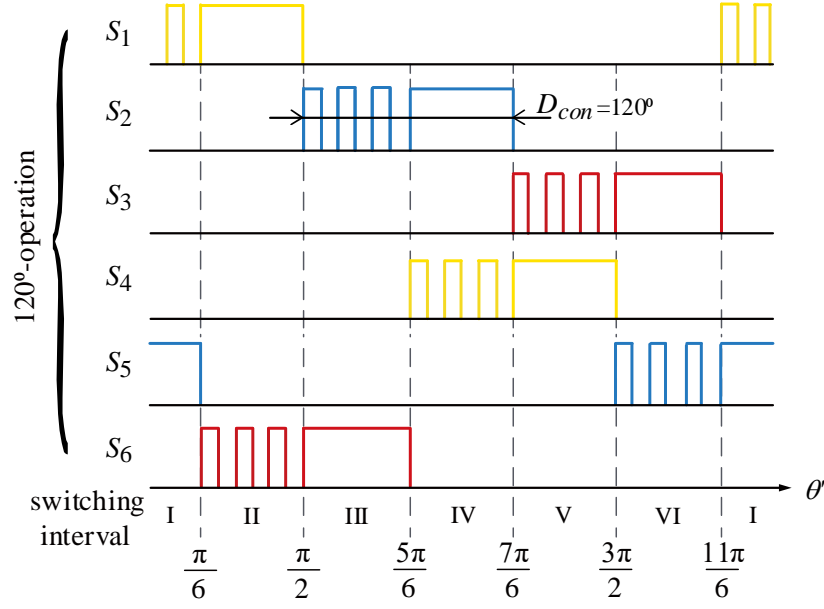
Figure 3.1 Typical commutation logic of the six-step 120-degree VSI operation with PWM-ON mode for the BLDC motors.

The voltage and current waveforms obtained for a typical BLDC motor with firing angle fixed at 30 degrees and the duty cycle of PWM at 1 is shown in Figure 3.2. It can be observed that one switching interval with the time duration T_{sw} consists of two subintervals. For the phase with both transistors off, the corresponding phase current firstly approaches to zero with a commutation period t_{com}. Afterwards, the other two phases conduct the full current during the conduction interval with a length of $t_{cond} = T_{sw} - t_{com}$. This effect of commutation and conduction could be automatically included by the appropriate circuit simulator (e.g., Simulink's SimScape Electrical [56], PLECS [65], etc.).
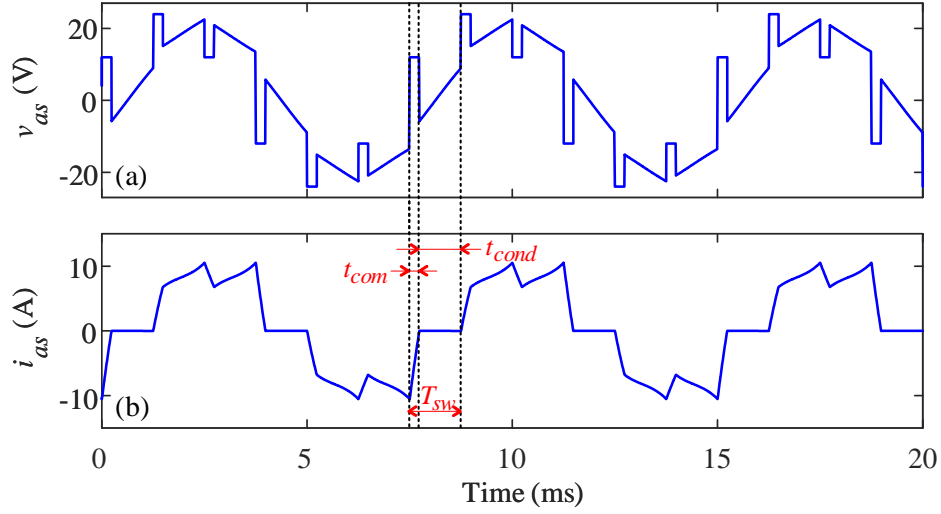
Figure 3.2 Typical waveforms of BLDC motors with 120-degree commutation in COM: (a) phase voltage, (b) phase current.

3.2 MTPA Strategies

For BLDC motors with the 120-degree operation, the waveforms shown in Figure 3.2 is influenced by the duration of the commutation interval t_{com}. Depending on machine parameters and operating conditions, the commutation interval as well as the averaged voltage equations could change dramatically [10]. It becomes difficult to obtain a determined and accurate analytical expression of the firing angle for MTPA operation. Instead, the numerical strategies have been considered.

3.2.1 Conventional Strategy

Conventionally, a BLDC motor with 120-degree conduction logic is assumed to achieve a build-in MTPA operation in the COM, where the Hall sensors are shifted to achieve a fixed 30-degree firing angle. Under this condition, the ideal steady-state performance with standard Hall

sensors will be similar to that depicted in Figure 3.3 (assuming phase *a* as an example). Therein, the alignment of the back EMF and the fundamental component of current is approximately achieved when the advance in firing angle is 30 degrees. Also, the (preceding) commutation point is about 30-degree earlier than the zero-crossing point of the back EMF. However, this is only applicable to the BLDC machines with small inductance, which has been commonly assumed in previous works [66]–[68].

   For BLDC machines with large inductances, the impact of the commutation interval will be magnified and the misalignment between the back EMFs and the fundamental components of currents can become more significant with the conventional 30-degree firing angle, as depicted in Figure 3.4 (see circle).
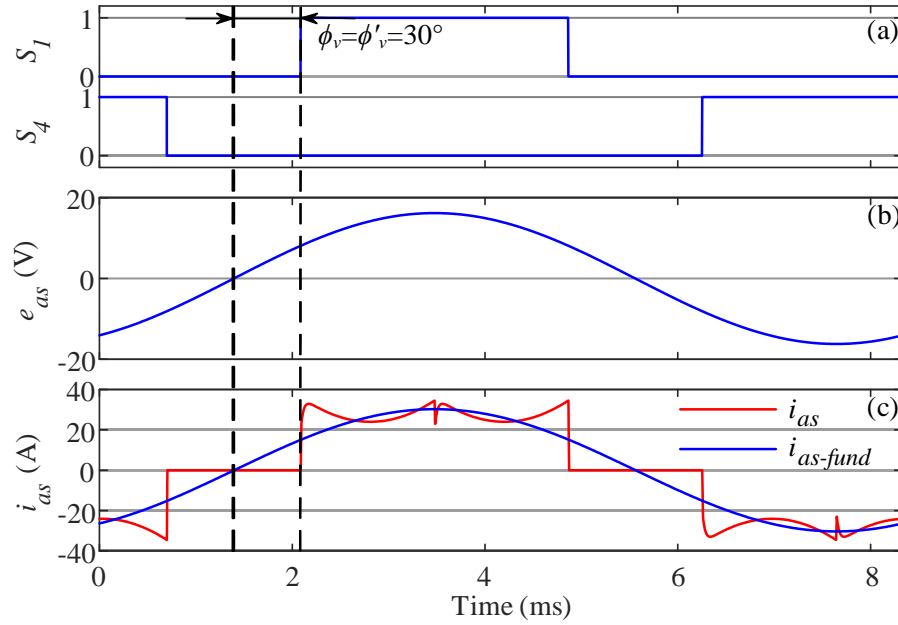
Figure 3.3 Expected operation using conventional MTPA strategy, i.e., in COM (applicable to BLDC motors with small inductance): (a) switching signals related to phase *a*; (b) back EMF; and (c) phase current and its fundamental component.
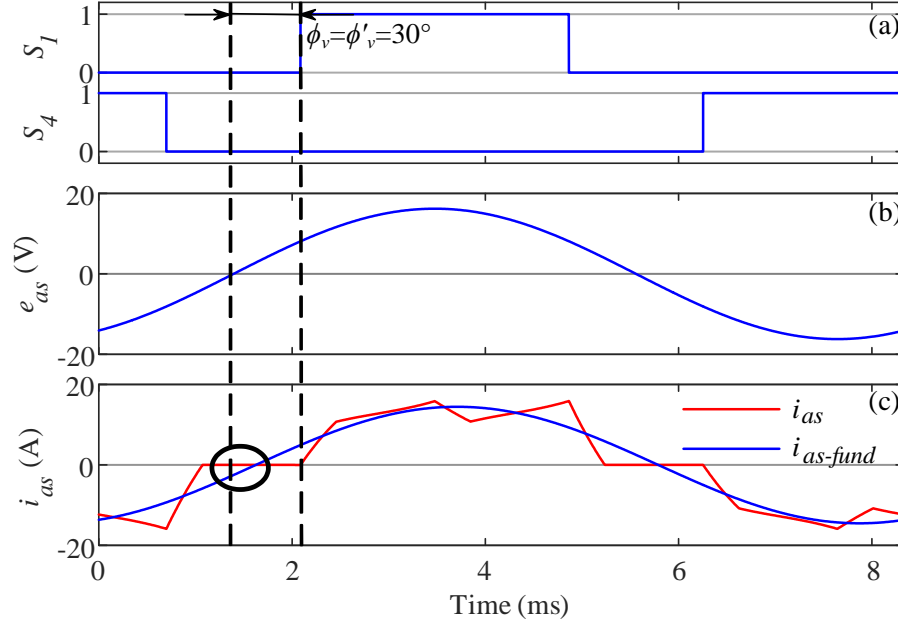
Figure 3.4 Expected operation using conventional MTPA strategy, i.e., in COM (applicable to BLDC motors with large inductance): (a) switching signals related to phase *a*; (b) back EMF; and (c) phase current and its fundamental component.

3.2.2　　Proposed Strategy

To eliminate the commutation errors caused by the commutation presenting in conventional strategy, a simple and straightforward compensation method is developed in this section. The MTPA control aims at maximizing the electromagnetic torque for a given value of phase current [5]. According to (2.12), the torque is proportional to *q*-axis current, while *d*-axis current does not contribute (assuming a round machine). Therefore, for a fixed current magnitude, the electromagnetic torque is maximized when the *d*-axis current is 0. It should be noticed, when the *d*-axis current is zero, the phase current is aligned with the *q*-axis as well as the back EMF voltage which is on the *q*-axis only, based on (2.9). With this alignment, the maximum current utilization will be achieved. To maintain a zero *d*-axis current, the advance in firing angle needs to be compensated by a proper controller and the compensation is to be incorporated into the commutation logic with (2.15) and (2.24).

Beforehand, to effectively control the *d*-axis current at 0, the current ripple (shown in Figure 3.5) has to be eliminated. To achieve this goal, a high-order filter is introduced in [37] to obtain the fundamental component of the phase current. In this paper, a simple and easy-to-implement method is proposed based on averaging the current components in *qd*-rotor reference frame within a prototypical switching interval as

$$\bar{i}_{ds}(t) = \frac{1}{T_{sw}} \int_{t-T_{sw}}^{t} i_{ds}(\xi) d\xi, \qquad T_{sw} = \frac{\pi}{3\omega_r}. \tag{3.1}$$

Here, the averaging is calculated over one interval with duration T_{sw}, since the currents in *qd*-rotor reference frame have repeating patterns as shown in Figure 3.5. Therefore, with the averaging over only 1/6 of one electrical revolution, this method leads to fast transient and computational efficiency.
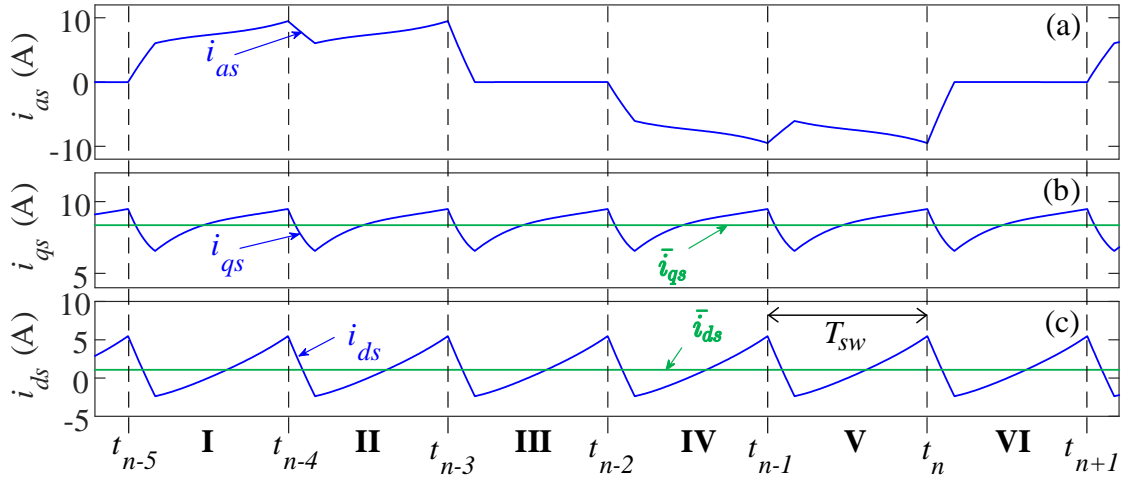
Figure 3.5 Steady state current waveforms of the 120-degree operation with 30-degree advance in firing angle: (a) phase current, (b) *q*-axis current, and (c) *d*-axis current.
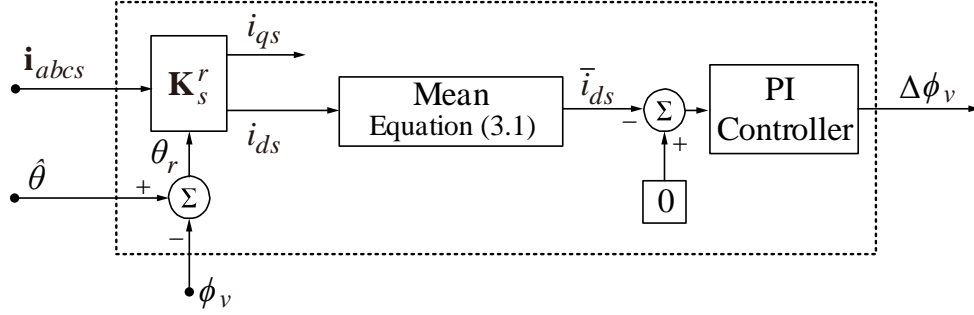
Figure 3.6 Implementation of the control scheme to compensate the advance in firing angle for automatically maintaining the MTPA operation.

Thereafter, it becomes possible to implement a simple PI controller that regulates the value of $\bar{i}_{ds}$ to zero. The corresponding controller is shown in Figure 3.6. This controller measures and then transforms the motor physical currents into the rotor reference frame using (2.8). The obtained d-axis current is averaged using (3.1), and then effectively regulated at zero by a PI controller. The output of the PI controller is the compensation of the firing angle $\Delta\phi_v$, which is added to the estimated angular position $\hat{\theta}$ (shown in Figure 2.1).

The performance of the proposed compensation method for a BLDC machine with large inductance is shown in Figure 3.7. As seen, the proposed method can align the back EMF with the respective fundamental component of current by adjusting the advance in firing angle. It is also seen in Figure 3.7 that the (preceding) commutation point is earlier than the zero-crossing point of the back EMF by an angle larger than 30 degrees, which indicates the advance in firing angle is greater than 30 degrees.
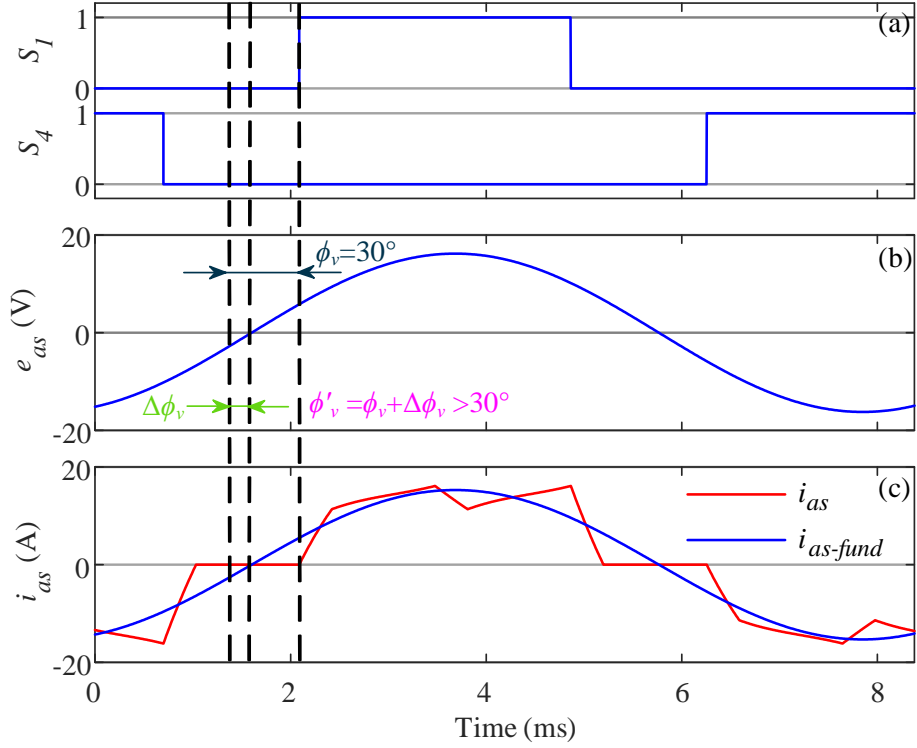
Figure 3.7 Expected operation using the proposed compensation method for MTPA operation (applicable to BLDC motors with large and/or small inductance): (a) switching signals related to phase *a*; (b) back EMF; and (c) phase current and its fundamental component.

Additionally, the firing angle advancement characteristic over a wide range of operating speed is obtained for a typical industrial BLDC (parameters listed in Appendix A.1) with a fixed effective dc voltage (i.e., $\bar{v}_{dc} = 36\text{V}$). Simulating the detailed model of the system in Figure 2.1 with the proposed MTPA strategy in Figure 3.6 over the desired range of speed, the compensated firing angle ϕ'_v is calculated with the output of the PI controller. The resulting angle is depicted in Figure 3.8. As observed in Figure 3.8, the compensated firing angle is generally different from the conventional approximation of constant 30 degrees and is dependent on the operating point. It is also seen that the difference can be significant (e.g., up to 13.3 degrees) and should not be neglected especially for motors with large inductance. However, with the proposed MTPA method

and using the PI controller, the firing angle can be accurately adjusted over a wide range of operating conditions (i.e., speed, dc voltage, load, etc.).
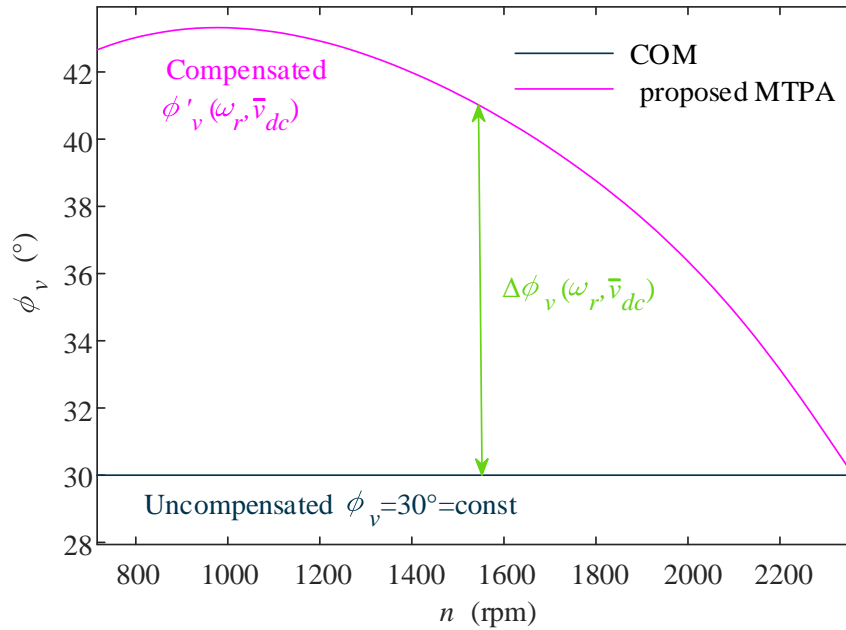
Figure 3.8 The advance in firing angle over a range of speeds as obtained with the proposed and conventional MTPA methods (with dc voltage fixed at 36 V).

3.3　Proposed MTPV Strategy

The MTPV control aims at maximizing the electromagnetic torque for a given dc voltage [5]. This could be achieved by setting the derivative of steady-state torque equation with respect to the firing angle at zero as

$$r_s \frac{\partial V_{qs}}{\partial \phi'_v} - L_{ss}\omega_r \frac{\partial V_{ds}}{\partial \phi'_v} = 0. \tag{3.2}$$

For the 120-degree operation, the operating-point-dependent commutation interval and voltage waveform make it difficult to derive an explicit equation for the firing angle from (3.2). If the commutation interval is neglected (applicable for motor with small inductance), the averaged voltages in *qd*-domain may be expressed as [10]

45

$$\bar{v}_{qs} = \frac{\sqrt{3}}{\pi}\bar{v}_{dc}\cos(\phi'_v - \frac{\pi}{6}) + \omega_r\lambda'_m\left[\frac{1}{2} - \frac{3\sqrt{3}}{4\pi}\cos(2\phi'_v - \frac{\pi}{3})\right], \tag{3.3}$$

$$\bar{v}_{ds} = -\frac{\sqrt{3}}{\pi}\bar{v}_{dc}\cos(\phi'_v - \frac{2\pi}{3}) - \frac{3\sqrt{3}}{4\pi}\omega_r\lambda'_m\cos(2\phi'_v + \frac{\pi}{6}). \tag{3.4}$$

Taking (3.3) and (3.4) into (3.2),

$$0 = r_s\left[-\frac{\sqrt{3}}{\pi}\sin(\phi'_v - \frac{\pi}{6}) + \frac{3\sqrt{3}}{2\pi}\frac{\omega_r\lambda'_m}{\bar{v}_{dc}}\sin(2\phi'_v - \frac{\pi}{3})\right]$$
$$-\omega_r L_{ss}\left[\frac{\sqrt{3}}{\pi}\sin(\phi'_v - \frac{2\pi}{3}) + \frac{3\sqrt{3}}{2\pi}\frac{\omega_r\lambda'_m}{\bar{v}_{dc}}\sin(2\phi'_v + \frac{\pi}{6})\right]. \tag{3.5}$$

Reordering (3.5), one can get a fourth-order function with respect to $\sin\phi'_v$ as

$$0 = \frac{144}{\pi^2}\omega_r^2\tau_v^2(\omega_r^2\tau_s^2 + 1)\sin^4(\phi'_v) - \frac{24}{\pi}\omega_r\tau_v(\omega_r^2\tau_s^2 + 1)\sin^3(\phi'_v)$$
$$+ (\omega_r^2\tau_s^2 + 1)(4 - \frac{144}{\pi^2}\omega_r^2\tau_v^2)\sin^2(\phi'_v) + \frac{6}{\pi}\omega_r\tau_v(5\omega_r^2\tau_s^2 + 1)\sin(\phi'_v). \tag{3.6}$$
$$+ \frac{9}{\pi^2}\omega_r^2\tau_v^2(\omega_r^2\tau_s^2 + 2\sqrt{3}\omega_r\tau_s + 3) - (3\omega_r^2\tau_s^2 + 2\sqrt{3}\omega_r\tau_s + 1)$$

The nonlinear equation (3.6) is still difficult to solve analytically, and only numerical/iterative solution is possible. Instead, another type of numerical methods based on the lookup table is considered in this thesis.

The MTPV operation depends on the dc voltage, the operating speed, and the machine parameters. Therefore, it is assumed that the firing angle corresponding to the MTPV operation ϕ_{MTPV} can be expressed as an algebraic equation of the effective dc voltage $\bar{v}_{dc}$ and the machine speed ω_r for a given BLDC motor. To establish the lookup table that can be used as an algebraic function $\phi_{\mathrm{MTPV}}(\bar{v}_{dc}, \omega_r)$, the detailed model of the BLDC systems in Figure 2.1 is run in a loop

46

Algorithm. Establishing the algebraic equation for MTPV firing angle using detailed simulation.

1. **for** $V_{dc}=V_{dc\text{-min}}$ **to** $V_{dc\text{-max}}$ **step** $V_{dc\text{-step}}$

2.   **for** $\omega_r=\omega_{r\text{-min}}$ **to** $\omega_{r\text{-max}}$ **step** $\omega_{r\text{-step}}$

3.   Initialize the maximum torque $T_{e\text{-max}}=0$

4.   Initialize the firing angle corresponding to the maximum torque $\phi_{\text{MTPV}}=\phi_{v\text{-min}}$

5.   **for** $\phi_v=\phi_{v\text{-min}}$ **to** $\phi_{v\text{-max}}$ **step** $\phi_{v\text{-step}}$

6.   Initialize the detailed model

7.   Start simulation

8.   Compare the simulated averaged electromagnetic torque T_e with the $T_{e\text{-max}}$

9.   Re-assign the value of $T_{e\text{-max}}$ with T_e if T_e is larger

10.   Re-assign the value of ϕ_{MTPV} with ϕ_v if T_e is larger

11.   **end for**

12.   Save $T_{e\text{-max}}$, ϕ_{MTPV} in 2-D lookup tables in terms of V_{dc}, ω_r

13.   **end for**

14.**end for**

Figure 3.9 Pseudo-code for establishing the lookup table of the firing angle for the proposed MTPV strategy using detailed simulation.

over a range of interesting operating conditions. The pseudo-code of this procedure is presented in

Figure 3.9 to formulate a two-dimensional lookup table for the algebraic function $\phi_{\text{MTPV}}(\overline{v}_{dc},\omega_r)$.

For a typical industrial BLDC motor with parameter listed in Appendix A.1, the lookup table

generated by the pseudo-code shown in Figure 3.9 are demonstrated in Figure 3.10. It is seen in

Fig. 3.10, the firing angles of MTPV operation are quite different from the 30 degrees of the COM

as well as the angles obtained from the proposed MTPA method.

Thereafter, it becomes possible to interpolate/extrapolate from this lookup table for proper

adjustment of firing angle to achieve the MTPV operation for BLDCs with 120-degree conduction

logic over a range of operating conditions.
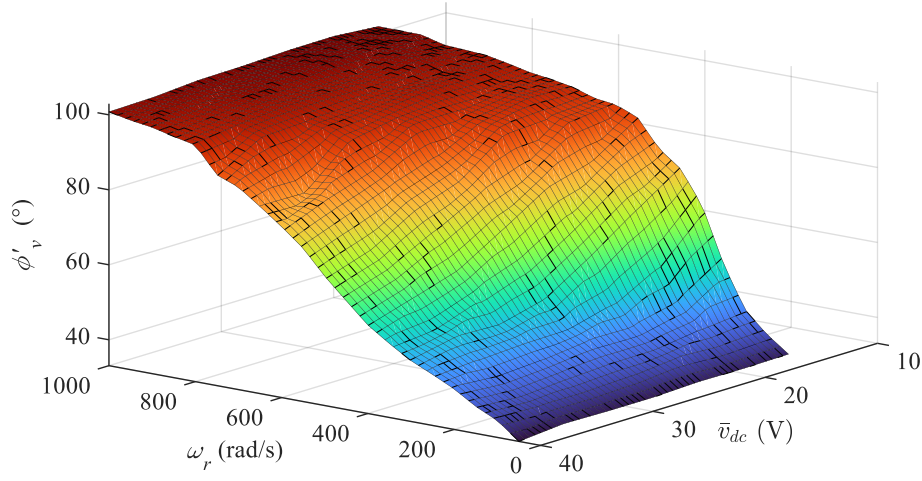
Figure 3.10 A lookup table of firing angle with respect to the effective dc voltage and the machine speed for a BLDC motor to operate in MTPV condition.

3.4   Computer Studies

The proposed MTPA and MTPV methods is verified against the common mode of operation with firing angle fixed at 30 degrees. The system depicted in Figure 2.1 has been implemented in MATLAB/Simulink in full details with the subject BLDC motor drive (with parameters listed in Appendix A.1). The parameters of the controller (i.e., the PI controller in the proposed MTPA strategy) have been properly tuned and are listed in Appendix B.2.

Firstly, to verify the proposed MTPA method against the conventional MTPA method operating in COM, the steady-state performance of the motor operating at 1800 rpm with the effective dc voltage fixed at 36V is shown in Figure 3.11. As seen in Figure 3.11(c), the machine can achieve higher output torque (i.e., 1.9731Nm vs 1.8475Nm) with the proposed method compared to the conventional method. Also, since the proposed method achieves the actual MTPA operation, the

48

ratio of the average torque to the phase current magnitude is also higher with the proposed method (i.e., 0.1765 vs 0.1740), as seen in Figure 3.11(d).

Also, the proposed MTPV strategy is verified against the conventional common mode of operation. For better demonstration, the dc supply is adjusted to drive the same mechanical load (i.e., at the same torque and speed). Specifically, the BLDC motor system in COM operates at 1800 rpm and 1.85 Nm when the dc voltage is 36 volts. With the same mechanical load, the effective dc voltage is to be decreased to 25.9 volts for operation with the proposed MTPV method. The corresponding steady-state performance of these two methods is shown in Figure 3.12. It can be observed that the voltage and current waveforms of the MTPV operation have been changed significantly with a firing angle far away from the conventional 30 degrees. Though the torque ripple increases, the ratio between the averaged torque and dc voltage are largely increased by the proposed MTPV method (i.e., 1.85/25.9=0.0714 Nm/V vs. 1.85/36=0.0514 Nm/V), which indicates a better voltage utilization.
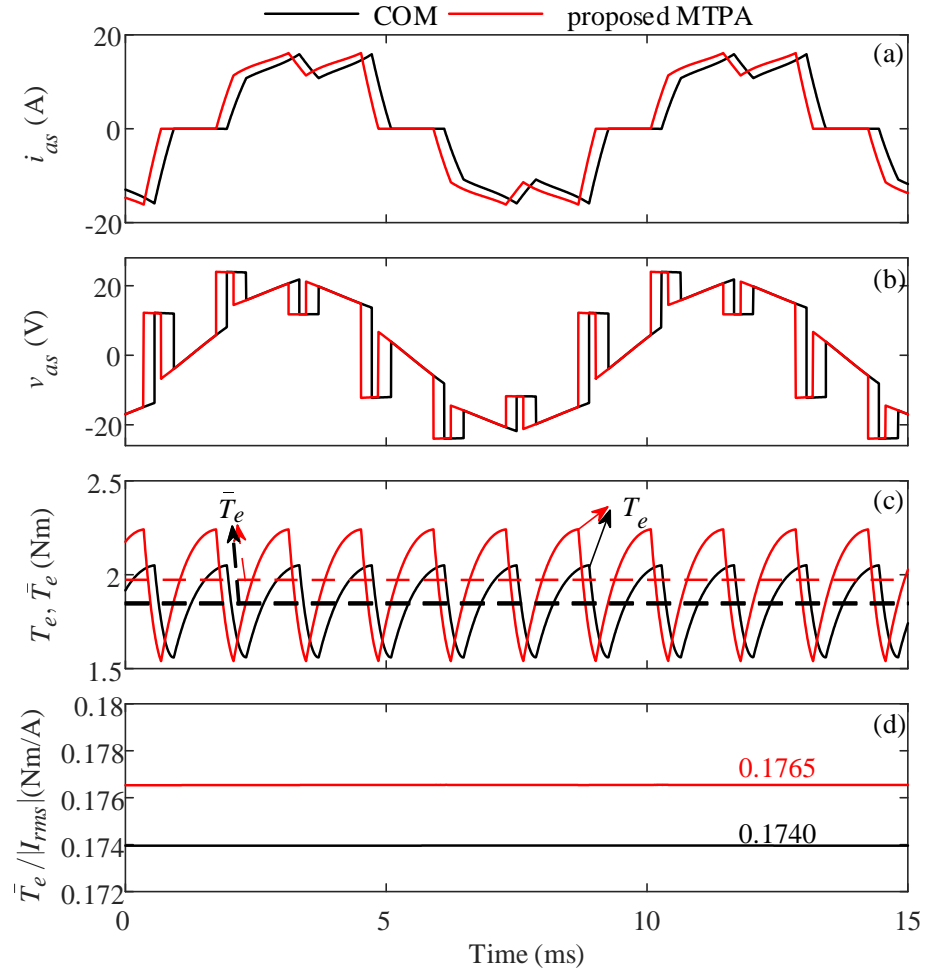
Figure 3.11 Simulated steady-state operation of the considered BLDC motor at 1800 rpm with the conventional COM and the proposed MTPA strategy: (a) phase current, (b) phase voltage, (c) electromagnetic torque and its average value, and (d) ratio of the averaged torque over the phase current magnitude.
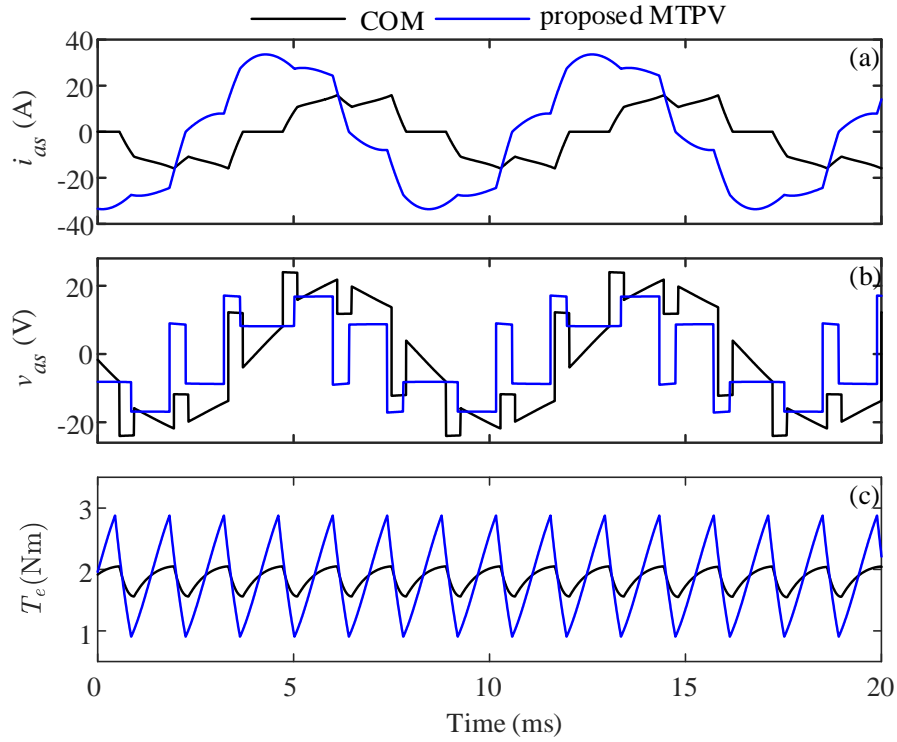
Figure 3.12 Simulated steady-state operation of the considered BLDC motor at 1800 rpm and 1.85 Nm by COM with 36 volts dc supply and the proposed MTPV operation with 25.9 volts dc supply: (a) phase current, (b) phase voltage, and (c) electromagnetic torque.
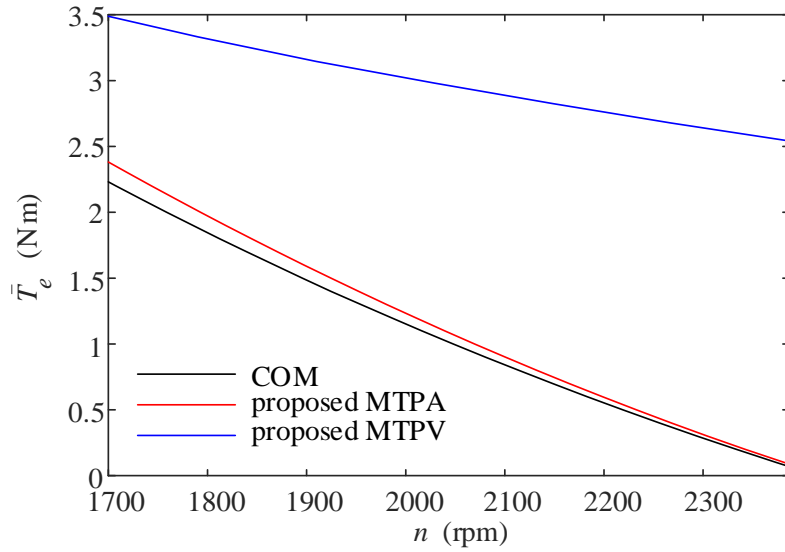
Figure 3.13 Simulated steady-state torque-speed characteristics of the BLDC motor with conventional common operating mode, proposed MTPA and MTPV methods.

Finally, to overview the performance of the proposed MTPA, MTPV methods against the conventional COM, the calculated steady-state torque-speed characteristics for different methods with dc supply at 36 volts are shown in Figure 3.13. The proposed MTPA has demonstrated an overall higher output torque over a wide range of speed when compared with the conventional MTPA implementation by fixing the firing angle at 30 degrees. Nevertheless, the highest torque output could be achieved by the proposed MTPV strategy which achieves the highest voltage utilization for a given dc voltage.

Chapter 4: Extended Conduction of BLDC Motors Under MTPA Control

Recently, the attention has been given to the operation of BLDC motors with conduction angles between 120 and 180 degrees (e.g., 150 degrees, 160 degrees, etc.), where some benefits such as low torque ripple may be gained. Specifically, the increasing trend of phase voltage by increasing the conduction angle is observed from the benchmark studies in [51]. Therefore, operating with an extended conduction angle provides a voltage extension above the conventional 120-degree operation with PWM. The extended operation is expected to reduce the torque ripple, current ripple, and iron losses caused by the PWM [53].

Meanwhile, considering the property of high efficiency, the MTPA strategy proposed in Chapter 3 for 120-degree operation will be extended over the entire range of voltage adjustment. Regulating the averaged d-axis current to zero using a PI controller, the firing angle could be adjusted properly to align the phase currents and the corresponding back EMFs for the extended conduction methods beyond the 120-degree operation.

For the purpose of verification, the proposed controller has been discretized and implemented in a digital signal processor (DSP). Both the simulations in MATLAB/Simulink and the hardware experiments based on the DSP demonstrate the steady-state and transient performance of the proposed scheme and its benefits over the conventional alternative methods.

4.1 Generalized Conduction Logic

In the conventional 180-degree and 120-degree modes of operation with the fixed firing angle (i.e., $\Delta\phi_v = 0$), the switching of the six inverter transistors could be determined directly based on the signals coming from the Hall-effect sensors. Specifically, from Figure 2.2 for 180-degree operation, the switching signals of the upper transistors S_1, S_2 and S_3 are coming directly from the Hall sensor outputs h_1, h_2 and h_3, as depicted in Figure 2.3(a), respectively. Meanwhile, the switching signals of the lower transistors S_4, S_5 and S_6 are complementary to those of the upper transistors. For the 120-degree operation, the switching logic shown in Figure 3.1 is a slight modification of the same Hall signals [shown in Figure 2.3(a)]. Specifically, the turn "OFF" of each transistor remains unchanged, and it coincides with the Hall sensor outputs in its sequence. However, the turned "ON" moment is delayed by 60 degrees and is obtained from the previous Hall signal (corresponding the previous phase within the considered sequence). Because of that, the conduction period becomes reduced to 120 degrees in one electrical cycle for each inverter switch.

It is observed that the 120-degree can be obtained from the 180-degree Hall sensor signals by delaying the turn "ON" time by 60 degrees (which is effectively done using the preceding Hall sensor signal). To extend the switching logic, the conduction angle D_{con} may be in the range between 120 and 180 degrees in one electrical cycle as depicted in Figure 4.1. The delay angle can be defined as

$$\alpha_d = 180° - D_{con},$$ (4.1)

where

$$120° \leq D_{con} \leq 180° \text{ (i.e. } 60° \geq \alpha_d \geq 0).$$ (4.2)
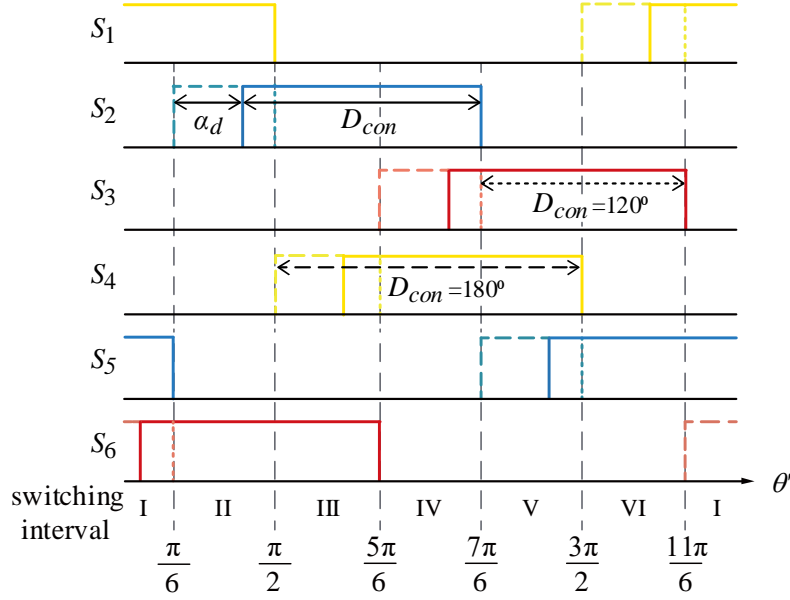
Figure 4.1 A generalized commutation logic of VSI operation of BLDC motors with conduction angle between 120 and 180 degree.

Thereafter, it becomes possible to express the commutation logic that covers any angle from 120 to 180 degrees by simply specifying the appropriate delay angle α_d . For the extended conduction methods, the commutation points can no longer be determined directly from the Hall sensor signals as it was for the conventional 180-degree and 120-degree modes with some fixed firing angles. Instead, the compensated position θ' based on the estimated position $\hat{\theta}$ from (2.19)–(2.20) is used in the switching logic. Here, for DSP implementation with fast sampling rate, the position estimation for point m in (2.19) is discretized as

$$\hat{\theta}(m) = \theta_H(t_n) + mT_I\hat{\omega}_r, \qquad 0 \le m \le M , \qquad (4.3)$$

where m is also referred as the mth fast sampling point between t_n and t_{n+1} [exemplified with switching interval V in Figure 2.3(c)]; M is the total number of samples within the considered switching interval; and T_I is the fast hardware sampling period (i.e. hardware counter period). The

estimated speed and fast-sampling counter in (4.3) need to be reset with any updates of the quantized position.

Considering the estimated position and the extended commutation logic, the typical waveforms of the phase voltage and current obtained for 120-degree, 140-degree, 160-degree and 180-degree operation with a typical BLDC motor are shown in Figure 4.2.
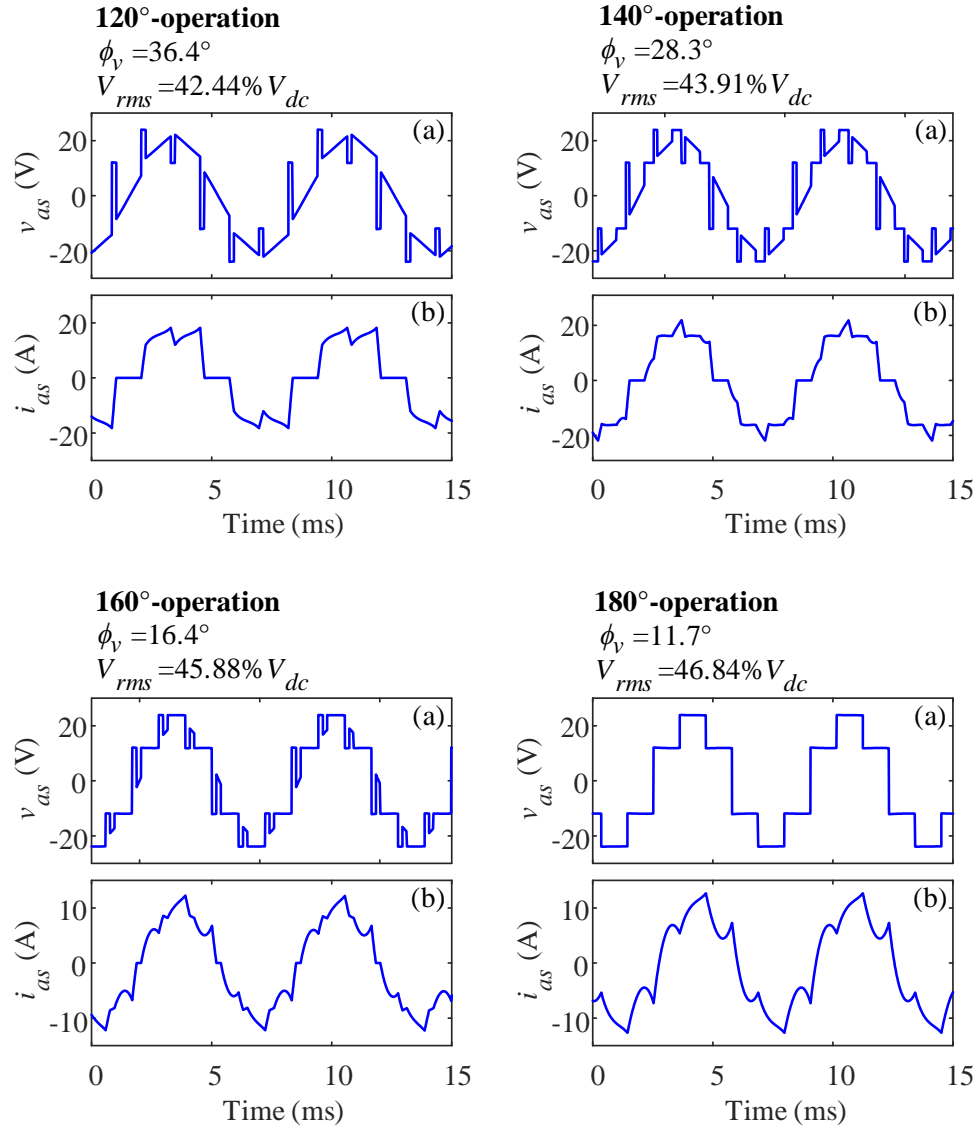
Figure 4.2 Typical steady-state waveforms obtained from simulations with 120-degree, 140-degree, 160-degree, and 180-degree operation under similar dc bus voltage for: (a) phase voltage, and (b) phase current.

Therein, the waveforms of the 120-degree and 180-degree operation are consistent with the typical waveforms shown in the literature, e.g. [10]. It can also be noticed in Figure 4.2, that the duration of time when the phase current is discontinuous and stays at zero is largest for the 120-degree operation. The discontinuity interval becomes smaller with increasing the conduction angle D_{con}, and completely disappears for the 180-degree operation (becomes continuous).

At the same time, increasing the conduction angle D_{con} also prolongs the time when the phase terminals are connected to the dc bus, which also increases the RMS value of the phase voltage seen by the motor (for a considered value of $\bar{v}_{dc}$). This has also been reported in [51] with a study regarding the phase voltage with 120-degree, 150-degree, 160-degree and 180-degree operations. Therefore, an extension of the voltage control may be readily implemented/achieved by adjusting the conduction angle D_{con}.

4.2   Implementation of Extended MTPA in DSP

To maintain the optimal properties of MTPA over the operations with the extended commutation methods, the d-axis current which does not contribute to the electromagnetic torque (assuming a round machine) is to be kept at zero for alignment between the phase current and the back EMF according to section 3.2.2. However, depending on the conduction angle and motor parameters, the (averaged) d-axis current may be different from 0 without proper adjustment of the firing angle, as shown in Figures 4.3–4.4. The corresponding phasor diagrams are also shown in Figure 4.5(a)–(b), where it can be observed that a positive d-axis current results in phase current lagging the back EMF, while a negative d-axis current results in phase current leading the back EMF, respectively. This misalignment results in a suboptimal operation. In Figure 4.5(c), the phase

current and back EMF are aligned, which is achieved by adjusting the *d*-axis current to zero which results in the MTPA operation. To achieve this optimal operation, the advance in firing angle needs to be compensated as (2.24).
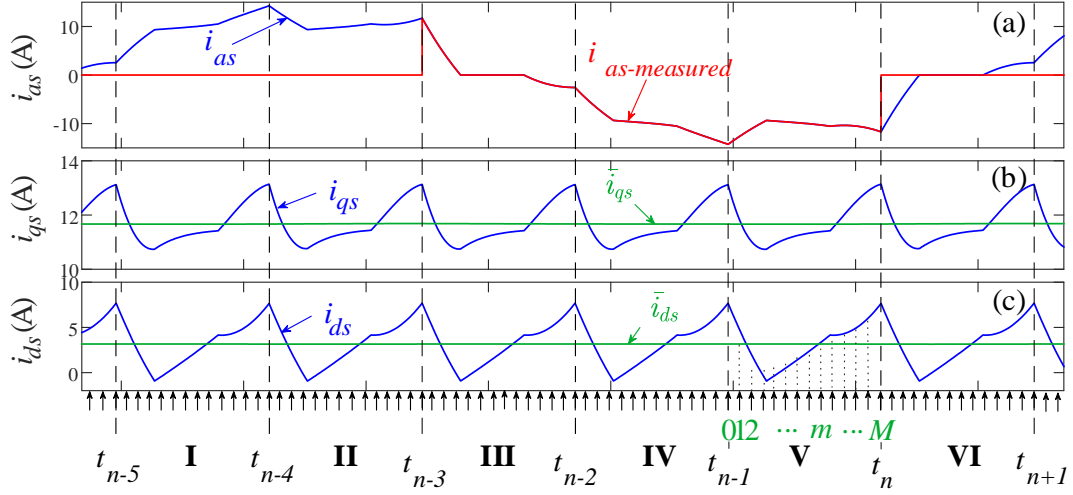
Figure 4.3 Steady-state current waveforms of the 140-degree operation with 20-degree advance in firing angle: (a) phase current, (b) *q*-axis current, and (c) *d*-axis current.
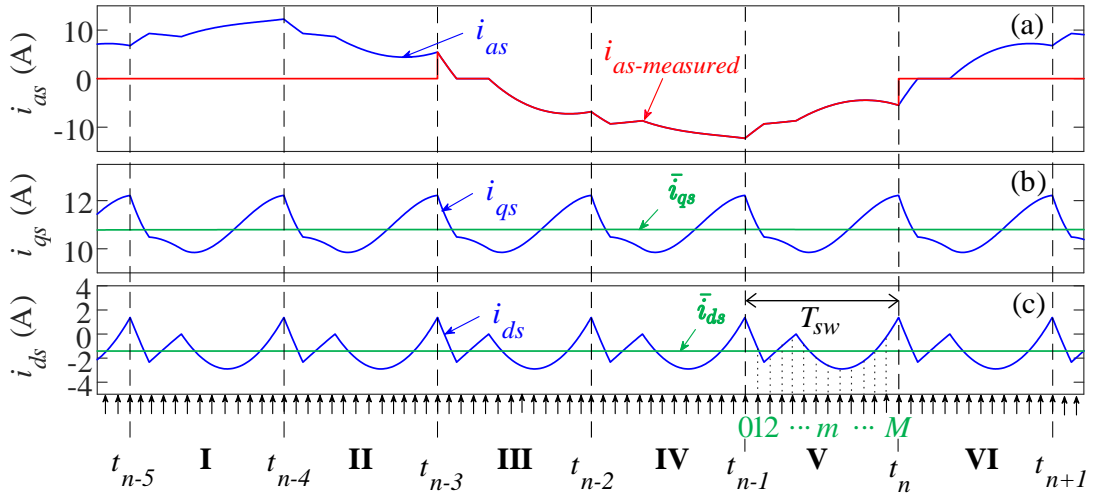
Figure 4.4 Steady-state current waveforms of the 160-degree operation with 20-degree advance in firing angle: (a) phase current, (b) *q*-axis current, and (c) *d*-axis current.
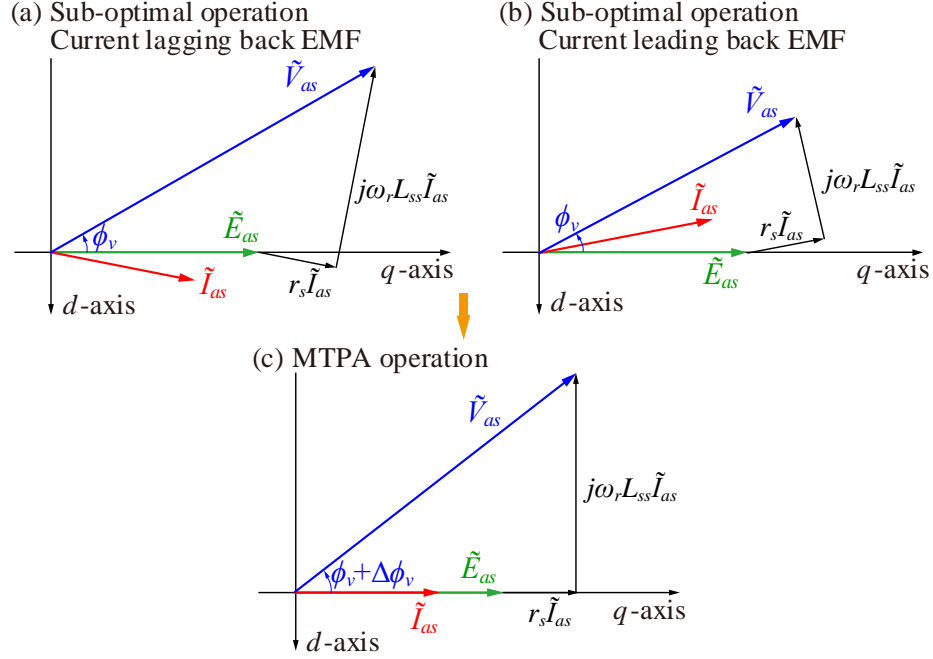
Figure 4.5 Phasor diagram of voltage, back EMF, and current under (a) suboptimal operation with the current lagging back EMF, (b) suboptimal operation with the current leading back EMF, and (c) optimal MTPA operation with the current aligned (in-phase) with back EMF.

The compensation method based on a PI controller in section 3.2.2 is extended to incorporate with the extended conduction logics in a DSP. In DSP implementation, to eliminate the current ripple for better control of zero d-axis current, the averaging in (3.1) may be discretized by using a simple summation based on the fast sampling inside the switching (as indicated by interval V in Figures 4.3–4.4) as

$$\bar{i}_{ds} = \frac{1}{M} \sum_1^M i_{ds}(m). \tag{4.4}$$

This value is updated at the end of switching interval. With respect to Figures 4.3–4.4, the value of $\bar{i}_{ds}(t_n)$ calculated by (4.4) becomes available at the end of switching interval t_n.

Additionally, since the averaging in (4.4) is only over 1/6 of an electrical cycle, there is no need for measuring the entire current waveform, and this method lends itself to a computationally efficient implementation in a DSP. Moreover, since generally sensing the entire phase current is expensive, the proposed approach may be readily implemented by measuring the currents of only the lower-side transistors of the VSI. As an example, such measurement is depicted in Figure 4.3(a) and Figure 4.4(a) (see red line $i_{as-measured}$ on top of current i_{as}). It is observed that this measurement is available in each phase when its lower transistor or diode are conducting. This may be done by measuring the voltage across very small resistors that are connected in series with the lower-side transistors [69].

Without loss of generality, the switching interval V is taken to depict this. Within this interval, both measured currents i_{as} and i_{bs} are available from the low-side current sensors. Assuming a star-connected winding, the phase c current can be calculated as

$$i_{cs} = -i_{as} - i_{bs} . \tag{4.5}$$

This allows obtaining all three currents in $\mathbf{i}_{abcs}$, from which the transformed current $\mathbf{i}_{qds}$ is calculated using (2.8). Then, the d-axis current i_{ds} is obtained. Thereafter, it becomes possible to implement a simple PI controller that regulates the value of $\overline{i}_{ds}$ to zero. The corresponding controller is shown in Figure 3.6.

Also, the DSP implementation of this controller is shown in Figure 4.6. In this thesis, the hardware interruption is assumed to be triggered with a frequency of 15 kHz (i.e., the hardware sampling interval $T_I = 66.67 \mu s$). At the beginning of each interruption, the Hall sensor signals are executed and the Hall state h_s is calculated based on (2.16). The corresponding estimated speed is
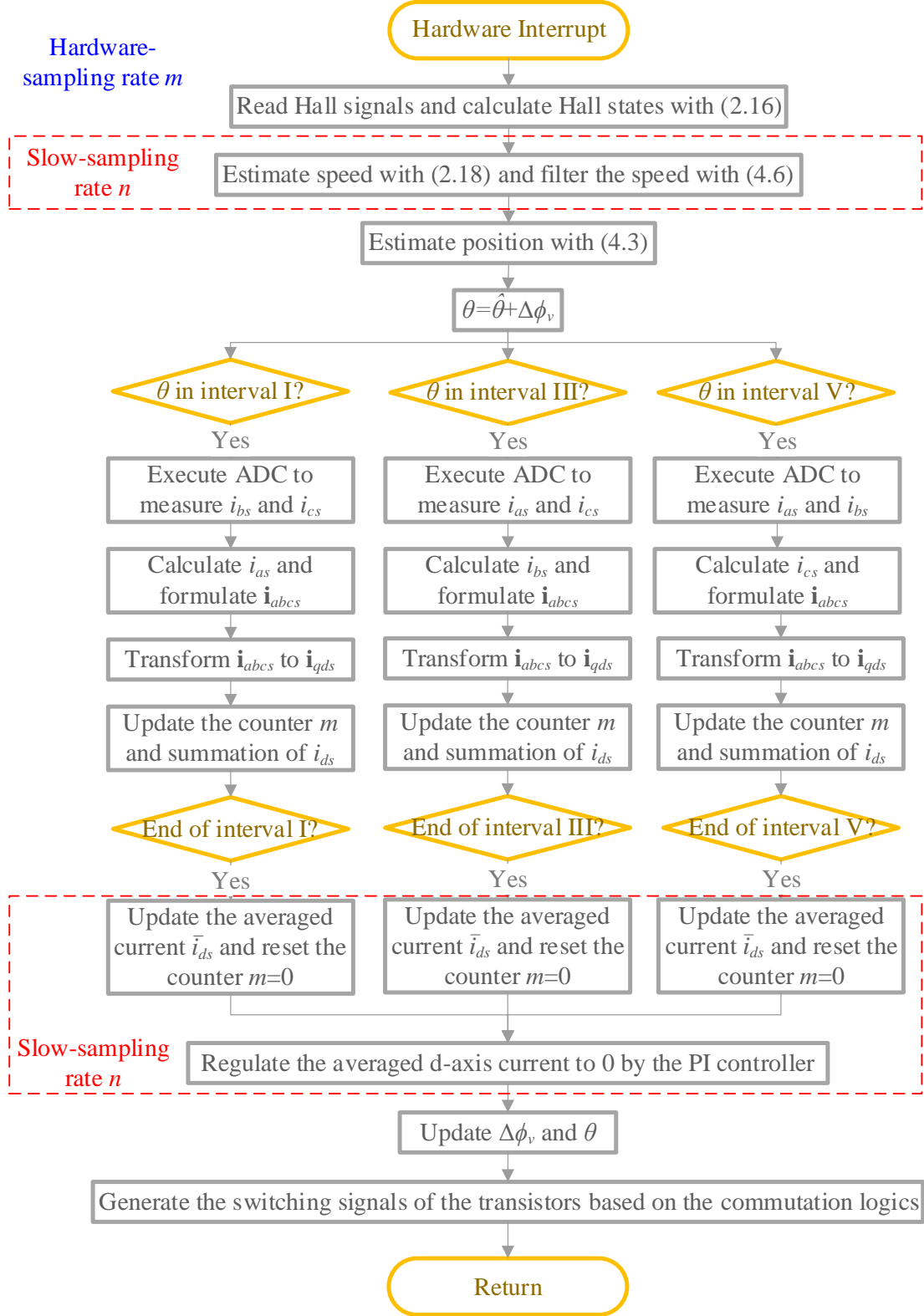
Figure 4.6 Logical flow-chart of the DSP implementation for the proposed control scheme.

calculated using (2.18).

To eliminate possible error caused by the unbalanced or misaligned Hall-sensors, the estimated speed is filtered with a six-step averaging [4] as

$$\bar{\hat{\omega}}_r(t_n) = \frac{1}{6} \sum_{p=0}^{5} \hat{\omega}_r(t_{n-p}) \, . \tag{4.6}$$

Then the position is estimated from the averaged estimated speed $\bar{\hat{\omega}}_r(t_n)$ using (4.3). With this position and the previous compensation of firing angle (the initial value is set at zero), it becomes possible to determine the position related to the switching intervals (numbered as I–VI in Figure 2.2). For switching intervals I, III and V, the counter starts from zero at the beginning of the interval, while the three-phase current vector is formulated by executing the analog-to-digital converter (ADC) corresponding to the two of the effective current measurements and the currents in qd-coordinates are calculated using (2.8). At the end of each interval, the averaged d-axis current is updated according to (4.4) for the PI controller to compensate the advance in firing angle. Here, the d-axis current averaging and the PI controller are operated with a slow sampling rate n instead of the fast hardware sampling. At the end, based on the estimated position and the updated compensation of firing angle, the switching signals for the six inverter transistors is generated according to the commutation logic.

4.3   Computer Studies

The proposed control scheme for extended commutation angle has been verified with steady-state and transient computer studies. The system depicted in Figure 2.1 has been implemented in MATLAB/Simulink in full details with the subject BLDC motor drive (with parameters listed in Appendix A.1). The parameters of the controller (i.e., the PI controller in the proposed MTPA

strategy) are listed in Appendix B.3. Additionally, the mechanical load torque is assumed to be quadratic with respect to the rotor speed, defined as $T_m = K_{m2}\omega_r^2$ (listed in Appendix C.2).

First, the proposed voltage control is demonstrated by gradually increasing the phase voltage over its adjustable range. Specifically, the study first increases the PWM duty cycle d_{pwm} from 0.25 to 1 within the 2 to 4 s, while keeping the conduction angle $D_{con} = 120°$. Then, between 4 to 6 s, the conduction angle D_{con} is linearly increased from 120 to 180 degrees, while keeping the PWM duty cycle maxed out, i.e., $d_{pwm} = 1$. The corresponding results are shown in Figure 4.7, with a detailed view of some variables at around $t = 4$ s also shown in Figure 4.8.

Since the increase in input voltage is relatively slow, the obtained results may be assumed in quasi steady-state. As it can be observed in Figures 4.7–4.8, the RMS phase voltage, RMS phase current, motor speed, and averaged electromagnetic torque all demonstrate increasing trends with the increasing of the PWM duty cycle d_{pwm} and also increasing of conduction angle D_{con}. It is also noted that the increase in phase voltage stops for conduction angle between 167.5 and 180 degrees. This is because the BLDC motor considered in this paper has a large inductance, which results in a long commutation angle [10]. Specifically, after D_{con} reaches 167.5 degrees, the phase current becomes continuous, and the voltage waveform becomes identical to that of the 180-degree operation. It is also observed that the RMS phase voltage is increased from 15.3V (maximum possible with 120-degree operation at $d_{pwm} = 1$) to 16.9V (maximum possible with 180-degree operation at $d_{pwm} = 1$).
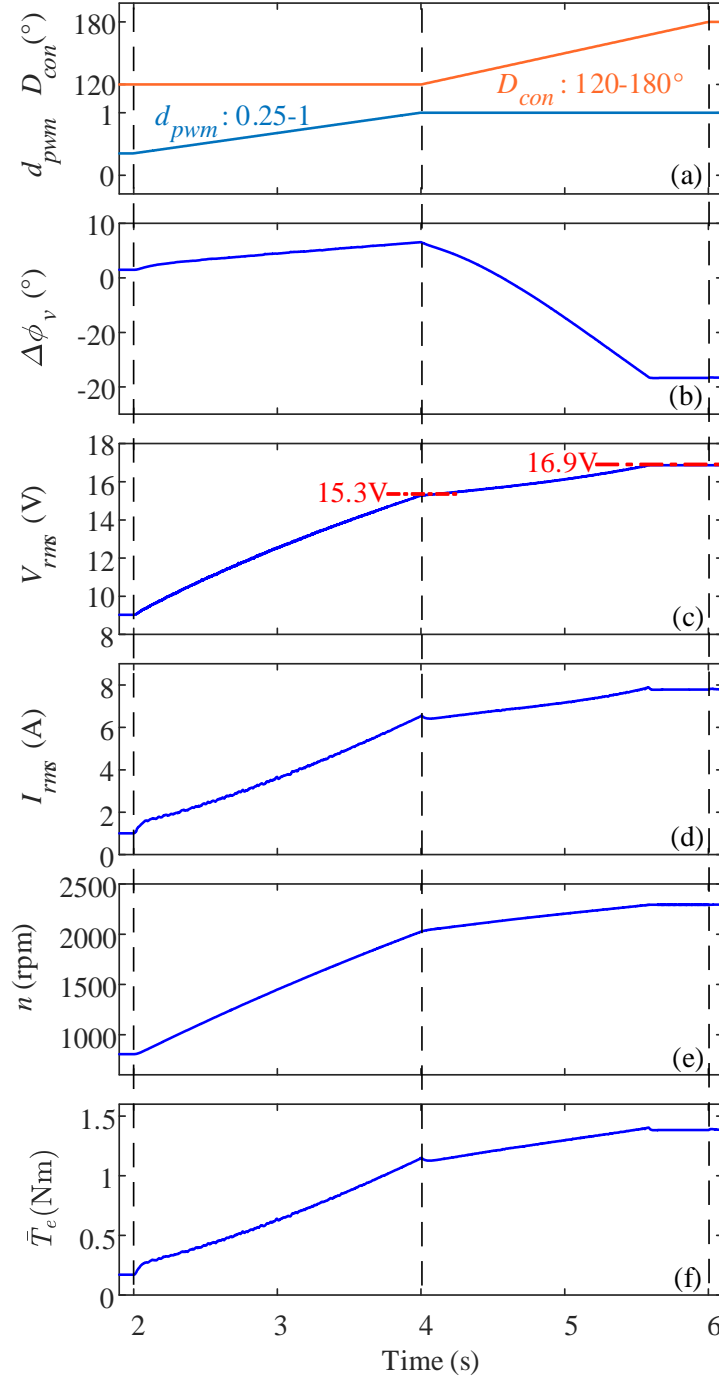
Figure 4.7 The profile of several variables when gradually increasing PWM duty cycle and conduction period: (a) duty cycle and conduction period, (b) firing angle compensation, (c) RMS of phase voltage, (d) RMS of phase current, (e) mechanical speed, and (f) average electromagnetic torque.
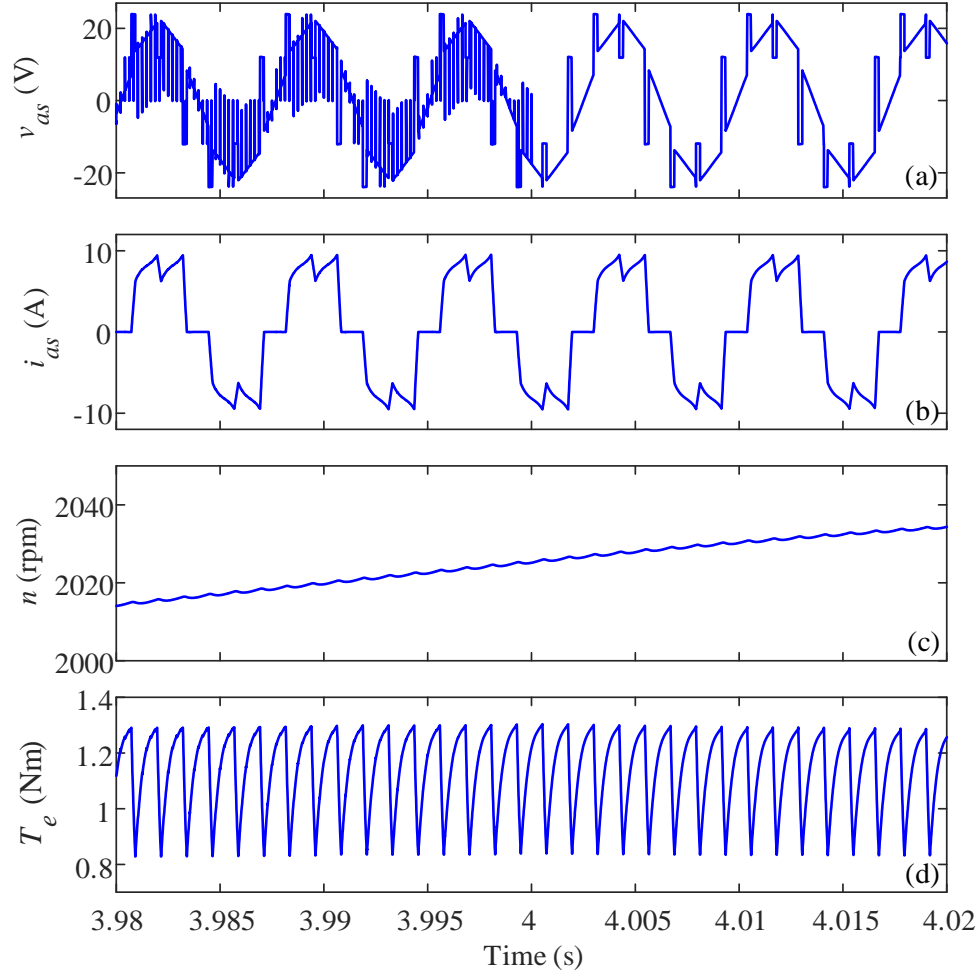
Figure 4.8 Magnified view of the corresponding variables in Figure 4.7 at around t=4s for the: (a) phase voltage, (b) phase current, (c) mechanical speed, and (d) electromagnetic torque.

Next, the proposed voltage extension method is compared in steady state with the conventional control for driving the same mechanical load (at the same torque and speed). To obtain the same electromagnetic torque under different duty cycles and conduction periods, the dc voltage has to be adjusted accordingly. The first operating point is defined by $n = 2000 \text{rpm}$ and $\bar{T}_e = 0.9 \text{Nm}$.

Table 4.1 Simulated steady-state performance of different commutation methods at 2000 rpm and 0.9 Nm achieved by adjusting dc voltage

65

Control Variables			V_{dc} (V)	V_{as-RMS} (V)	THD (v_{as}) (%)	$T_{e-ripple}$ (%)
	d_{pwm}	D_{con}				
Conventional Method	0.70	120⁰	49.03	17.42	80.02	53.11
	0.85		40.42	15.82	59.39	46.96
	1.00		34.36	14.58	38.56	42.20
Proposed Extended Method	1.00	140⁰	32.40	14.19	29.61	25.61
		160⁰	30.97	14.17	29.08	31.23
		180⁰	30.38	14.25	31.24	30.15

The resulting RMS of phase voltage, total harmonic distortion (THD) of phase voltage, and torque ripple are summarized in Table 4.1. Here, the torque ripple is calculated as follows:

$$T_{e-ripple} = \left(\left[\max\left(T_e\right) - \min\left(T_e\right) \right] / \overline{T}_e \right) \times 100\% . \tag{4.7}$$

The first three rows in Table 4.1 (shaded in blue) correspond to the conventional 120-degree operation with duty cycle control. It is interesting to observe that with the increase of the duty cycle from 0.7 to 1, the phase voltage RMS, the voltage THD, and torque ripple values are decreasing; because V_{dc} should be decreased to ensure the same operating point. The best utilization of dc voltage ($V_{dc} = 34.36\text{V}$) is achieved with $d_{pwm} = 1$ (i.e., 14.58/34.36=42.4%) compared to when the duty cycle is 0.85 and 0.70 (i.e., 15.82/40.42=39.1% and 17.42/49.03=35.5%, respectively). Moreover, having $d_{pwm} = 1$ results in voltage THD of 38.56% and torque ripple of 42.20%; respectively, which are both lower compared to when having the d_{pwm} equal to 0.85 or 0.7. Extending the conduction period D_{con} from 120 to 180 degrees brings further reduction of the voltage THD (below 32%) and torque ripple (below 32%), as can be

observed in the last four rows of the orange-shaded part of Table 4.1. As can be expected, using the proposed method the best dc voltage utilization is achieved with $D_{con} = 180°$ (i.e., 46.91% with $V_{dc} = 30.38\text{V}$).

A transient study is also considered to demonstrate the performance of the proposed MTPA tracking method under changing conditions. First, it is assumed that the BLDC motor/inverter is supplied from the nominal dc source (36 volts), and operates under the 120-degree conduction with PWM duty cycle at 0.9. Then, at $t = 2.002\text{s}$, the conduction angle is stepped to 140-degree with duty cycle maxed out at 1. The corresponding simulated transient responses of several variables are shown in Figure 4.9. Since the effective value of the stator voltage has increased, the motor undergoes an acceleration transient. The performance of the PI controller is shown in Figure 4.9(a), where the compensation angle is automatically adjusted to achieve the MTPA operation which is reached in the new steady state around $t = 2.1\text{s}$.
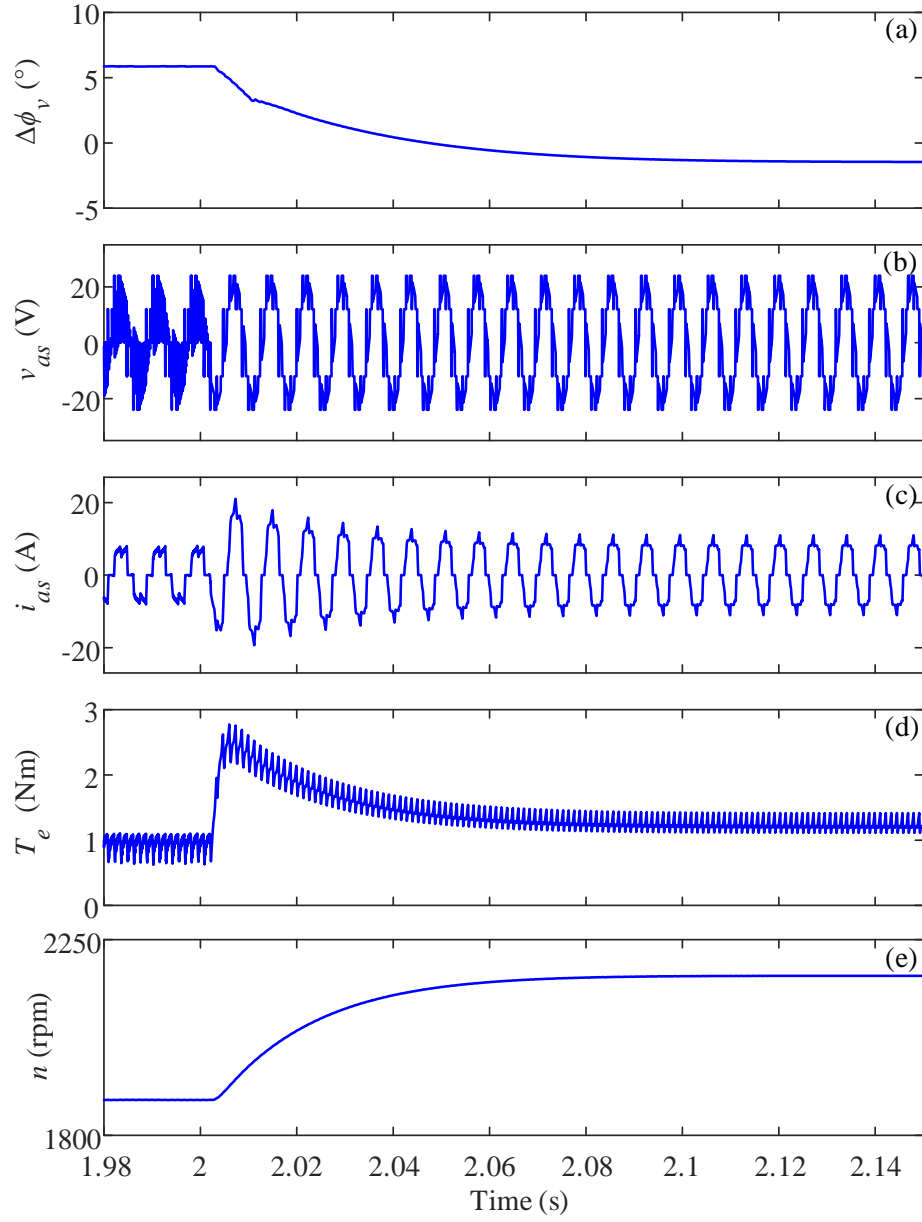
Figure 4.9 Transient response of several variables to step from 120-degree operation with PWM duty cycle of 0.9 to an extended 140-degree operation without PWM at 2.002 s: (a) firing angle compensation, (b) phase voltage, (c) phase current, (d) electromagnetic torque, and (e) mechanical speed.

4.4 Experimental Verification

A hardware prototype as shown in Figure 1.1 has been set up for verification of the proposed extended operation. For the motors (Model 86EMB3S98F, Model EC 167131 and Model

JK80BLS02) with parameters in Appendix A.1–3, the PI controller is tuned with parameters listed in Appendix B.3. Also, a mechanical torque is emulated on the load shaft by coupling the motor-drive system with a dc dynamometer. When the load resistance of the dynamometer is fixed, the speed-dependent mechanical torque could be approximately described by $T_m = K_{m3}\omega_r + K_{m4}$ in the steady state (with detailed derivations provided in Appendix C.3).

Firstly, the detailed studies are conducted for the motor Model 86EMB3S98F which has been primarily verified in the simulation. To demonstrate the motor drive operation around the nominal operating point with $n = 2000\text{rpm}$ and $\bar{T}_e = 0.9\text{Nm}$, the steady-state voltage and current waveforms with different commutation methods under different dc voltage supplies have been measured as demonstrated in Figure 4.10. The results shown in Figure 4.10 are consistent with the simulated waveforms in Figure 4.2, which also verifies the DSP implementation of the generalized commutation logic.

To demonstrate the operation of the proposed extended method over a wide range of operating conditions, the motor drive is supplied from the fixed dc source ($V_{dc} = 36\text{V}$) and the dc dynamometer is connected with a fixed resistance (i.e., $T_m = K_{m3}\omega_r + K_{m4}$). Initially, the system operates under the 120-degree switching logic, and the voltage control is applied by slowly increasing the duty cycle from 0.25 to 1. After reaching the maximum PWM duty cycle (i.e., $d_{pwm} = 1$), the conduction angle D_{con} is slowly increased from 120 to 180 degrees. The corresponding experimental measurements are shown in Figure 4.11. As it is observed in Figure
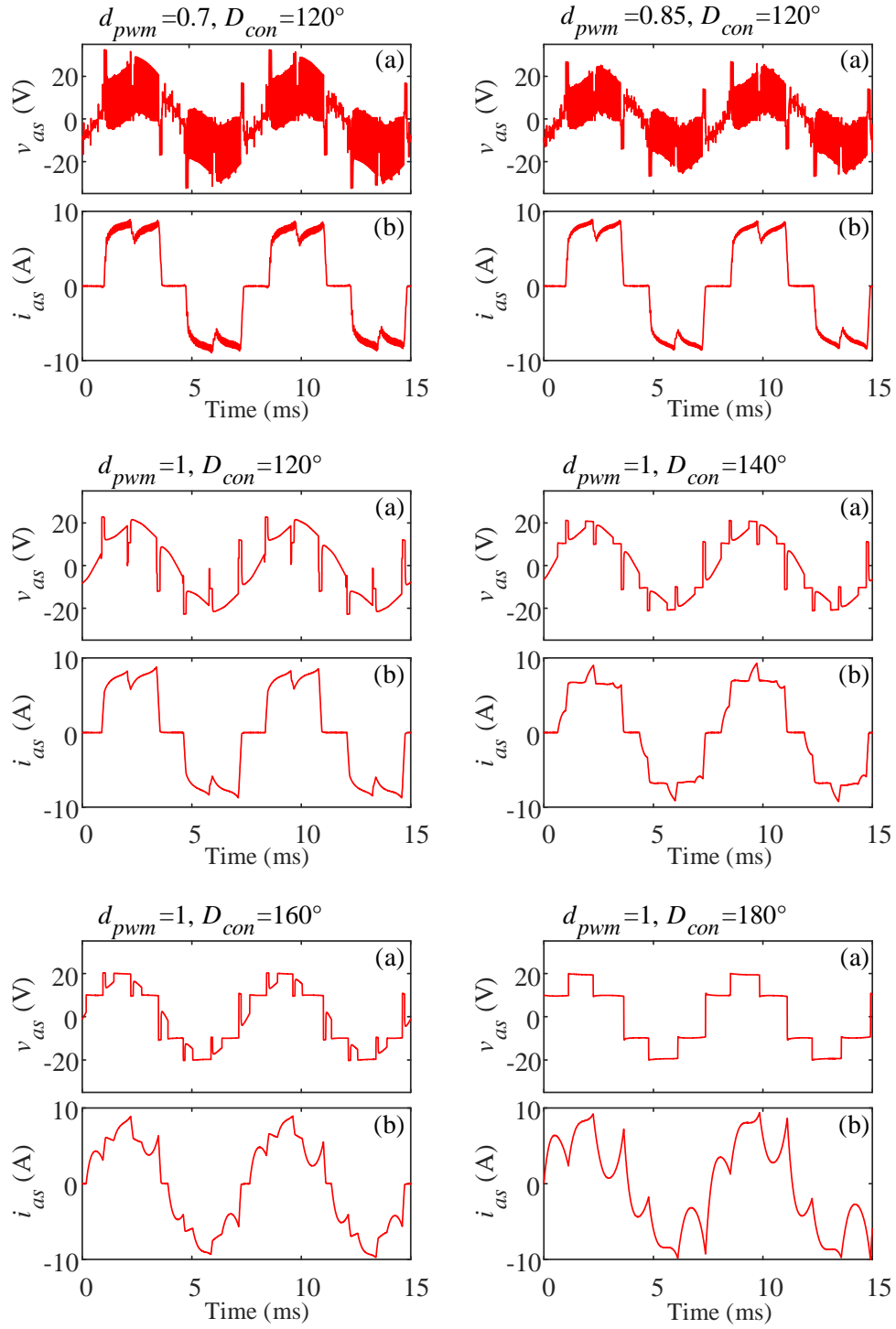
Figure 4.10 Measured steady-state waveforms obtained with different conduction angles: (a) phase voltage, and (b) phase current.
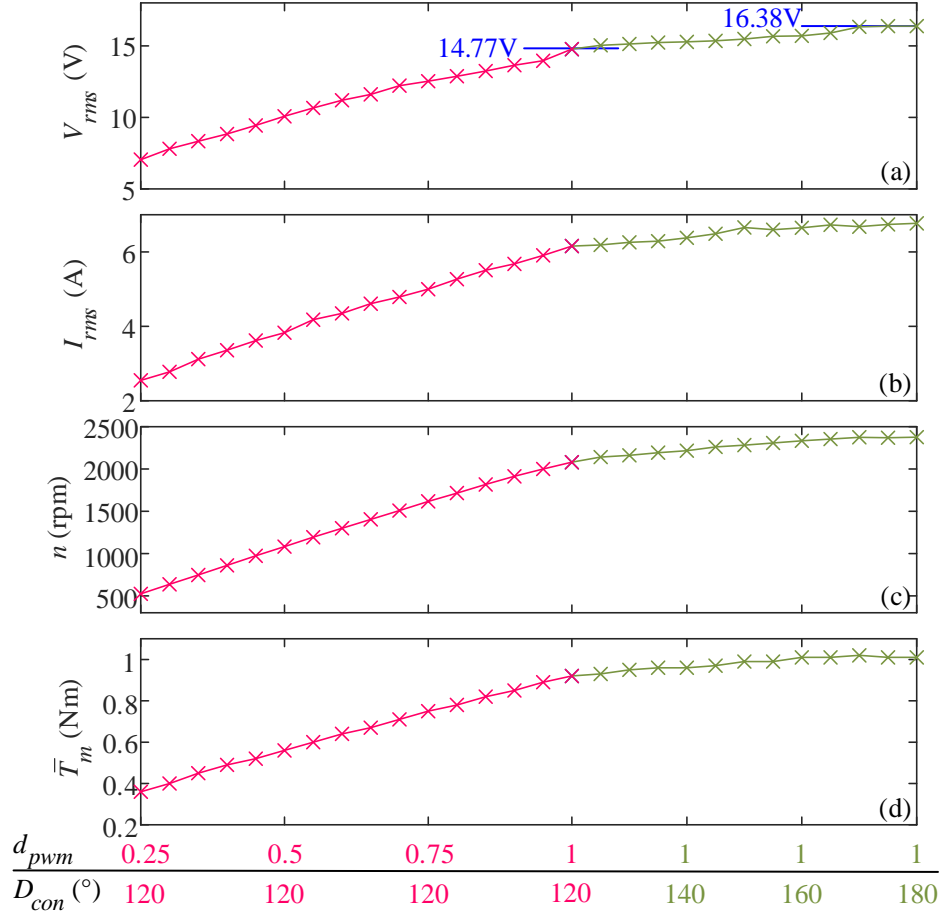
Figure 4.11 Measured steady-state profile of several variables with different commutation logics when the mechanical load is linearly proportional to the rotor speed: (a) RMS phase voltage, (b) RMS phase current, (c) mechanical speed, and (d) average mechanical torque.

4.11, the phase voltage, phase current, mechanical speed, and dynamometer-measured torque all consistently increase in the conventional region as well as in the extended region (distinguished by colors red and green, respectively). It is interesting to note that the extreme point for the conventional region (defined by $D_{con} = 120°$ and $d_{pwm} = 1$) is reached at 2081 rpm and 0.92 Nm, while the proposed extended commutation angle method allows to further continuously increase the speed and torque to 2377 rpm and 1.01 Nm, respectively, in the extended region (extreme of

which is defined by $D_{con} = 180°$ and $d_{pwm} = 1$). These points also correspond to the increase of RMS phase voltage from 14.77 V to 16.38 V, which constitutes about 11% increase.

Therefore, it is possible to define a modified duty cycle d'_{pwm} that is ranging from 0 to d'_{max} (here, $d'_{max} = 1.11$) that spans the entire range of operating voltages. This modified duty cycle d'_{pwm} in turn determines the actual d_{pwm} as

$$d_{pwm} = \begin{cases} d'_{pwm}, & 0 < d'_{pwm} < 1 \\ 1, & 1 \le d'_{pwm} < d'_{max} \end{cases}.$$ (4.8)

Also, due to the approximately linear profiles as seen in Figure 4.11, the delay angle α_d (4.1) in the switching logic can be calculated as

$$\alpha_d = \begin{cases} 60°, & 0 < d'_{pwm} < 1 \\ \dfrac{60°\left(d'_{max} - d'_{pwm}\right)}{\left(d'_{max} - 1\right)}, & 1 \le d'_{pwm} < d'_{max} \end{cases}.$$ (4.9)

Next, to compare the proposed control scheme against the conventional method, the same torque-speed operating point (i.e., $n = 2000$rpm and $\overline{T}_e = 0.9$Nm) is achieved for different values of conduction angle D_{con} and PWM duty cycle d_{pwm} by adjusting the dc-link voltage in the experimental setup. The corresponding results are summarized in Table 4.2. Here, the torque ripple is not included due to the limitation of the dynamometer, which only measures the average torque. Regarding the RMS and THD values of the ac phase voltage, consistent results as in Table 4.1 (with simulations) are observed in Table 4.2 (with experiments). As seen in Table 4.2, compared to the conventional 120-degree operation (red rows), the extended method (green rows) reduces the RMS and THD of the ac phase voltage that is required to support the same mechanical load, which is consistent with simulation results in Table 4.1.

Table 4.2 Measured steady-state performance of different commutation methods at 2000 rpm and 0.9 Nm achieved by adjusting dc voltage

Control Variables			V_{dc} (V)	V_{as-RMS} (V)	THD (v_{as}) (%)
	d_{pwm}	D_{con}			
Conventional Method	0.70		49.0	16.48	80.65
	0.85	120⁰	40.4	15.03	59.65
	1.00		34.4	14.15	43.70
Proposed Extended Method		140⁰	32.4	13.73	31.79
	1.00	160⁰	31.0	13.56	27.97
		180⁰	30.4	13.77	31.60

Additionally, the transient performance of the proposed method is also validated here experimentally. The same speed-dependent mechanical load (emulated by the dc dynamometer with fixed resistive load) is used in this test. Initially, the BLDC motor is operating using standard 120-degree switching logic with PWM duty cycle at 0.9. This operating condition is shown in Figure 4.12 as Operating Point A. Then, the effective voltage is stepped up by increasing the duty cycle to 1 and conduction angle to 140 degrees. After a short transient, the machine reaches a new steady-state Operating Point B. The corresponding measured responses are shown in Figure 4.12. Specifically, the responses of phase voltage and current Figures 4.12(a) and (b) very closely match the simulated results of Figure 4.9, which validates the model. The overall acceleration transients in Figure 4.9 and 4.12 are also very similar and confirm the proper operation of the proposed method.
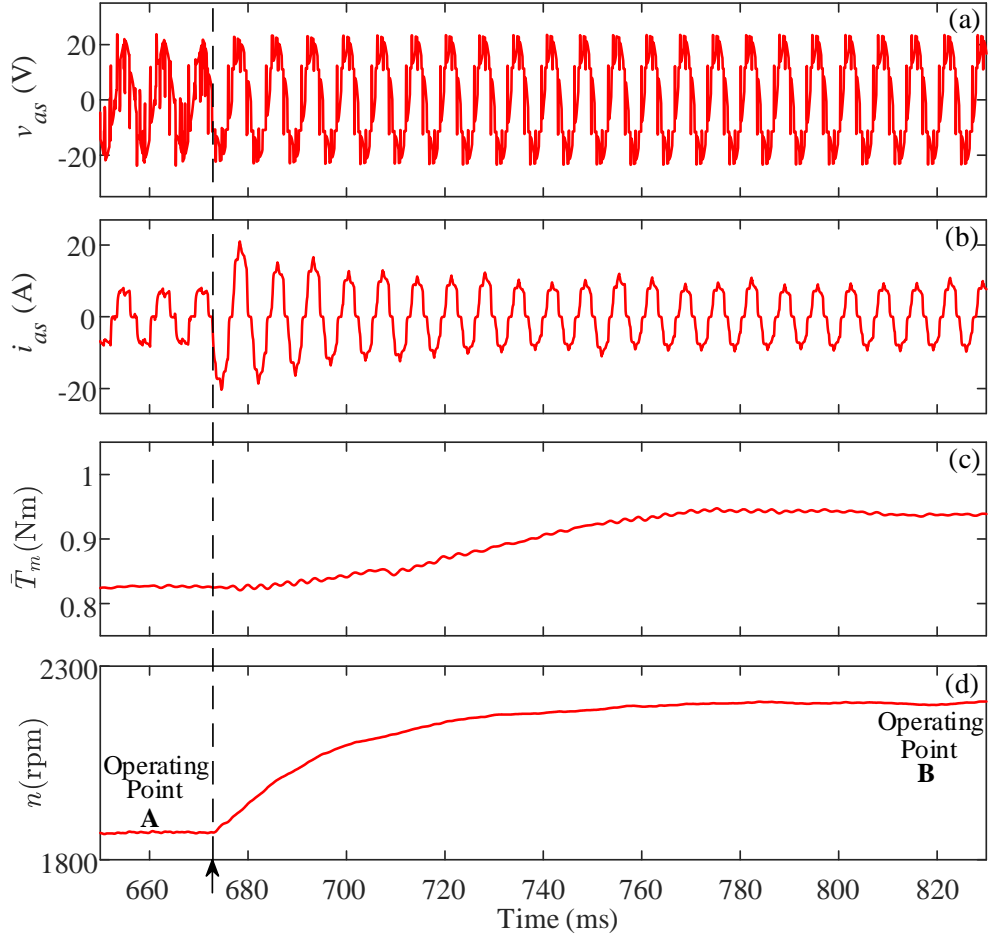
Figure 4.12 Transient response of several variables to stepping from 120-degree operation with PWM duty cycle at 0.9 into 140-degree operation without PWM obtained from experimental measurements for: (a) phase voltage, (b) phase current, (c) mechanical torque, and (d) mechanical speed.

The MTPA operation is further verified for Operating Points A and B. For this purpose, the measured Hall signal and phase a current are shown in Figure 4.13. Based on the recorded Hall signal h_1 in Figure 4.13(a), the corresponding back EMF is also reconstructed and plotted in Figure 4.13(b). As it is observed in Figure 4.13(c), the fundamental component of the actual current is in phase with its corresponding phase back EMF for both Operating Points A and B, which verifies the optimal property of the MTPA operation is retained by the proposed control method.

Figure 4.13 Steady state waveforms of motor Model 86EMB3S98F at the operating points A and B with MTPA obtained from experimental measurements for: (a) recorded Hall signal, (b) reproduced corresponding back EMF, and (c) measured phase current and its fundamental frequency component.

To further verify the applicability of the proposed methods for machines with different parameters, the studies are carried out to check the effectiveness for both the conventional and extended operating range with the other two machine models. To be consistent with previous study, the steady state waveforms for Point A operating in 120-degree mode with PWM duty cycle at 0.9 and Point B operating with 140-degree operation and no PWM are obtained as Figures 4.14 and 4.15 for motor Model EC 167131 and motor Model JK80BLS02, respectively. The fundamental component of the actual current is in phase with its corresponding reconstructed phase back EMF for both Operating Point A and B regardless the machine parameters. It is verified the

75

proposed MTPA method is effective for machines with small inductance (e.g., Model EC 167131) and large inductance (e.g., Model JK80BLS02) for both the conventional and extended operation regions.
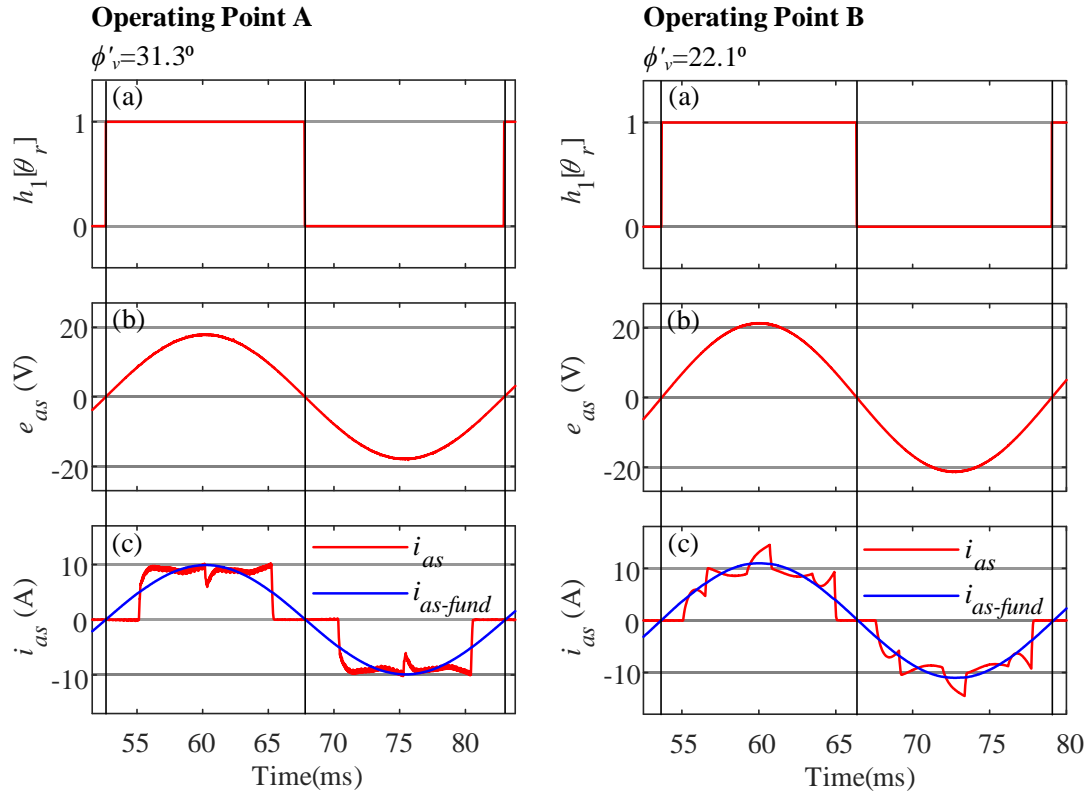
Figure 4.14 Steady state waveforms of motor Model EC 167131 at the operating points A and B with MTPA obtained from experimental measurements for: (a) recorded Hall signal, (b) reproduced corresponding back EMF, and (c) measured phase current and its fundamental frequency component.

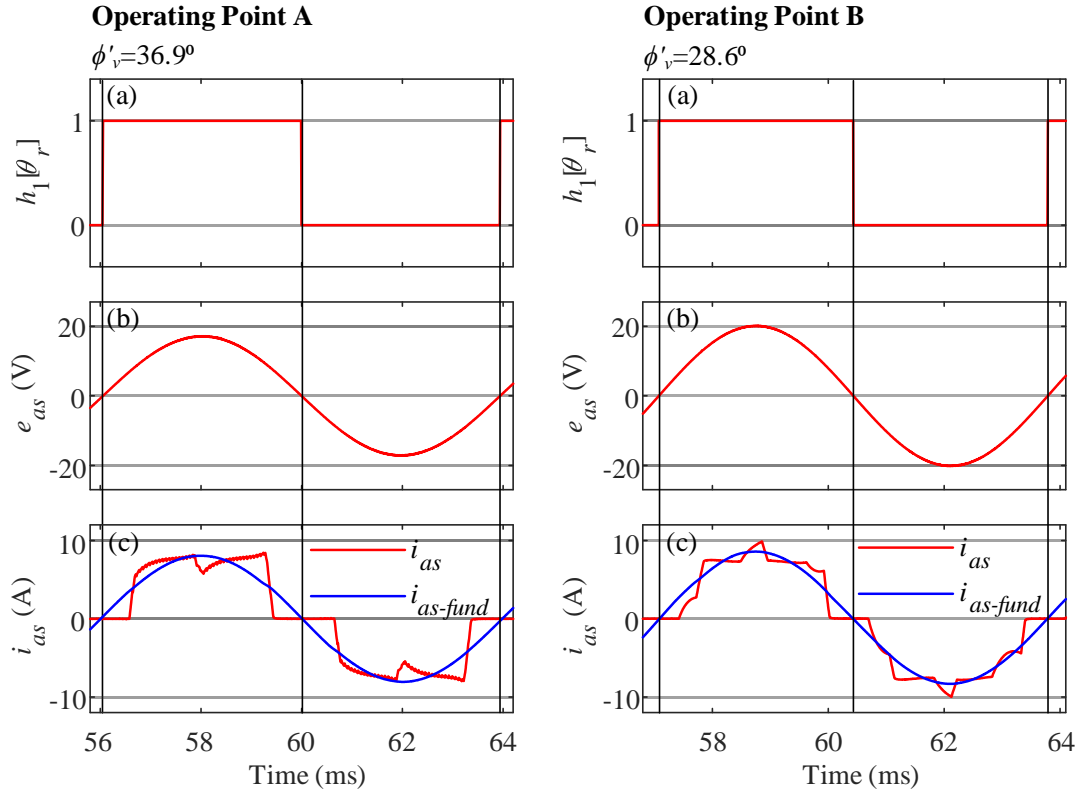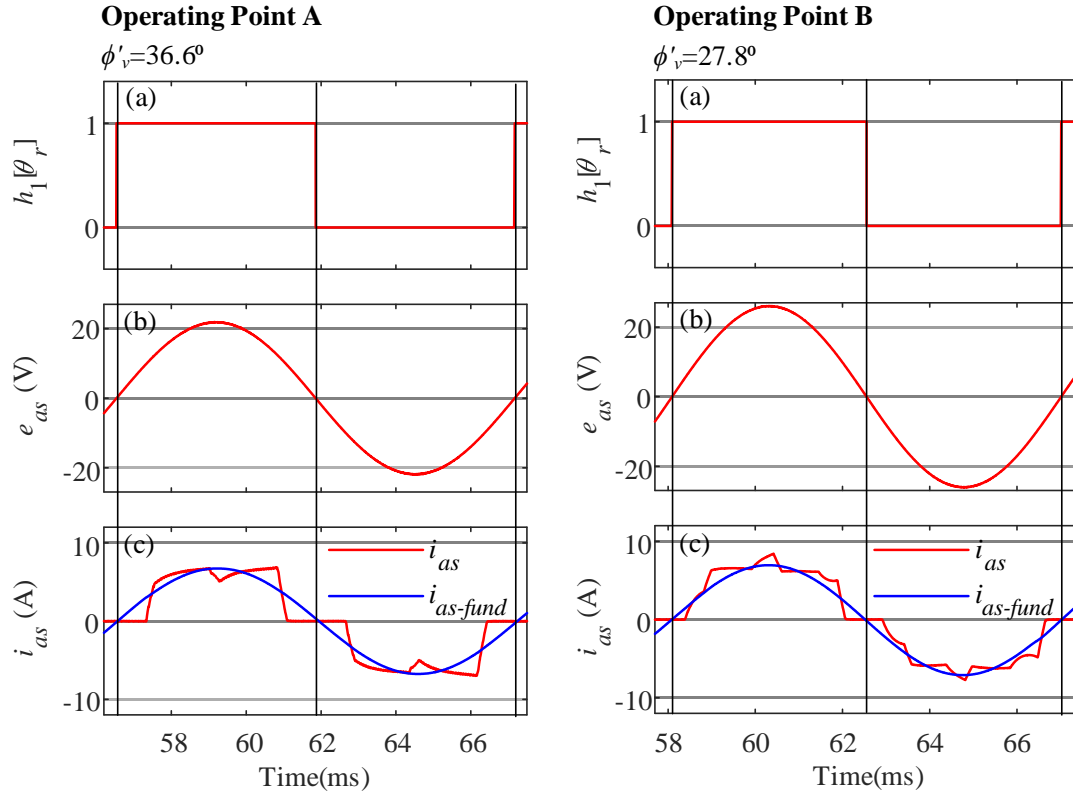**Figure 4.15 Steady state waveforms of motor Model JK80BLS02 at the operating points A and B with MTPA obtained from experimental measurements for: (a) recorded Hall signal, (b) reproduced corresponding back EMF, and (c) measured phase current and its fundamental frequency component.**

Finally, to demonstrate the overall achieved benefit of the proposed extended conduction angle method, the steady-state torque-speed characteristics obtained with the conventional and the proposed control schemes have been obtained from both the detailed simulations and the experimental setup; the results of which are superimposed and shown in Figure 4.16. As seen in Figure 4.16, the simulated characteristics are very consistent with the measured results, which confirms the accuracy of the detailed model. The general trend of the torque-speed characteristic is as expected for the BLDC motors of this type when supplied from a constant dc source, with close-to-linearly decrease in speed with increasing torque. The characteristic is shifted upwards by either increasing the PWM duty cycle in the conventional region (see Figure 4.14, white area) or

by increasing the conduction angle in the extended region (see Figure 4.14, green area, which is achieved by the proposed extended angle method).

(I)	120° commutation (d_{pwm}=0.6)	(V)	120° commutation (d_{pwm}=1)
(II)	120° commutation (d_{pwm}=0.7)	(IV)	140° commutation (d_{pwm}=1)
(III)	120° commutation (d_{pwm}=0.8)	(VII)	160° commutation (d_{pwm}=1)
(IV)	120° commutation (d_{pwm}=0.9)	(VIII)	180° commutation (d_{pwm}=1)

Simulated Results ———   **Experimental Results** ✕
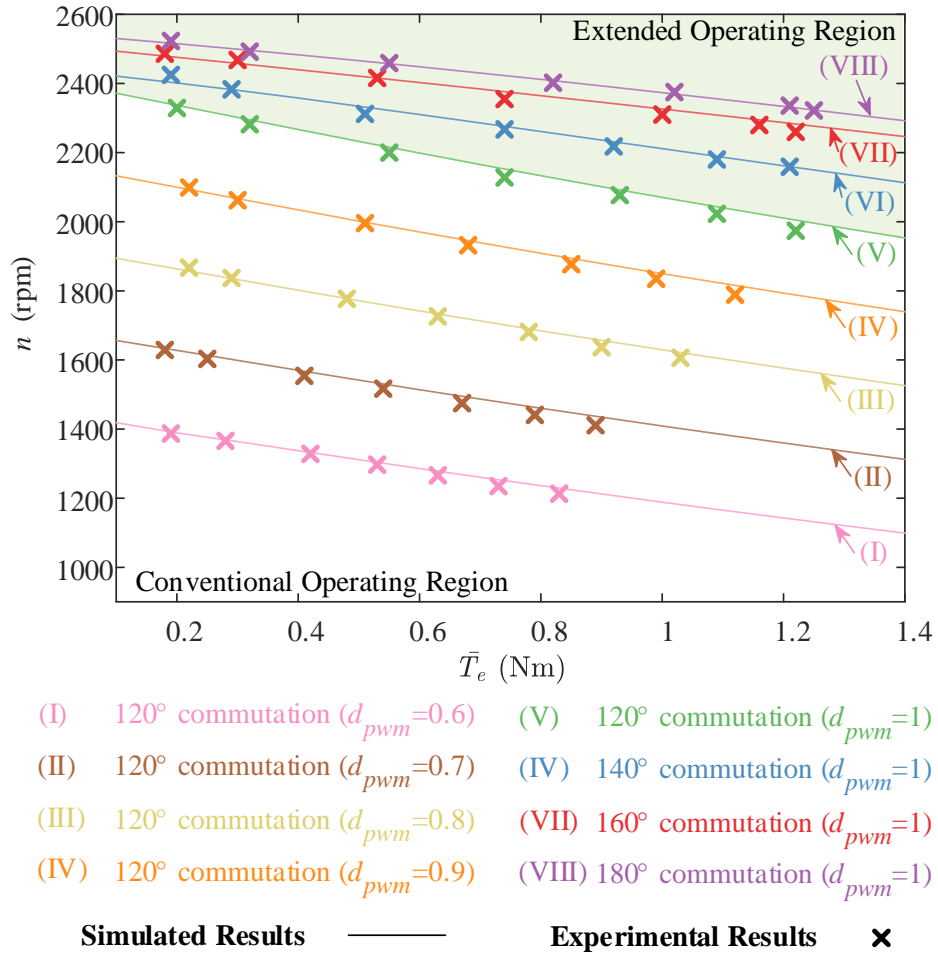
Figure 4.16 Measured and simulated steady-state torque-speed characteristics of the BLDC motor achieved by the conventional 120-degree and the proposed extended conduction angle methods.

Chapter 5: Conclusion

5.1   Contributions and Anticipated Impact

The research presented in this thesis has been focused on the MTPA and MTPV strategies of the Hall-sensor-controlled BLDC motor drive systems. With the optimal properties, the MTPA and MTPV are widely applied control methods aiming at maximum torque for a given phase current or a given dc voltage, respectively. For BLDC motors operating with different conduction logics, the applicable MTPA and MTPV strategies are different. In 180-degree operation, it is possible to derive simple firing angle equations with the well-known six-step voltage waveforms. However, the operations with 120-degree or the extended conduction logic include the operating-point-dependent commutation processes and make it difficult to calculate the firing angle analytically in the form of explicit equations. Instead, numerical approximations coupled with tunable controllers (e.g., with a PI controller) are often considered for regulating the current. In this thesis, novel control schemes have been proposed that are shown to perform better than conventional alternative methods especially for machines with diverse range of performance. The main features of the new controllers and the contributions of each research objective are summarized as below.

In **Chapter 2**, the Objective I is achieved by presenting a hybrid MTPA/MTPV control technique for the BLDC motors operating in the 180-degree mode. The proposed hybrid control scheme incorporates the conventional MTPA and MTPV methods which adjusts the advance in firing angle based on their simple explicit equations. Particularly, using a control logic, the hybrid method adopts the MTPA in steady state to achieve high efficiency, while in transients it smoothly converts to the MTPV to exploit the full torque capability of the machine, thus achieving faster

transient response. Comparing against the conventional MTPA and MTPV operations as well as the common mode of operation, the proposed method is shown to combine the advantages of both the MTPA and MTPV methods: in steady states, the scheme achieves a high efficiency similar to the MTPA operation; during transients, the performance is similar to the MTPV with a fast speed response. A practical solution of Objective I with smooth transitions between two methods has been provided and demonstrated. It is envisioned that the proposed hybrid MTPA/MTPV method may be an effective and straightforward control technique for many low-cost BLDC applications that require both high efficiency in the long term while operating in steady state as well as have access to higher torque during fast but intermittent transients.

The Objective II is addressed in **Chapter 3**, where easy-to-implement and straightforward numerical strategies of MTPA and MTPV operations have been developed for the BLDCs with 120-degree commutation logic. Specifically, the MTPA operation is conventionally achieved by fixing the firing angle at 30 degrees. However, it has been shown that for motors with large inductances, the commutation angle may be significant (e.g., up to 13.3 degrees for motor Model 86EMB3S98F), leading to misalignment of the phase current and the respective back EMF, and reduction in torque (e.g., 6.37% reduction). To compensate for this angle (which is dependent on motor parameters and operating conditions), a simple controller has been proposed to dynamically regulate the average d-axis current to zero, thus restoring the desired MTPA operation and improving the steady-state torque-speed characteristic over a wide range of operating conditions. Additionally, the MTPV methods based on lookup tables have been extended to the BLDC motors operating in the 120-degree mode. An algorithm to collect the firing angle has been established using the detailed simulation. Then, the firing angle can be easily obtained from the table under different dc voltages and machine speeds and thus, achieving the MTPV operation and improving

the voltage utilization. The proposed MTPA and MTPV methods has been verified using the detailed simulations with a typical industrial BLDC motor (with large inductance), and demonstrated to be very effective. The easy-to-implement and straightforward properties of the proposed methods makes them advantageous for many low-cost applications.

The **Chapter 4** has presented a novel extended control method of BLDC motors to achieve Objective III. Therein, a generalized switching logic for the Hall-sensor-controlled BLDC motors has been developed which allows to continuously change the conduction angle between 120 and 180 degrees. Aiming to maintain the optimal property of the MTPA, the strategy proposed in Section 3.2.2 has been extended to incorporate with the generalized/expended switching logic. Regardless of the motor parameters and the conduction angle (when it goes beyond 120 degrees), the alignment between the phase current (fundamental component) and the back EMF is automatically achieved with the proposed controller. Compared with the conventional method for increasing voltage range by simply increasing the dc source voltage, the proposed method has shown advantages of lower torque ripple and lower THD of phase voltage while achieving the same ac phase voltage with a lower dc voltage requirement. Additionally, the DSP implementation of this extended control method has been developed and is shown to be easy-to-implement and computational efficiency. Using the detailed simulations as well as hardware experiments based on a typical industrial BLDC motor, the proposed method has been demonstrated to be very effective and achieving up to 10% voltage (and speed-torque characteristic) extension for the same dc source voltage.

It is envisioned that the proposed extended method may be very attractive for many low-cost BLDC applications that require high efficiency while maximizing the utilization of the available

dc source. These applications would include all battery-operated applications with BLDC motors, including vehicles, scooters, hand-held tools, flying drones, etc.

5.2   Future Works

The research presented in this thesis may be continued in several directions. Due to the limited space, I mention here only three possible directions that will soon be undertaken by other students in our group:

Firstly, the hybrid MTPA/MTPV strategy has been developed for BLDC motors with 180-degree operation in this thesis. It is also desirable for BLDCs with 120-degree conduction logic (which is very common) to achieve both high steady-stare efficiency and fast dynamic response with a similar hybrid strategy. However, the proposed strategy in Section 2.3 is based on the simple explicit equations for 180-degree operation with the well-known voltage waveforms. In 120-degree operation, the commutation process and the stator inductance make it difficult to derive the closed-form analytical equations. Instead, the lookup-table-based extension of the proposed hybrid MTPA/MTPV strategy is expected to be developed for the BLDCs with 120-degree conduction logic.

Secondly, it may also be possible to derive another operating mode that will optimize the efficiency directly, as opposed to the MTPA which is known in the literature not to result in minimal losses. To derive this new mode of maximum efficiency (ME), one would need to obtain the analytical expression for the losses and then minimize these losses with respect to the given value of torque. I envision that this control mode may be established analytically for the BLDC motors operating using 180-degree switching logic, but it will have to be established numerically using lookup tables for the 120-degree switching logic due to the operating-point-dependent

commutation angle. Because of this challenge, for the proposed extended switching logic, the envisioned ME operation may only be established numerically and implemented using lookup tables.

Thirdly, the average-value models for the conventional commutation method (i.e., 180-degree and 120-degree modes of operation) have been well developed and play important roles in the industrial simulations and tuning of controllers. This is because the average-value models reduce the computational complexity by ignoring the fast-switching, which also makes the numerical linearization and subsequent frequency-domain analysis possible. For the generalized commutation logic developed in Chapter 4, it is also possible to develop a generalized average-value model to take full advantage of its low-computational cost and the capability to conduct frequency-domain analysis.

Bibliography

[1] D. Mohanraj *et al.*, "A review of BLDC motor: state of art, advanced control techniques, and applications," *IEEE Access*, vol. 10, pp. 54833-54869, May 2022.

[2] S. S. Patel *et al.*, "Modeling and implementation of intelligent commutation system for BLDC motor in underwater robotic applications," in *Proc. 1st Int. Conf. Power Electron., Intell. Control Energy Syst.*, Delhi, India, 2016, pp. 1-4.

[3] R. G. Bayardo, A. G. Loukianov, and E. N. Sánchez, "Adaptive control methodology for a class of nonlinear systems with speed tracking implementation for a BLDC motor," *IEEE Trans. Robot. Autom.*, vol. 7, no. 3, pp. 8363-8369, Jul. 2022.

[4] N. Samoylenko, Q. Han, and J. Jatskevich, "Dynamic performance of brushless dc motors with unbalanced hall sensors," *IEEE Trans. Energy Convers.*, vol. 23, no. 3, pp. 752–763, Sep. 2008.

[5] P. C. Krause, O. Wasynczuk, S. D. Pekarek, and T. O'Connell, Electromechanical Motion Devices: Rotating Magnetic Field-based Analysis with Online Animations. Hoboken: John Wiley & Sons, 2020.

[6] B. Hu, S. Sathiakumar, and Y. Shrivastava, "Sensorless drive of brushless DC motor with 180-degree commutation," in *Proc. ISECS Int. Colloquium Comput. Commun. Control. Manag.*, Sanya, China, 2009, pp. 579–582.

[7] T. F. Chan, Lie-Tong Yan, and Shao-Yuan Fang, "In-wheel permanent-magnet brushless dc motor drive for an electric bicycle," *IEEE Trans. Energy Convers.*, vol. 17, no. 2, pp. 229–233, Jun. 2002.

[8] W. Lee, J. H. Kim, W. Choi, and B. Sarlioglu, "Torque ripple minimization control technique of high-speed single-phase brushless dc motor for electric turbocharger," *IEEE Trans. Veh. Technol.*, vol. 67, no. 11, pp. 10357–10365, Nov. 2018.

[9] S. D. Sudhoff, and P. C. Krause, "Operating modes of the brushless dc motor with a 120 degrees inverter," *IEEE Trans. Energy Convers.*, vol. 5, no. 3, pp. 558–564, Sep. 1990.

[10] Q. Han, N. Samoylenko, and J. Jatskevich, "Average-value modeling of brushless dc motors with 120⁰ voltage source inverter," *IEEE Trans. Energy Convers.*, vol. 23, no. 2, pp. 423–432, Jun. 2008.

[11] R. Kumar, and B. Singh, "BLDC motor-driven solar PV array-fed water pumping system employing zeta converter," *IEEE Trans. Ind. Appl.*, vol. 52, no. 3, pp. 2315–2322, May/Jun. 2016.

[12] D. Das, N. Kumaresan, V. Nayanar, K. Navin Sam, and N. Ammasai Gounden, "Development of BLDC motor-based elevator system suitable for dc microgrid," *IEEE/ASME Trans. Mechatronics*, vol. 21, no. 3, pp. 1552–1560, Jun. 2016.

[13] K. Lee, D. Kim, B. Kim, and B. Kwon, "A novel starting method of the surface permanent-magnet BLDC motors without position sensor for reciprocating compressor," *IEEE Trans. Ind. Appl.*, vol. 44, no. 1, pp. 85–92, Jan./Feb. 2008.

[14] Y. Park, H. Kim, H. Jang, S. H. Ham, J. Lee, and D. H. Jung, "Efficiency improvement of permanent magnet BLDC with Halbach magnet array for drone," *IEEE Trans. Appl. Supercond.*, vol. 30, no. 4, pp. 1-5, Jun. 2020.

[15] A. De, A. Stewart-Height, and D. E. Koditschek, "Task-based control and design of a BLDC actuator for robotics," *IEEE Trans. Robot. Autom.*, vol. 4, no. 3, pp. 2393-2400, Jul. 2019.

[16]   T. Chun, Q. Tran, H. Lee, and H. Kim, "Sensorless control of BLDC motor drive for an automotive fuel pump using a hysteresis comparator," *IEEE Trans. Power Electron.*, vol. 29, no. 3, pp. 1382-1391, Mar. 2014.

[17]   Q. Zhang, J. Deng, and N. Fu, "Minimum copper loss direct torque control of brushless DC motor drive in electric and hybrid electric vehicles," *IEEE Access,* vol. 7, pp. 113264–113271, Jul. 2019.

[18]   H. C. Jung, D. J. Kim, S. Y. Jung, and D. Lee, "Optimization method to maximize efficiency map of a drive motor with electrical winding changeover technique for hybrid EV," *IEEE Trans. Appl. Supercond.,* vol. 30, no. 4, pp. 1–5, Apr. 2020.

[19]   J. N. Bae, S. J. Kim, J. H. Park, J. W. Ahn, and D. H. Lee, "An advanced speed control scheme for the high speed blender machine using BLDC motor," in *Proc. IEEE Student Conference on Electric Machines and Systems*, Huzhou, China, 2018, pp. 1–6.

[20]   C. Dinca, M. Bushe, A. Giedymin, and U. Schafer, "Mass producible optimized BLDC motor for automotive dynamic pump applications," in *Proc. Int. Conf. Elec. Machines (ICEM),* Berlin, Germany, 2014, pp. 1286–1292.

[21]   K. H. Nam, AC Motor Control and Electrical Vehicle Applications. Boca Raton: CRC Press, 2018.

[22]   G. Pellegrino, E. Armando, and P. Guglielmi, "Direct-flux vector control of IPM motor drives in the maximum torque per voltage speed range," *IEEE Trans. Ind. Electron.,* vol. 59, no. 10, pp. 3780–3788, Oct. 2012.

[23]   S. Ekanayake, R. Dutta, M. F. Rahman, and D. Xiao, "Deep flux weakening control of a segmented interior permanent magnet synchronous motor with maximum torque per voltage

control," in *Proc. 41st Annual Conf. IEEE Indust. Electron. Society (IECON),* Yokohama, Japan, 2015, pp. 4802–4807.

[24]   L. Sepulchre, M. Fadel, M. Pietrzak-David, and G. Porte, "MTPV flux-weakening strategy for PMSM high speed drive," *IEEE Trans. Ind. Appl.,* vol. 54, no. 6, pp. 6081–6089, Nov./Dec. 2018.

[25]   J. Li *et al.*, "Deep flux weakening control with six-step overmodulation for a segmented interior permanent magnet synchronous motor," in *Proc. 20th Int. Conf. Elect. Machines and Systems (ICEMS)*, Sydney, Australia, 2017, pp. 1–6.

[26]   M. N. Uddin, T. S. Radwan, and M. A. Rahman, "Performance of interior permanent magnet motor drive over wide speed range," *IEEE Trans. Energy Convers.,* vol. 17, no. 1, pp. 79–84, Mar. 2002.

[27]   H. Liu, Z. Zhu, E. Mohamed, Y. Fu, and X. Qi, "Flux-weakening control of nonsalient pole PMSM having large winding inductance, accounting for resistive voltage drop and inverter nonlinearities," *IEEE Trans. Power Electron.*, vol. 27, no. 2, pp. 942–952, Feb. 2012.

[28]   L. Sepulchre, M. Fadel, M. Pietrzak-David, and G. Porte, "MTPV flux-weakening strategy for PMSM high speed drive," *IEEE Trans. Ind. Appl.*, vol. 54, no. 6, pp. 6081–6089, Nov./Dec. 2018.

[29]   C. Miguel-Espinar, D. Heredero-Peris, G. Gross, M. Llonch-Masachs, and D. Montesinos-Miracle, "Maximum torque per Voltage flux-weakening strategy with speed limiter for PMSM drives," *IEEE Trans. Ind. Electron.*, vol. 68, no. 10, pp. 9254–9264, Oct. 2021.

[30]   S. Ekanayake, R. Dutta, M. F. Rahman, and D. Xiao, "Deep flux weakening control of a segmented interior permanent magnet synchronous motor with maximum torque per voltage

control," in *Proc. IEEE 41st Annu. Conf. Ind. Electron. Soc. (IECON)*, Yokohama, Japan, 2015, pp. 4802–4807.

[31]   D. Hu, L. Zhu, and L. Xu, "Maximum torque per Volt operation and stability improvement of PMSM in deep flux-weakening region," in *Proc. IEEE Energy Convers. Congr. Expo. (ECCE)*, Raleigh, USA, 2012, pp. 1233–1237.

[32]   S. John, and V. P. Mini, "Brushless dc motor (BLDCM) drive with maximum torque per Ampere (MTPA) control for electric vehicle application," in *Proc. Innov. Power Adv. Comput. Technol. (i-PACT)*, Kuala Lumpur, Malaysia, 2021, pp. 1–6.

[33]   S. Sue, Y. Huang, J. Syu and C. Sun, "A bi-directional power flow IPM-BLDC motor drive for electrical scooters," in *Proc. 5th IEEE Conf. Ind. Electron. Appl. (ICIEA)*, Taichung, Taiwan, 2010, pp. 1330–1334.

[34]   A. Khazaee, H. A. Zarchi, and G. R. A. Markadeh, "Real-time maximum torque per Ampere control of brushless dc motor drive with minimum torque ripple," *IEEE Trans. Power Electron.*, vol. 35, no. 2, pp. 1194–1199, Feb. 2020.

[35]   I. N. Syamsiana, M. F. Hakim, H. M. K, and M. Y. Irdandy, "Maximum torque per Ampere control strategy for load variation on sensorless brushless dc motor," in *Proc. Int. Conf. Electr. Inf. Technol. (IEIT)*, Malang, ID, 2021, pp. 151–154.

[36]   A. Khazaee, H. A. Zarchi, G. A. Markadeh, and H. Mosaddegh Hesar, "MTPA strategy for direct torque control of brushless dc motor drive," *IEEE Trans. Ind. Electron.*, vol. 68, no. 8, pp. 6692–6700, Aug. 2021.

[37]   L. Wang, Z. Zhu, H. Bin, and L. Gong, "A commutation error compensation strategy for high-speed brushless dc drive based on Adaline filter," *IEEE Trans. Ind. Electron.*, vol. 68, no. 5, pp. 3728–3738, May 2021.

[38]   X. Shi, X. Wang, C. Gu, and Z. Deng, "A novel commutation correction method for high-speed PM brushless dc motor," in *Proc. IEEE Appl. Power Electron. Conf. and Expo. (APEC)*, Tampa, USA, 2017, pp. 1899–1905.

[39]   B. Tan, X. Wang, D. Zhao, K. Shen, J. Zhao, and X. Ding, "A lag angle compensation strategy of phase current for high-speed BLDC motors," *IEEE Access*, vol. 7, pp. 9566–9574, Jan. 2019.

[40]   M. Lee, and K. Kong, "Fourier-series-based phase delay compensation of brushless dc motor systems," *IEEE Trans. Power Electron.*, vol. 33, no. 1, pp. 525–534, Jan. 2018.

[41]   F. Wang, C. Chang, and B. Liu, "Analysis of PMSM control performance based on the mathematical model and saturated parameters," in *Proc. IEEE Transp. Electrific. Conf. (ITEC)*, Beijing, China, 2014, pp. 1–5.

[42]   P. Vaclavek, and P. Blaha, "Interior permanent magnet synchronous machine field weakening control strategy - the analytical solution," in *Proc. Annu. Conf. Soc. Instrum. Control Eng. (SICE)*, Chofu, Japan, 2008, pp. 753–757.

[43]   L. Zhu, S. Xue, X. Wen, Y. Li and L. Kong, "A new deep field-weakening strategy of IPM machines based on single current regulator and voltage angle control," in *Proc. IEEE Energy Convers. Congr. Expo. (ECCE)*, Atlanta, USA, 2010, pp. 1144–1149.

[44]   L. Xu, Y. Zhang, and M. K. Guven, "A new method to optimize q-axis voltage for deep flux weakening control of IPM machines based on single current regulator," in *Proc. IEEE Int. Conf. Elect. Mach. Syst. (ICEMS)*, Wuhan, China, 2008, pp. 2750–2754.

[45]   J. Lee, "Interpolation error compensation for look-up table based PMSM control for electric vehicle," in *Proc. Int. Conf. Inf. Commun. Technol. Converg. (ICTC)*, Jeju, South Korea, 2018, pp. 1521–1524.

[46]   L. Huang, G. Zhao, and P. Huang, "An approach to improve the torque performance of IPMSM by considering cross saturation applied for hybrid electric vehicle," in *Proc. Int. Conf. Elect. Machines and Systems* (ICEMS), Incheon, South Korea, 2010, pp. 1378–1381.

[47]   Y. Chen, Y. Fang, X. Huang, and J. Zhang, "Torque and flux weakening control with MTPV for interior permanent magnet synchronous motor," in *Proc. IEEE Veh. Power Propulsion Conf. (VPPC)*, Hangzhou, China, 2016, pp. 1–5.

[48]   S. Saha, T. Tazawa, K. Narazaki, H. Murakami, and Y. Honda, "A novel sensorless control drive for an interior permanent magnet motor," in *Proc. IECON'01: 27th Annu. Conf. IEEE Ind. Electron. Soc.*, Denver, CO, USA, 2001, pp. 1655–1660.

[49]   S. Promthong, and M. Konghirun, "Sensorless control of BLDC motor drive with 150⁰ conducting mode to minimize torque ripple," in *Proc. Int. Conf. Elect. Mach. Syst.*, Busan, South Korea, 2013, pp. 1004–1009.

[50]   S. Wang, and A. Lee, "A 12-Step sensorless drive for brushless dc motors based on back-EMF differences," *IEEE Trans. Energy Convers.*, vol. 30, no. 2, pp. 646–654, Jun. 2015.

[51]   A. S. Al-Adsani, M. E. AlSharidah, and O. Beik, "BLDC motor drives: a single Hall sensor method and a 160⁰ commutation strategy," *IEEE Trans. Energy Convers.*, vol. 36, no. 3, pp. 2025–2035, Sep. 2021.

[52]   C. Wang, S. Wang, S. Lin, and H. Lin, "A novel twelve-step sensorless drive scheme for a brushless dc motor," *IEEE Trans. Magn.*, vol. 43, no. 6, pp. 2555–2557, Jun. 2007.

[53]   C. Cui, G. Liu, and K. Wang, "A novel drive method for high-speed brushless dc motor operating in a wide range," *IEEE Trans. Power Electron.*, vol. 30, no. 9, pp. 4998–5008, Sep. 2015.

[54]   The Math Works, Inc., (2022). *MATLAB & SIMULINK: Simulink Reference.* [Online]. Available: www.mathworks.com.

[55]   The Math Works, Inc., (2022). *MATLAB & SIMULINK: Simscape Reference.* [Online]. Available: www.mathworks.com.

[56]   The Math Works, Inc., (2006). *SimPowerSystems: Model and Simulate Electrical Power Systems User's Guide.* [Online]. Available: www.mathworks.com.

[57]   R. Shanmugasundram, K. Zakariah, and N. Yadaiah, "Implementation and performance analysis of digital controllers for brushless dc motor drives," *IEEE/ASME Trans. Mechatronics*, vol. 19, no. 1, pp. 213–224, Feb. 2014.

[58]   M. Ebadpour, N. Amiri, and J. Jatskevich, "Fast fault-tolerant control for improved dynamic performance of Hall-sensor-controlled brushless dc motor drives," *IEEE Trans. Power Electron.*, vol. 36, no. 12, pp. 14051–14061, Dec. 2021.

[59]   J. Shao, D. Nolan, and T. Hopkins, "Improved direct back EMF detection for sensorless brushless dc (BLDC) motor drives," in *Proc. IEEE Appl. Power Electron. Conf. and Expo. (APEC)*, Miami Beach, USA, 2003, pp. 300–305.

[60]   H. S. Chuang, Y. Ke, and Y. C. Chuang, "Analysis of commutation torque ripple using different PWM modes in BLDC motors," in *Proc. IEEE Ind. Commercial Power Syst. Tech. Conf. (I&CPS)*, Calgary, Canada, 2009, pp. 1–6.

[61]   D. Dwivedi, S. Singh, and J. Kalaiselvi, "Impact of PWM and duty ratio control on voltage for sic fed three phase BLDC motor drive," in *Proc. IEEE Int. Conf. Power Electron. Smart Grid Renew. Energy (PESGRE)*, Trivandrum, India, 2022, pp. 1–5.

[62]   L. Yang, Z. Zhu, H. Bin, Z. Zhang, and L. Gong, "Safety operation area of zero-crossing detection-based sensorless high-speed BLDC motor drives," *IEEE Trans. Ind. Appl.*, vol. 56, no. 6, pp. 6456–6466, Nov./Dec. 2020.

[63]   K. Liu, Z. Zhou, and W. Hua, "A novel region-refinement pulse width modulation method for torque ripple reduction of brushless dc motors," *IEEE Access*, vol. 7, pp. 5333–5342, Dec. 2019.

[64]   Q. Zhou, J. Shu, Z. Cai, Q. Liu, and G. Du, "Improved PWM-OFF-PWM to reduce commutation torque ripple of brushless dc motor under braking conditions," *IEEE Access*, vol. 8, pp. 204020–204030, Nov. 2020.

[65]   Plexim GmbH., (2006). *Piecewise Linear Electrical Circuit Simulation (PLECS) User Manual*, Version. 1.4 [Online]. Available: www.plexim.com.

[66]   H. Li, S. Zheng, and H. Ren, "Self-correction of commutation point for high-speed sensorless BLDC motor with low inductance and nonideal back EMF," *IEEE Trans. Power Electron.*, vol. 32, no. 1, pp. 642–651, Jan. 2017.

[67]   X. Zhou, X. Chen, F. Zeng, and J. Tang, "Fast commutation instant shift correction method for sensorless coreless BLDC motor based on terminal voltage information," *IEEE Trans. Power Electron.*, vol. 32, no. 12, pp. 9460–9472, Dec. 2017.

[68]   P. Damodharan, and K. Vasudevan, "Sensorless brushless dc motor drive based on the zero-crossing detection of back electromotive force (EMF) from the line voltage difference," *IEEE Trans. Energy Convers.*, vol. 25, no. 3, pp. 661–668, Sep. 2010.

[69]   Texas Instruments, Inc., (2017). *Low-Side Current Sense Circuit Integration,* [Online]. Available: www.ti.com.

Appendix A Parameters of BLDC Motor

Drive Systems

A.1   BLDC Motor A

Arrow Precision Motor Company, Ltd., Model 86EMB3S98F, 36 V, 2000 r/min, 8 poles, $r_s = 0.15\ \Omega$, $L_{ss} = 0.45\ \text{mH}$, $\lambda_m^{'} = 21.5\ \text{mVs}$, $J = 12e - 4\ \text{kgm}^2$.

A.2   BLDC Motor B

Maxon Precision Motor Company, Inc., Model EC 167131, 48 V, 2680 r/min, 2 poles, $r_s = 0.674\ \Omega$, $L_{ss} = 0.41\ \text{mH}$, $\lambda_m^{'} = 86.2\ \text{mVs}$, $J = 12e - 4\ \text{kgm}^2$.

A.3   BLDC Motor C

JKONG Motor Company, Ltd., Model JK80BLS02, 48 V, 3000 r/min, 4 poles, $r_s = 0.28\ \Omega$, $L_{ss} = 1.2\ \text{mH}$, $\lambda_m^{'} = 37.0\ \text{mVs}$, $J = 7.5e - 4\ \text{kgm}^2$.

A.4   VSI

Snubber resistance $R_{snubber} = 1e5\ \Omega$.

Appendix B Controller Parameters

B.1   Parameters of the Proposed Hybrid MTPA/MTPV Controller for the BLDC with 180-degree Operation (in Section 2.4)

Speed regulator parameters:

$$K_p = 0.0269, \ K_i = 0.2049.$$

Threshold:

$$\text{threshold-1} = 5\%, \ \text{threshold-2} = 0.05\%.$$

Low-pass filter parameters:

$$\tau_{L-1} = 0.500, \ \tau_{L-2} = 0.005.$$

B.2   Parameters of the Proposed MTPA Controller for the BLDC with 120-degree Operation (in Section 3.4)

PI controller parameters:

$$K_p = 0.0136, \ K_i = 1.4880.$$

B.3   Parameters of the Proposed MTPA Controller for the BLDC beyond 120-degree Operation (in Section 4.3 and 4.4)

PI controller parameters:

$$K_p = 0.0136, \ K_i = 4.4640.$$

Appendix C Mechanical Load Conditions

C.1 Assumptions of the Mechanical Load in Section 2.4

$T_m = K_{m1}\omega_r^2$, where $K_{m1} = 1.0e - 6 \text{Nm s}^2/\text{rad}^2$.

C.2 Assumptions of the Mechanical Load in Section 4.3

$T_m = K_{m2}\omega_r^2$, where $K_{m2} = 1.5e - 6 \text{Nm s}^2/\text{rad}^2$.

C.3 Approximation of the Mechanical Load in Section 4.4

In the hardware experiments, the BLDC motor is coupled with a dynamometer with an equivalent circuit shown in Figure 0.1. In steady-state, the induced voltage is expressed as

$$E_a = I_a\left(R_a + R_{ext}\right), \tag{A.1}$$

where the armature resistance is R_a = 0.77 Ω and the external resistance is fixed at R_{ext} = 14.88 Ω. Also, for the DC machine, the equations for back EMF and electromagnetic torque can be written as

$$E_a = k_v\omega_r, \tag{A.2}$$

$$T_e = k_t i_a, \tag{A.3}$$

where the voltage and torque constants are k_v = k_t = 0.23 Vs/rad. Based on (A.1)–(A.3), the electromagnetic torque T_e can be expressed in terms of the rotor speed ω_r as

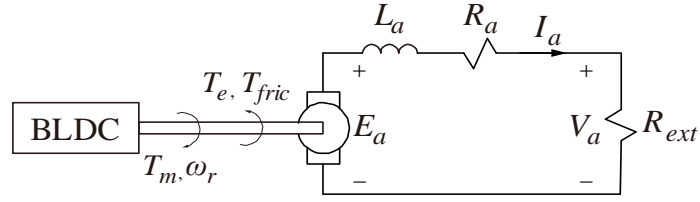$$T_e = k_v^2\omega_r / (R_a + R_{ext}). \tag{A.4}$$

Figure C.1 A permanent magnet DC dynamometer.

Considering the friction torque, the load torque is expressed as

$$T_m = T_e + T_{fric} = k_v^2 \omega_r / (R_a + R_{ext}) + T_{fric} , \tag{A.5}$$

where the friction torque T_{fric} is approximately constant and its value is 0.18 Nm. Overall, the load

torque is described as

$$T_m = K_{m3}\omega_r + K_{m4} , \tag{A.6}$$

where $K_{m3} = 0.0034 \text{ Nm} \cdot \text{s/rad}$ and $K_{m4} = 0.18 \text{ Nm}$.

Appendix D Diagrams of DSP

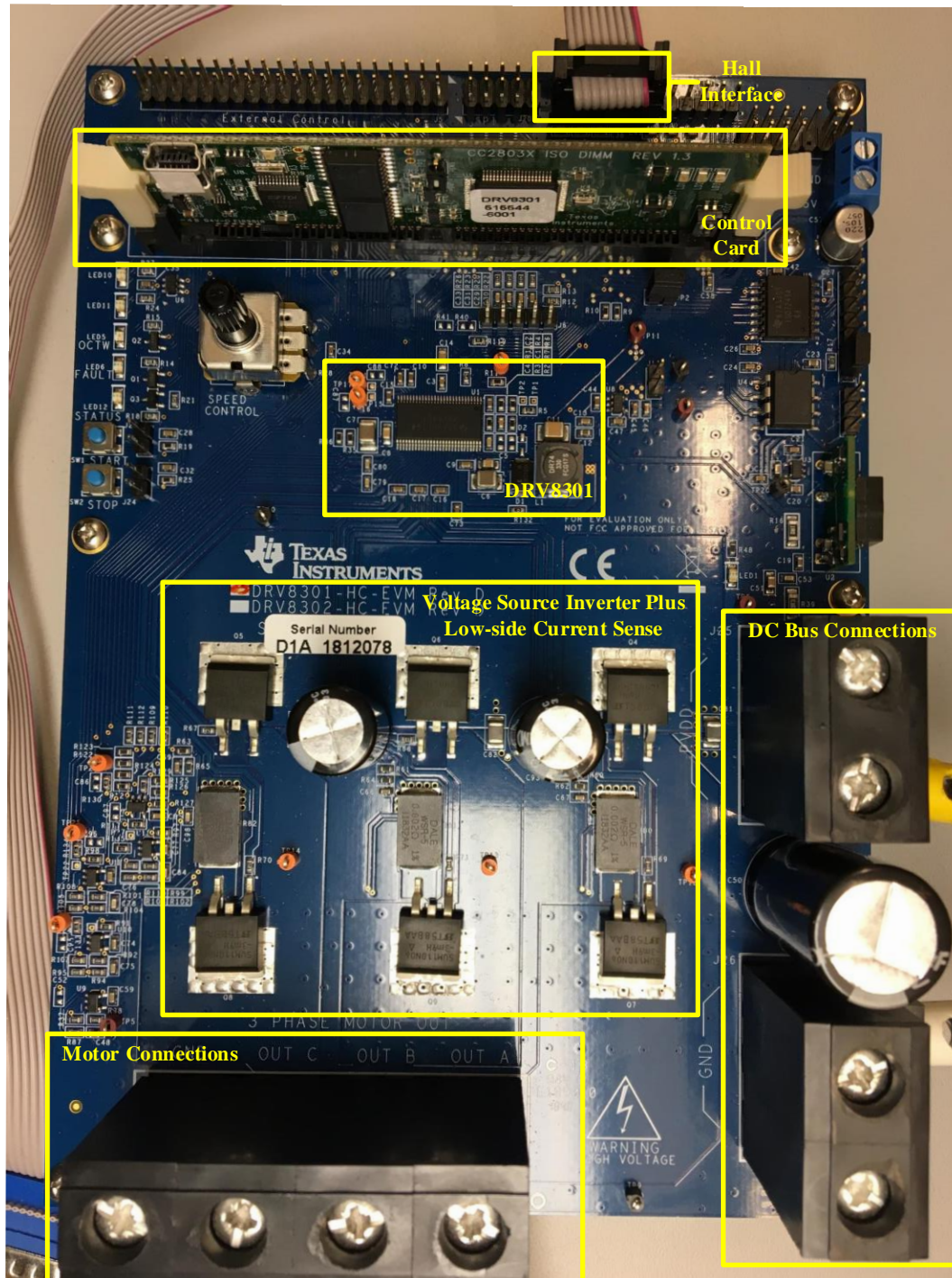## D.1   Layout of DSP DRV8301-HC-EVM

Figure D.1 Layout of DSP DRV8301-HC-EVM.

D.2 Functional block diagram of DSP DRV8301-HC-EVM
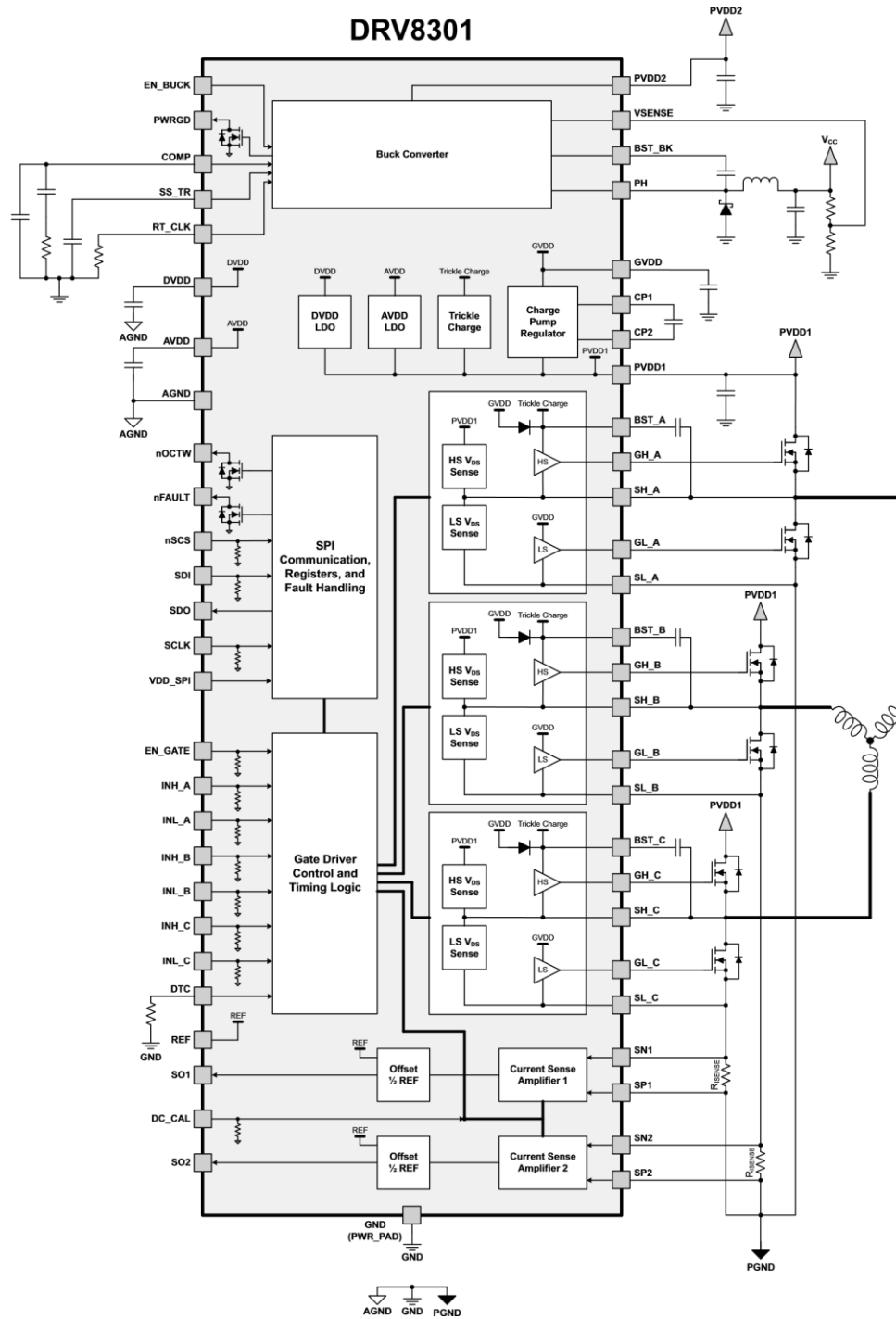

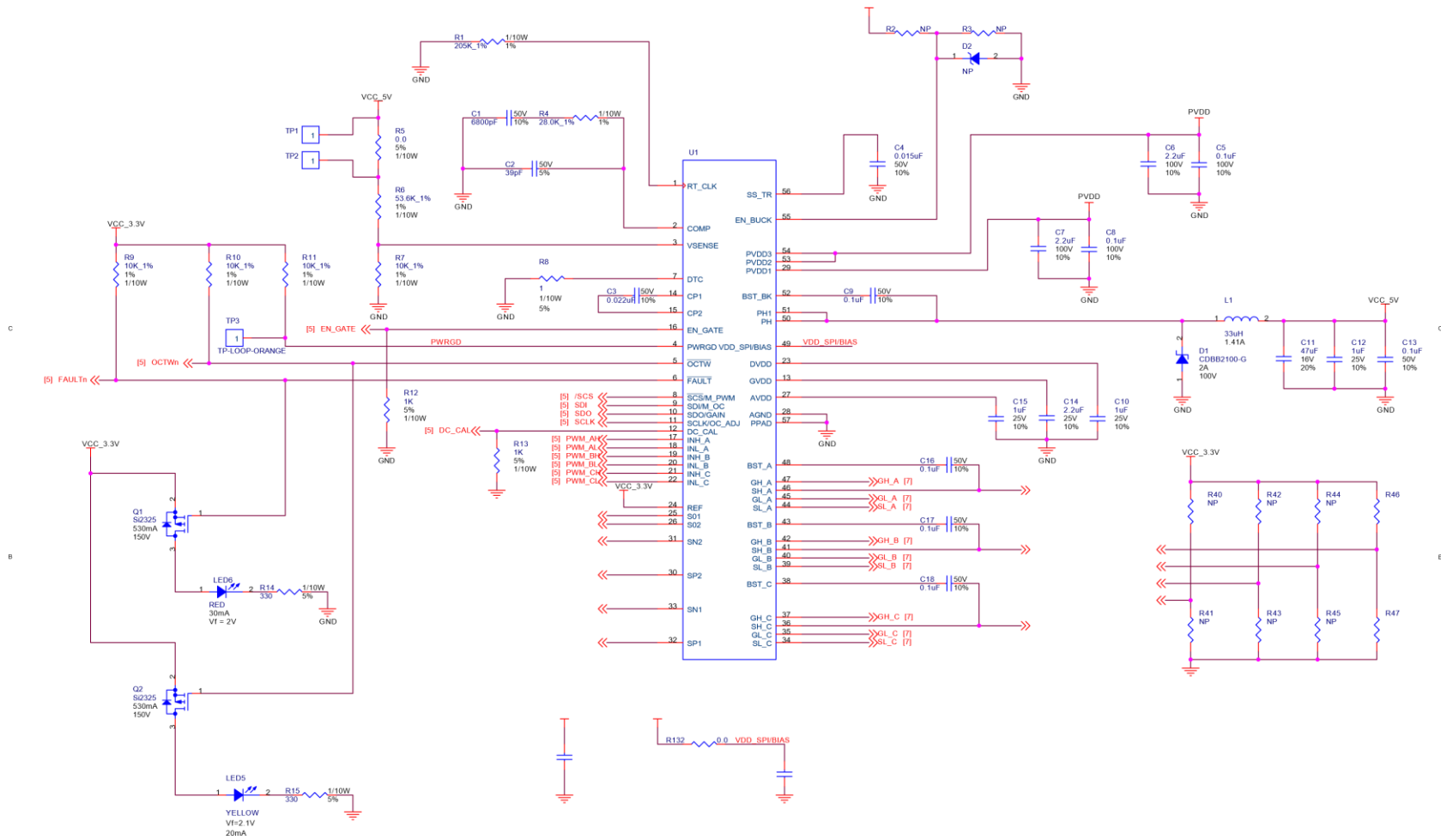**Figure D.2 Functional block diagram of DRV8301.**

D.3   Schematic of DSP DRV8301-HC-EVM

Figure D.3 Schematic of DSP DRV8301-HC-EVM.